JEM Journal of Experimental Medicine

ARTICLE

IMPA1-derived inositol maintains stemness in castration-resistant prostate cancer via IMPDH2 activation

Che-Chia Hsu[1,2], Guihua Wang[2], Chien-Feng Li[4], Xian Zhang[2], Zhen Cai[2], Tingjin Chen[1,2], Bo-Syong Pan[1,2], Rajesh Kumar Manne[1,2], Gagan Deep[2], Haiwei Gu[5], Yuzhuo Wang[9], Danni Peng[2], Vasudevarao Penugurti[1,2], Xiaobo Zhou[7], Zhigang Xu[8], Zhongzhu Chen[8], Ming Chen[1], Andrew J. Armstrong[3], Jiaoti Huang[1], Hong-Yu Li[6], and Hui-Kuan Lin[1,2]

Acquisition of prostate cancer stem cells (PCSCs) manifested during androgen ablation therapy (ABT) contributes to castration-resistant prostate cancer (CRPC). However, little is known about the specific metabolites critically orchestrating this process. Here, we show that IMPA1-derived inositol enriched in PCSCs is a key metabolite crucially maintaining PCSCs for CRPC progression and ABT resistance. Notably, conditional *Impa1* knockout in the prostate abrogates the pool and properties of PCSCs to orchestrate CRPC progression and prolong the survival of *TRAMP* mice. IMPA1-derived inositol serves as a cofactor that directly binds to and activates IMPDH2, which synthesizes guanylate nucleotides for maintaining PCSCs with $AR^{low/-}$ features leading to CRPC progression and ABT resistance. IMPA1/inositol/IMPDH2 axis is upregulated in human prostate cancer, and its overexpression predicts poor survival outcomes. Genetically and pharmacologically targeting the IMPA1/inositol/IMPDH2 axis abrogates CRPC and overcomes ABT resistance in various CRPC xenografts, patient-derived xenograft (PDX) tumor models, and *TRAMP* mouse models. Our study identifies IMPDH2 as an inositol sensor whose activation by inositol represents a key mechanism for maintaining PCSCs for CRPC and ABT resistance.

Introduction

Prostate cancer is the second leading cause of cancer-related deaths in the United States. Prostate cancer initially responds well to androgen ablation therapy (ABT) but inevitably develops a resistant mechanism in an advanced stage where prostate cancer is no longer sensitive to ABT, known as castration-resistant prostate cancer (CRPC). The CRPC is an unmet medical problem due to the lack of an effective treatment strategy. Insufficient understanding of the mechanisms driving CRPC greatly limits our ability to develop an effective strategy to tackle this dismal disease.

Prostate tumor heterogeneity contains the mixture of cells whose stemness and/or proliferative ability varies (Beltran et al., 2011). One of the resistant mechanisms of anti-androgen treatment has been discussed through which prostate cancer cells escape from androgen receptor (AR) pathway inhibition via lineage switching. A small cell population with the properties of prostate cancer stem-like cells (PCSCs) is capable of driving tumor growth, metastatic spread, and therapy resistance due to the features of stem cells. The conversion and/or acquisition of cancer stem cell (CSC) phenotype with low or negative expression of $AR^{low/-}$ from AR-positive luminal prostate cancer cells, a process known as lineage plasticity, is now considered one of the prominent mechanisms for driving CRPC progression and ABT resistance (Aggarwal et al., 2018; Ku et al., 2017; Mu et al., 2017). While ABT eliminates AR^{+} luminal epithelial cells, it spares a small cell population of prostate cancer cells known as PCSCs (Davies et al., 2018; Reya et al., 2001), which are exemplified by high aldehyde dehydrogenase (ALDH) and low/negative AR expression (Qin et al., 2012; van den Hoogen et al., 2010). Notably, the next-generation anti-androgen agent, such as enzalutamide, has driven the occurrence of aggressive and adaptive cancer cells with AR-independent CSC features that maintain

[1]Department of Pathology, Duke University Medical Center, Duke University School of Medicine, Durham, NC, USA; [2]Department of Cancer Biology, Wake Forest Baptist Medical Center, Wake Forest University, Winston Salem, NC, USA; [3]Duke Cancer Institute Center, Duke University School of Medicine, Durham, NC, USA; [4]Department of Pathology, Chi-Mei Medical Center, Tainan, Taiwan; [5]Cellular Biology and Pharmacology Department, Center for Translational Science, The Herbert Wertheim College of Medicine, Florida International University, Port St. Lucie, FL, USA; [6]Division of Pharmaceutical Science, College of Pharmacy, University of Arkansas for Medical Sciences, Little Rock, AR, USA; [7]Center for Computational Systems Medicine, School of Biomedical Informatics, The University of Texas Health Science Center at Houston, Houston, TX, USA; [8]Chongqing Engineering Laboratory of Targeted and Innovative Therapeutics, Chongqing Key Laboratory of Kinase Modulators as Innovative Medicine, IATTI, Chongqing University of Arts and Sciences, Chongqing, China; [9]Department of Experimental Therapeutics, BC Cancer Research Institute, Vancouver, Canada.

Correspondence to Hui-Kuan Lin: hui-kuan.lin@duke.edu.

prostate tumor growth and survival (Davies et al., 2018; Germann et al., 2012; Lee et al., 2013; Qin et al., 2012; Seiler et al., 2013). Despite targeting PCSCs involved in CRPC progression is a promising strategy to target CRPC and overcome ABT resistance, how PCSCs can be pharmacologically targeted remains yet to be established.

Of note, advanced prostate cancer commonly associated with loss of p53 and Rb arises from the stem cell–enriched proximal region of prostate (Zhou et al., 2006, 2007), accompanied by the upregulation of reprogramming factor SOX2 and epigenetic factor EZH2 (Kregel et al., 2013; Ku et al., 2017; Mu et al., 2017; Nyquist et al., 2020). Notably, SOX2 or EZH2 upregulation triggers the expression of diverse target genes involved in lineage plasticity with PCSC features leading to CRPC (Dardenne et al., 2016; Ku et al., 2017; Mu et al., 2017). Although pharmacologically targeting SOX2 and EZH2 appear to be an ideal strategy for eradicating PCSCs and thus CRPC, there is no effective agent currently available for targeting SOX2 (Hüser et al., 2018) or the lack of a well-tolerable EZH2 inhibitor (Yamagishi and Uchimaru, 2017). As there is no effective and tolerable strategy for PCSCs thus far, it is crucial to identify a novel druggable and tolerable target critical for maintaining PCSCs, thus allowing for developing an effective strategy to combat CRPC and ABT resistance.

Energy metabolism has emerged to play a key role in cancer progression, metastasis, and drug resistance (Elia et al., 2019; Faubert et al., 2017, 2020). Cancer cells display distinct metabolic programs compared with normal counterparts, which endow cancer cells with high cell proliferation and survival advantages (Hui et al., 2017; Mashimo et al., 2014; Mayers et al., 2016). Accumulating evidence reveals that CSCs also display distinct metabolic signatures relative to differentiated bulk cancer cells, raising the possibility that unique metabolic reprogramming operated in CSCs may serve as a crucial mechanism to maintain CSC pools and functions. Energy metabolism not only provides energy sources and building blocks for cancer cells but also offers unique metabolites such as α-ketoglutarate (α-KG), which activates histone demethylases and involves in epigenetics and transcription for regulating distinct biological processes (Carey et al., 2015; Lu and Thompson, 2012), and glycolysis-derived lactate, which represses retinoic acid-inducible gene I (RIG-1) like receptor (RLR)/interferon signaling and viral infection by directly targeting mitocondrial antiviral signaling protein (MAVS) (Zhang et al., 2019). These studies offer new insights into the unique role of the metabolites in regulating signaling and epigenetics through direct protein sensing. It will be of significance to explore whether there are unique metabolic enzymes through the synthesis of key metabolites critically maintaining PCSC properties with $AR^{low/-}$ features for CRPC progression and ABT resistance.

Results

IMPA1/inositol is enriched in PCSCs and maintains the functions of PCSCs

To identify the novel metabolic and targetable mechanisms critically maintaining PCSCs, we aimed to dissect distinct metabolites and metabolic gene signatures between PCSCs and non-PCSCs. As ALDH has been well established as a key PCSC marker (Clark and Palle, 2016; van den Hoogen et al., 2010), we isolated $ALDH^{high}$ (PCSCs) and $ALDH^{low/-}$ (non-PCSCs) prostate cancer cells from PC3 and LNCaP for systematic metabolomics, transcriptomics analysis, and RNA-sequencing (RNA-seq) analysis. Several unique metabolites involved in glycolysis, alanine metabolism, TCA cycle, nucleotide sugars metabolism, nicotinate and nicotinamide metabolism, and inositol metabolism were specifically enriched in $ALDH^{high}$ PCSCs compared with $ALDH^{low/-}$ non-PCSCs, while 200 genes were upregulated in $ALDH^{high}$ PCSCs (Fig. 1, A and B; and Fig. S1, A–C; data available at figshare: https://figshare.com/s/01c3a4c13ecdff7be728; https://figshare.com/s/3ff185e2781d54b039cf; https://figshare.com/s/5081739c2f2cba50553d). By integrating metabolomics and transcriptomic datasets, we found that both myo-inositol and its synthesis enzyme, inositol monophosphatase 1 (*IMPA1*), which is a crucial enzyme triggering myo-inositol production from inositol monophosphate derived from glucose-6-phosphate (G6P), were highly enriched in $ALDH^{high}$ PCSCs from PC3 and LNCaP cells (Fig. 1, A and B; and Fig. S1, B–F). Immunoblotting assay further verified that $ALDH^{high}$ PCSCs displayed not only higher expression of CSC marker Oct4, reprogramming factor SOX2 but also high IMPA1 protein expression, accompanied by reduced luminal cell marker AR expression, compared with $ALDH^{low/-}$ non-PCSCs isolated from AR-positive 22RV1 and LNCaP cells (Fig. S1, G–I). Notably, metabolism ontology analysis revealed the higher enrichment of inositol metabolism in the $ALDH^{high}$ PCSCs compared with $ALDH^{low/-}$ PCSCs (Fig. S1 A).

Myo-inositol (hereafter as inositol) is a precursor used for the production of phosphatidylinositol (PI) and phosphoinositides (Fig. S1 D). The functions of inositol are primarily attributed to its conversation into PI or distinct phosphoinositides, which are involved in diverse biological processes including membrane trafficking, cell growth, apoptosis, and cell movement (Di Paolo and De Camilli, 2006). The key gap that remains to be determined is whether inositol can serve as a second messenger that directly targets its protein sensors and in turn regulates novel biological outcomes and oncogenic processes beyond its classic role in regulating PI and phosphoinositides cycle. Moreover, the role of the IMPA1/inositol axis in CSC regulation has never been reported thus far. Consistent with the result observed from $ALDH^{high}$ PCSCs, the mRNA and protein levels of IMPA1 were also increased in spheroid cells, which are constituted primarily by PCSCs, compared with adherent cells from three CRPC cell lines including PC3, DU145, and 22RV1, correlated with higher expression of CSC markers like Nanog and SOX2 (Fig. S1, J–L). Thus, IMPA1/inositol axis is highly enriched in PCSCs.

Because both inositol and its synthesis enzyme, IMPA1, are enriched in $ALDH^{high}$ PCSCs, we there focused on dissecting the role of the IMPA1/inositol axis in regulating the properties of PCSCs. To this end, we knocked down IMPA1 with its two distinct lentiviral shRNAs (shIMPA1 #1 and #2) in diverse prostate cancer cell lines including CRPC (AR-positive and AR-negative) cells for cancer sphere assay. Metabolomics assay revealed that loss of IMPA1 in prostate cancer cells led to an expected decline in inositol and its downstream metabolites including IP_2, IP, PI,

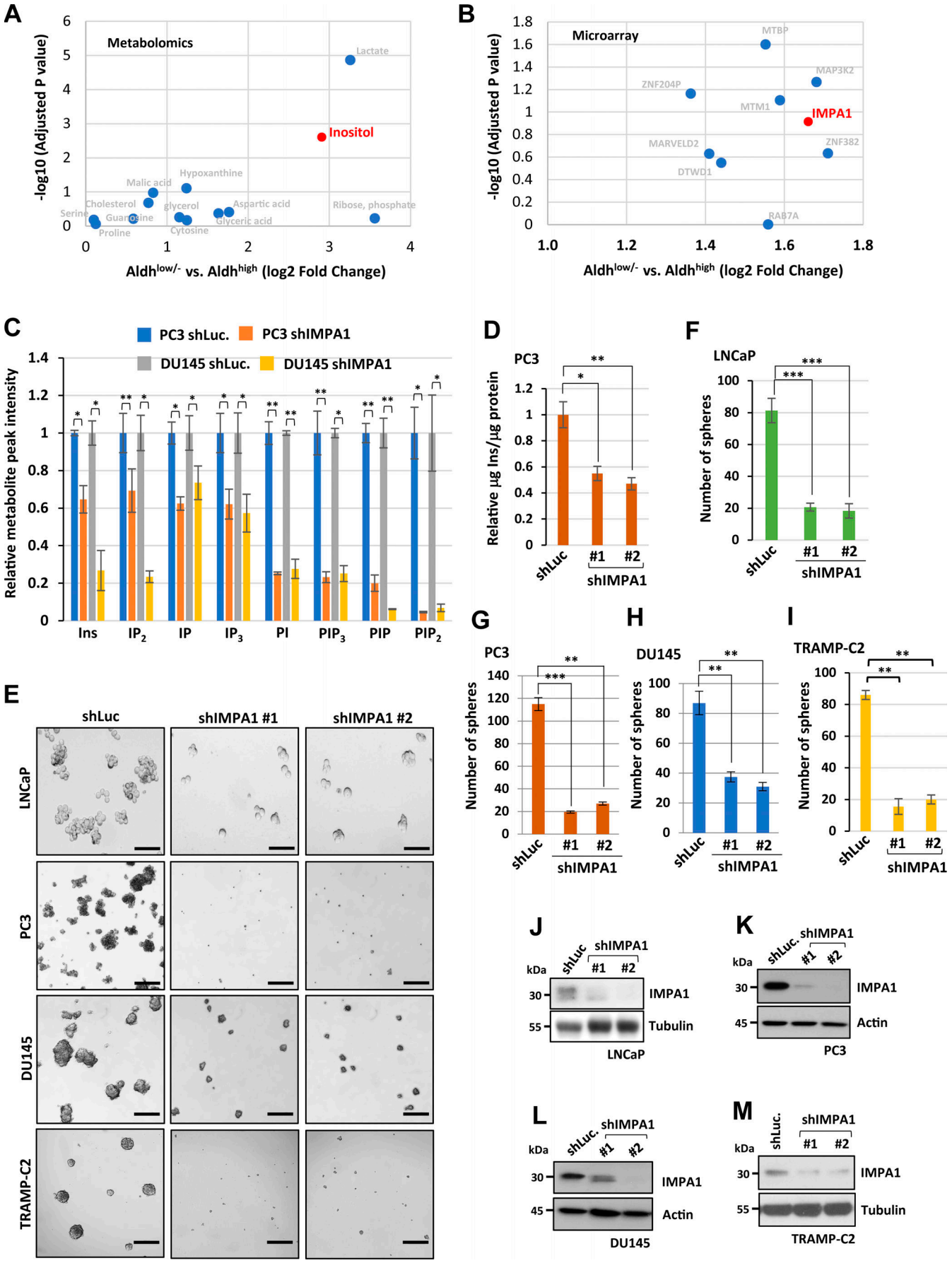
A
Metabolomics
-log10 (Adjusted P value)
Aldh^low/- vs. Aldh^high (log2 Fold Change)
Lactate
Inositol
Hypoxanthine
Malic acid
Cholesterol
glycerol
Aspartic acid
Ribose, phosphate
Serine
Guanosine
Glyceric acid
Cytosine
Proline
B
Microarray
-log10 (Adjusted P value)
Aldh^low/- vs. Aldh^high (log2 Fold Change)
MTBP
MAP3K2
ZNF204P
MTM1
IMPA1
MARVELD2
ZNF382
DTWD1
RAB7A
C
PC3 shLuc.
PC3 shIMPA1
DU145 shLuc.
DU145 shIMPA1
Relative metabolite peak intensity
Ins
IP2
IP
IP3
PI
PIP3
PIP
PIP2
D
PC3
Relative μg Ins/μg protein
shLuc
#1
#2
shIMPA1
F
LNCaP
Number of spheres
G
PC3
H
DU145
I
TRAMP-C2
E
shLuc
shIMPA1 #1
shIMPA1 #2
LNCaP
PC3
DU145
TRAMP-C2
J
kDa
IMPA1
Tubulin
LNCaP
K
Actin
PC3
L
DU145
M
TRAMP-C2

Figure 1. **IMPA1/inositol axis is enriched in ALDH-positive PCSCs and maintains prostate cancer stemness. (A and B)** Dot plots show the upregulation of genes and metabolites in ALDH^{high} compared with ALDH$^{low/-}$ of PC3 cells. PC3 cells were isolated using FACS based on ALDH expression. **(C)** Metabolic profiling of PC3 or DU145 cells expressing shLuc or shIMPA1 was revealed by targeted mass spectrometry analysis of phosphoinositides metabolism including inositol (Ins), PI, inositol 1,3,4-trisphosphate (IP_3), phosphatidylinositol 3-phosphate (PIP), and inositol 4-phosphate (IP). Each metabolite in the shIMPA1 group was normalized by shLuc showing relative peak intensity. The mean ± SEM showed three independent experiments for each group. *, P < 0.05; **, P < 0.01 by two-tailed unpaired *t* test. **(D)** The level of inositol of PC3 cells stably expressing shLuc or IMPA1-two specific shRNA lentivirus (#1 and #2) was determined using a K-INOSL assay kit according to the manufacturer's instructions. The inositol levels were normalized by protein concentration in each experimental group. The mean ± SEM showed three independent experiments for each group. *, P < 0.05; **, P < 0.01 by two-tailed unpaired *t* test. **(E)** Spheres from LNCaP, PC3, DU145, and TRAMP-C2 stably expressing shLuc or IMPA1-two specific shRNA lentivirus (#1 and #2) were shown. Scale bar, 200 µm. **(F–I)** Quantification of the number of spheres from E was shown for LNCaP (F), PC3 (G), DU145 (H), and TRAMP-C2 (I). The mean ± SEM showed three independent experiments for each group. **, P < 0.01; ***, P < 0.001 by two-tailed unpaired *t* test. **(J–M)** Immunoblotting of LNCaP (J), PC3 (K), DU145 (L), and TRAMP-C2 (M) cells stably expressing shLuc or shIMPA1 (#1 and #2) with indicated antibodies. Immunoblotting data were verified in at least two independent experiments. Source data are available for this figure: SourceData F1.

IP_3, PI, PIP_3, PIP, and PIP_2 (Fig. 1 C). Of note, IMPA1 loss by IMPA1 knockdown markedly reduced inositol levels (Fig. 1 D), impaired prostate cancer sphere formation from four prostate cancer cell lines including AR-positive LNCaP and TRAMP-C2 cells and AR-negative PC3 and DU145 cells (Fig. 1, E–M), and reduced ALDH^{high} PCSC populations (Fig. S1, M and N). Likewise, pharmacological inactivation of IMPA1 activity by IMPA inhibitor, lithium chloride (LiCl), also suppressed cancer sphere formation (Fig. S1, O–T). Although LiCl could also inactivate GSK3β kinase activity, the treatment of specific GSK3β inhibitors, BIO and SB216763, failed to affect cancer sphere formation (Fig. S1, Q–T), indicating that LiCl does not appear to act through GSK3β inactivation to suppress cancer sphere formation.

To strengthen the specific role of IMPA1/inositol in maintaining PCSCs, we isolated PCSCs by sorting ALDH^{high} cells from LNCaP and TRAMP-C2 cells. Approximately, 5.27% ALDH^{high} PCSCs and 3.8% ALDH^{high} PCSCs were identified (Fig. S2, A and B). IMPA1 knockdown decreased inositol levels in both ALDH^{high} and ALDH$^{low/-}$ cells sorted from LNCaP and TRAMP-C2 (Fig. S2, C and D). Colony formation assay and cancer sphere assay revealed that IMPA1 knockdown significantly inhibited cancer sphere formation and cell proliferation in ALDH^{high} PCSCs from LNCaP cells and TRAMP-C2 (Fig. S2, E, G, I, J, and M–O). However, loss of IMPA1 did not affect cell proliferation in ALDH$^{low/-}$ cells (>94%) from LNCaP and TRAMP-C2 (Fig. S2, F, H, K, and L). These results suggest that IMPA1/inositol critically maintains the proliferation of ALDH^{high} PCSCs, but not ALDH$^{low/-}$ non-PCSCs.

To further validate the functional role of IMPA1/inositol axis in maintaining PCSC properties in vivo, we sorted ALDH$^{low/-}$ non-PCSCs and ALDH^{high} PCSCs from androgen-dependent LNCaP (AR-positive) and PC3 (AR-negative) CRPC cells upon control knockdown and IMPA1 knockdown (shIMPA1 #1 and #2), followed by in vivo limiting dilution assay, which is a gold standard for assessing the properties of CSCs in vivo (Jahchan et al., 2016) (Fig. 2 A). Extremely transplanting limiting dilution analysis revealed that the frequency of tumor-initiating ALDH^{high} PCSCs was far greater than ALDH$^{low/-}$ PCSCs from these cell lines with 12.8-fold higher in LNCaP and 3.5-fold higher in PC3 (Fig. 2, B–E). Importantly, the loss of IMPA1 significantly abrogated tumor-initiating capabilities of the ALDH^{high} population with only 100 ALDH^{high} cells inoculated into nude mice (Fig. 2, B–E). Thus, IMPA1 appears to be commonly required for PCSC properties in vivo both from androgen-dependent and androgen-independent prostate cancer cells.

To further examine the role of IMPA1/inositol axis in PCSCs ex vivo, we established tumor organoids from male *TRAMP* mice, which display CRPC due to *pRB* and *p53* inactivation (Chiaverotti et al., 2008; Gelman, 2016; Quaglia et al., 2021) (Fig. 2, F and G). H&E staining and immunohistochemistry (IHC) analyses revealed that prostate tumor organoids isolated from *TRAMP* mouse model exhibited high expression IMPA1 (Fig. 2 H). Remarkably, the knockdown of IMPA1 impaired tumor organoid formation in *TRAMP* mouse model (Fig. 2, I–K). Of note, restoration of inositol rescued the defect in prostate cancer sphere formation and tumor organoid growth from *TRAMP* mouse model (Fig. S1, U and V; and Fig. 2, L and M) upon IMPA1 knockdown.

To examine the effect of IMPA1 loss on prostate cancer stem cells ex vivo, we further isolated ALDH^{high} PCSCs and ALDH$^{low/-}$ non-PCSCs from *TRAMP* mouse model, followed by IMPA1 knockdown using two independent shRNAs (Fig. 3 A). Approximately, 8.45% ALDH^{high} cells were isolated from the prostate tissue of *TRAMP* mouse model (Fig. 3 B). ALDH^{high} PCSCs, but not ALDH$^{low/-}$ non-PCSCs, isolated from *TRAMP* mice could form prostate tumor organoids (Fig. 3 C). Western blotting and IHC analysis revealed that the protein levels of IMPA1 also significantly decreased, accompanied by reduced inositol levels, in tumor organoids with IMPA1 knockdown compared with control knockdown (Fig. 3, D–F). Notably, ALDH^{high} tumor organoids isolated from *TRAMP* mice upon IMPA1 knockdown dramatically inhibited the formation of tumor organoids compared with control knockdown (Fig. 3, F and G). Collectively, IMPA1/inositol axis plays a pivotal role in maintaining and promoting the functions of PCSCs and tumor organoid growth from genetic mouse models.

IMPA1 maintains PCSCs via its enzymatic activity independently of its classical role in regulating PI and phosphoinositides

As aforementioned, IMPA1-derived inositol is thought to act primarily through the generation of PI and phosphoinositides thus impacting diverse biological processes. Opposite to the results of IMPA1 knockdown, stable overexpression of IMPA1 increased cancer sphere formation, accompanied by induction of

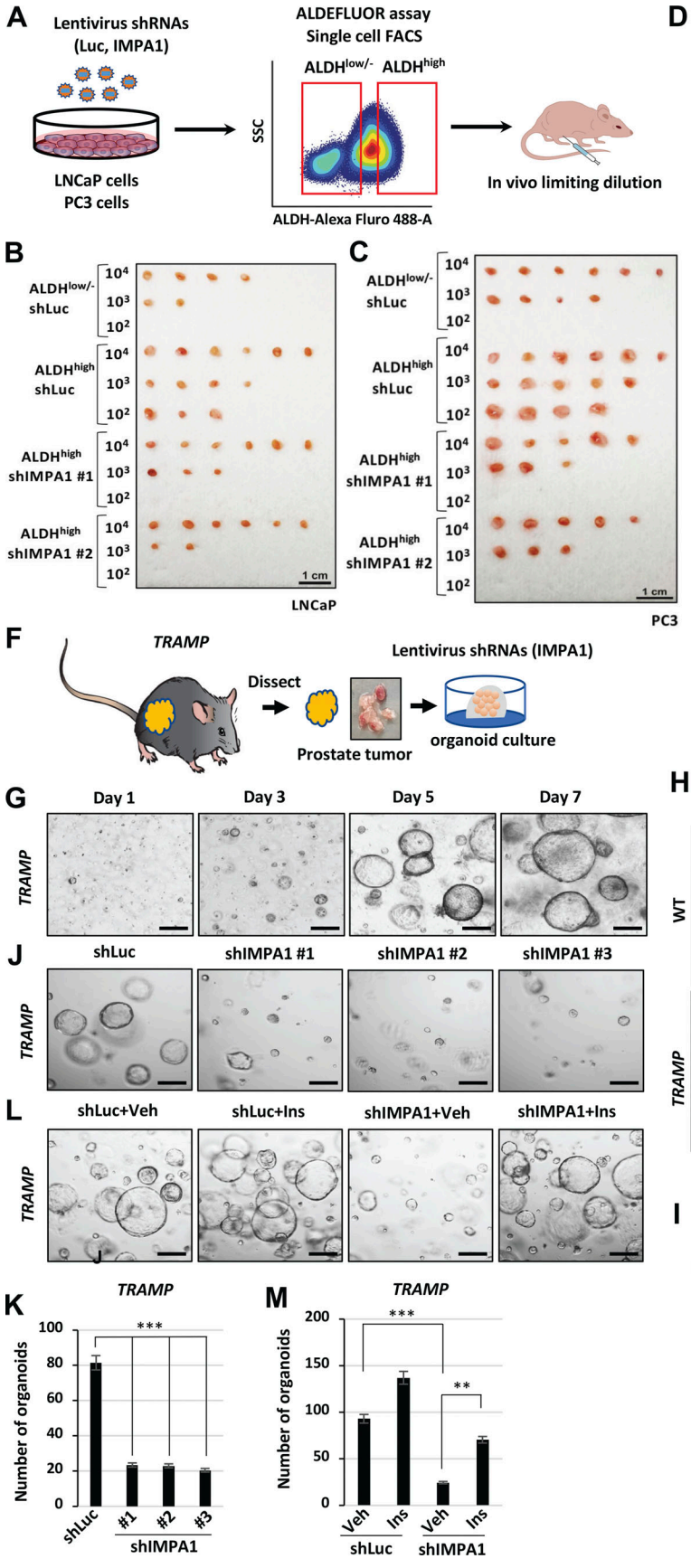

Xenograft LNCaP Line	Cells Transplanted	Tumors	Tumor-initiating frequency
ALDH$^{low/-}$ shLuc	10^4 10^3 10^2	4/6 2/6 0/6	1/6808
ALDH^{high} shLuc	10^4 10^3 10^2	6/6 4/6 3/6	1/553
ALDH^{+} shIMPA1 #1	10^4 10^3 10^2	6/6 3/6 0/6	1/1609
ALDH^{+} shIMPA1 #2	10^4 10^3 10^2	6/6 2/6 0/6	1/2340

Xenograft PC3 Line	Cells Transplanted	Tumors	Tumor-initiating frequency
ALDH^{-} shLuc	10^4 10^3 10^2	6/6 4/6 0/6	1/1072
ALDH^{+} shLuc	10^4 10^3 10^2	6/6 5/6 4/6	1/301
ALDH^{+} shIMPA1 #1	10^4 10^3 10^2	5/6 3/6 0/6	1/3759
ALDH^{+} shIMPA1 #2	10^4 10^3 10^2	5/6 3/6 0/6	1/3759

Figure 2. **IMPA1-derived inositol is required for maintaining ALDH^{high} PCSCs and 3D prostate tumor organoids from CRPC *TRAMP* mouse model.** **(A)** The flow chart shows an experimental outline to demonstrate the tumor-initiating ability of ALDH^{high} cells sorted from LNCaP or PC3 cells stably

expressing shLuc or shIMPA1 (#1 and #2), followed by transplanting 10^4, 10^3, and 10^2 cells into male nude mice for each group. **(B and C)** The image of tumor formation from limiting dilution transplantation using LNCaP (B) and PC3 (C) cells. **(D and E)** Table outlining differences in tumor-initiating frequency of $ALDH^{low/-}$ or $ALDH^{high}$ LNCaP cells (D) and PC3 cells (E) upon limiting dilution transplantation. Tumors arose from transplantation of 10^4, 10^3, and 10^2 $ALDH^{low/-}$ or $ALDH^{high}$ LNCaP cells upon IMPA1 loss. Tumor-initiating frequency was calculated by the ELDA software application for limiting dilution analysis (Hu and Smyth, 2009). **(F)** The flow chart shows prostate tumor organoids are established from male *TRAMP* mice, followed by infection with lentivirus shRNAs of IMPA1. **(G)** Representative images show the growth of prostate tumor organoids from male *TRAMP* mice at the age of 6 mo with indicated days. Scale bar, 200 µm. **(H)** H&E staining and IHC staining with IMPA1 antibody of prostate organoids from WT and *TRAMP* mice at the age of 6 mo. Scale bar, 100 µm for H&E staining; 50 µm for IHC staining. **(I)** Immunoblotting of tumor organoids from male *TRAMP* mice with indicated antibodies. Immunoblotting data were verified in at least two independent experiments. **(J)** Representative images of tumor organoids expressing shLuc or shIMPA1 (#1, #2 and #3) from male *TRAMP* mice. Scale bar, 200 µm. **(K)** Quantification of number of tumor organoids from J was shown as the mean ± SEM of three independent experiments for each group. ***, $P < 0.001$ by two-tailed unpaired *t* test. **(L)** Tumor organoids from male *TRAMP* mice expressing shLuc or shIMPA1 with vehicle (Veh) or 25 µM of inositol (Ins) treatment. Scale bar, 200 µm. **(M)** Quantification of the number of tumor organoids from L for *TRAMP* mice was shown as the mean ± SEM of three independent experiments for each group. **, $P < 0.01$; ***, $P < 0.001$ by two-tailed unpaired *t* test. Source data are available for this figure: SourceData F2.

CSC markers like Oct4 and SOX2 (Fig. S3, A–C). Moreover, the number and size of sphere-forming cells of DU145 and 22RV1 were significantly increased upon inositol treatment in a dose-dependent manner (Fig. S3, D–H). Restoration of IMPA1 expression level in IMPA1 knockout cells by CRISPR double nicking strategy with Cas9 D10A nickase (Ran et al., 2013a) (Fig. S3 I), but not IMPA1-D220A enzymatic dead mutant defective in restoration of inositol level (Fig. 4, A, B, E, and F), rescued the defect in cancer sphere formation (Fig. 4, C, D, G, and H), indicating that phosphatase activity of IMPA1 for inositol generation is essential for maintaining the properties of PCSCs.

To understand whether IMPA1/inositol regulates PCSCs through its known role in the PI cycle, we conducted the rescued experiments by restoring inositol or its downstream metabolites in the PI cycle in cancer sphere assays and tumor organoids from *TRAMP* mouse model. Restoration of inositol, but not of its downstream metabolites, PI, PIP, PIP_2, PIP_3, IP_3, IP_2, and IP, rescued the impairment of cancer sphere formation and tumor organoid growth from *TRAMP* mice upon IMPA1 knockdown (Fig. S3, J–M). Similarly, inositol also rescued cancer sphere formation upon IMPA1 inactivation by LiCl (Fig. S1, O and P). Unlike IMPA1 loss, knockdown of the key enzymes involved in PI and phosphoinositides cycles downstream of IMPA1 including CDP-DAG-inositol 3-phosphatidyl transferase (CDIPT), phosphatidylinositol 4-kinase type 2α (PI4K2α), phospholipase C β1 (PLCβ1), and inositol polyphosphate-1-phosphatase (INPP1), which catalyze the production of inositol's downstream metabolites, PI, PIP, IP_3, and IP, respectively, failed to impair cancer sphere formation (Fig. S3, N–P).

Since inositol is shown to regulate the structure of cell membranes and the levels of insulin and neurotransmitters, we examined whether IMPA1/inositol loss affects the structure of cell membranes and the levels of insulin, dopamine, and glutamate. IMPA1 knockdown did not affect the structure of cell membranes examined by electron microscope (EM) compared with control knockdown (Fig. S3 Q). IMPA1 knockdown also did not change the levels of insulin and neurotransmitters like glutamate and dopamine in $ALDH^{high}$ cells from LNCaP cells and 22RV1 cells compared with control knockdown (Fig. S3, R–T), indicating that inositol inhibition impairs cancer sphere formation, but not cell membrane structure or the levels of insulin and neurotransmitters. Collectively, these results suggest that IMPA1-derived inositol may directly promote cancer stemness of PCSCs independently of its classic mode in serving as a precursor for generating PI and phosphoinositides.

IMPA1/inositol maintains prostate cancer progression using various CRPC xenografts and genetic mouse models

The findings that IMPA1/inositol axis is crucial for maintaining CRPC organoid growth and cancer stemness of PCSCs, which drive cancer initiation and progression, prompted us to hypothesize that IMPA1/inositol is critical for tumorigenesis of CRPC cells. To test this hypothesis, we performed anchorage-independent soft agar assay and xenograft assays to assess prostate cancer cell transformation and tumorigenicity from CRPC cell lines. The soft agar assay revealed that IMPA1 knockdown in CRPC cells abrogated prostate cancer cell transformation potential (Fig. 4, I and J). IMPA1 knockdown also impaired prostate tumorigenicity from three CRPC cell lines (DU145, PC3, and 22RV1) in xenograft assays (Fig. 4, K–Q). Notably, the restoration of inositol partially rescued the tumorigenicity of CRPC cell lines (Fig. 4, O–Q). Collectively, the IMPA1/inositol axis played a pivotal role in maintaining and promoting the tumorigenicity of CRPC cell lines.

We also examined IMPA1 expression in CRPC tumors from *TRAMP* mice (Chiaverotti et al., 2008; Gelman, 2016; Quaglia et al., 2021). Consistently, IMPA1 expression in the CRPC tumor from *TRAMP* mice was significantly upregulated compared with prostate tissue of wild-type (*WT*) mice, correlated with the increased expression of reprogramming factor SOX2 (Fig. 5 A). To further validate the critical role of IMPA1/inositol in prostate cancer progression in *TRAMP* mouse model, we utilized genetic mouse models to establish prostate-specific *Impa1* knockout in *TRAMP* mouse model. To this end, we first generated conditional $Impa1^{flox/+}$ ($Impa1^{FL/+}$) mice by using Cas9/CRISPR editing strategy, as $Impa1^{-/-}$ mice displayed early embryonic lethality (Cryns et al., 2008). We then generated $Impa1^{FL/FL}$ mice by crossing $Impa1^{FL/+}$ mice and $Impa1^{FL/+}$ mice, which were further crossed with *Probasin*-Cre (*PB-Cre4*) mice that selectively express Cre recombinase only in the prostate to generate $Impa1^{FL/FL}$ (referred to as *WT* mice) and $Impa1^{FL/FL}$/*PB-Cre4* mice (Fig. 5 B). Prostate development examined by H&E staining and overall survival rate analyzed by Kaplan–Meier analysis in $Impa1^{FL/FL}$/*PB-Cre4* mice at the age of 7 mo was not altered compared with WT mice (Fig. 5, C, D, and G). We next crossed $Impa1^{FL/FL}$/*PB-Cre4* mice with *TRAMP* mice to generate *TRAMP/PB-Cre4* and *TRAMP*/$Impa1^{FL/FL}$/*PB-Cre4* mice for assessing the role of *impa1* in prostate tumorigenesis in *TRAMP* mouse model. Consistently, *TRAMP/PB-Cre4* mice developed spontaneous tumors in the anterior (AP), ventral (VP), and/or dorsolateral (DLP)

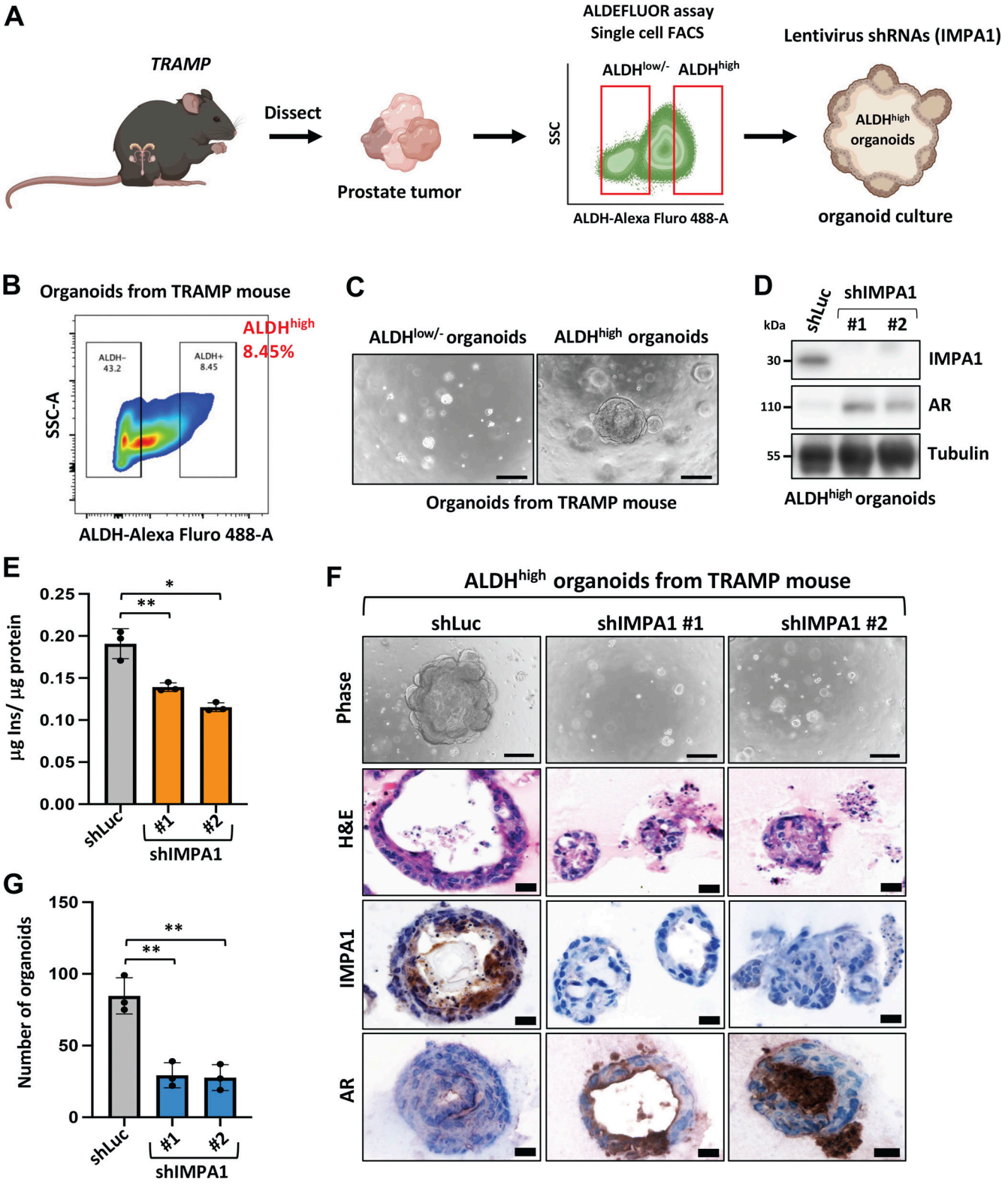

Figure 3. **IMPA1/inositol maintains ALDH^{high} organoids with AR low expression from TRAMP mouse model. (A)** The flow chart shows an experimental outline to demonstrate ALDH^{high} tumor organoids sorted from TRAMP mouse. **(B)** Dot plot of sorted ALDH^{high} and ALDH$^{low/-}$ cell population from TRAMP mouse. **(C)** The phase contrast shows the images of sorted ALDH^{high} and ALDH$^{low/-}$ organoids from TRAMP mouse. Scale bar, 50 µm. **(D)** Immunoblotting of ALDH^{high} and ALDH$^{low/-}$ organoids from TRAMP mouse with indicated antibodies. Immunoblotting data were verified in at least two independent experiments. **(E)** Inositol levels were determined by K-INOSL assay kit. The inositol levels were normalized by protein concentration in each experimental group. Three independent experiments were performed. *, $P < 0.05$; **, $P < 0.01$ by two-tailed unpaired *t* test. **(F)** The phase contrast shows the images of ALDH^{high} organoids upon shLuc, shIMPA1 (#1 and #2). Scale bar, 50 µm. H&E staining and IHC analysis of ALDH^{high} organoids upon shLuc, shIMPA1 (#1 and #2) with indicated antibodies. Scale bar, 20 µm. **(G)** Quantification of ALDH^{high} organoids upon shLuc, shIMPA1 #1 and shIMPA1 #2. The data were shown as the mean ± SEM of three independent experiments for each group. **, $P < 0.01$ by two-tailed unpaired *t* test. Source data are available for this figure: SourceData F3.

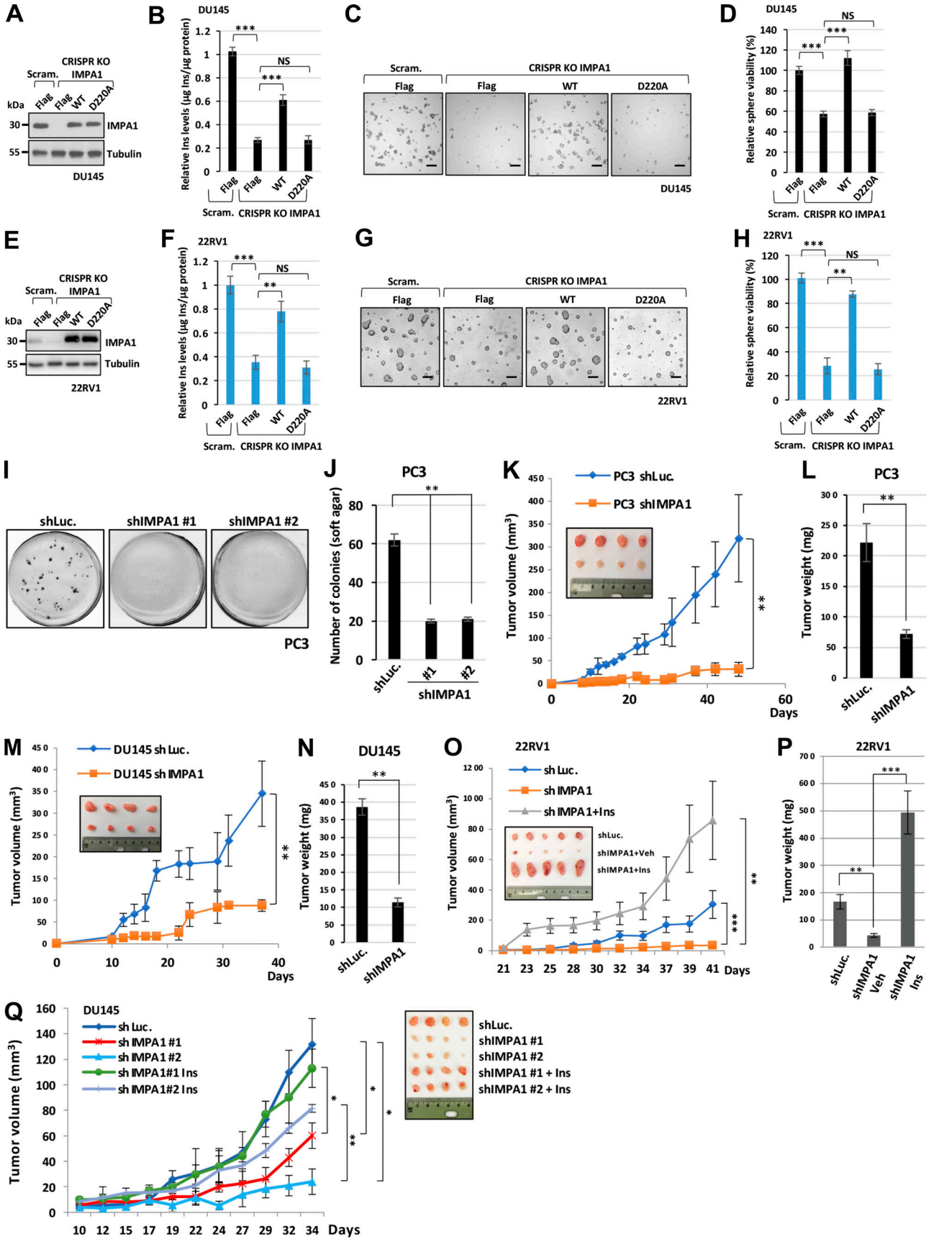

Figure 4. **IMPA1/inositol promotes PCSCs, anchorage-independent growth, and tumorigenicity of CRPC in vivo. (A and E)** Immunoblotting of DU145 (A) and 22RV1 (E) scramble (Scram.) or IMPA1 knockout (KO) cells by CRISPR/Cas9 upon Flag vector, Flag-IMPA1 (WT), and Flag-IMPA1 D220A (D220A)

overexpression with indicated antibodies. Immunoblotting data were verified in at least two independent experiments. **(B and F)** The levels of inositol in DU145 (B) and 22RV1 (F) scramble (Scram.) or IMPA1 knockout by CRISPR/Cas9 cells upon Flag vector, Flag-IMPA1 (WT), and Flag-IMPA1 D220A (D220A) overexpression were determined by K-INOSL assay kit. The inositol levels were normalized by protein concentration in each experimental group. Three independent experiments were performed for the statistic of two-tailed unpaired *t* test. **, P < 0.01; NS, non-significant; ***, P < 0.001 by two-tailed unpaired *t* test. **(C and G)** Representative images of spheres from DU145 (C) and 22RV1 (G) scramble (Scram.) or IMPA1 knockout cells upon Flag vector, Flag-IMPA1 (WT), and Flag-IMPA1 D220A (D220A) overexpression. Scale bar, 100 µm. **(D and H)** Quantification of the number of spheres from DU145 (D) and 22RV1 (H) is shown as the mean ± SEM of three independent experiments for each group. **, P < 0.01; ***, P < 0.001; NS, non-significant by two-tailed unpaired *t* test. **(I)** Soft agar assay is shown in PC3 cells stably expressing shLuc or IMPA1-two specific shRNA lentivirus (#1 and #2). **(J)** Quantification of the number of colonies formation in soft agar by ImageJ in I is shown as the mean ± SEM of three independent experiments for each group. **, P < 0.01 by two-tailed unpaired *t* test. **(K and M)** Tumorigenicity of PC3 (K) or DU145 (M) cells stably expressing shLuc or shIMPA1 was determined by tumor volume. At least four xenograft tumors in each group were quantified. **, P < 0.001 by two-tailed unpaired *t* test. **(L and N)** Tumor weight from PC3 (L) or DU145 (M) cells stably expressing shLuc or shIMPA1 was measured at day 48 (L) and day 38 (N). At least four xenograft tumors in each group were quantified. **, P < 0.01 by two-tailed unpaired *t* test. **(O)** Nude mice subcutaneously injected with 22RV1 cells stably expressing shLuc or shIMPA1 were intraperitoneally injected with vehicle or 30 mg/kg of inositol every 2 days until 41 days, and tumor volume was measured with indicated days. At least five xenograft tumors in each group were quantified. **, P < 0.001; ***, P < 0.001 by two-tailed unpaired *t* test. **(P)** Tumor weight from 22RV1 cells stably expressing shLuc or shIMPA1 upon intraperitoneal injection with vehicle or 30 mg/kg of inositol every 2 days at day 41 was measured. At least five xenograft tumors in each group were quantified. **, P < 0.01; ***, P < 0.001 by two-tailed unpaired *t* test. **(Q)** Nude mice subcutaneously injected with DU145 cells stably expressing shLuc or shIMPA1 (#1 and #2) were intraperitoneally injected with vehicle or 50 mg/kg of inositol every 2 days until 34 days, and tumor volume was measured with indicated days. At least four xenograft tumors in each group were quantified. *, P < 0.05; **, P < 0.01 by two-tailed unpaired *t* test. Source data are available for this figure: SourceData F4.

lobes of the prostate. We found that all *TRAMP/PB-Cre4* mice (n = 15) developed massive prostate tumor mass in DLP at the age of 7–8 mo. Remarkably, none of *TRAMP/Impa1*$^{FL/FL}$*/PB-Cre4* mice (n = 15) developed noticeable tumors in DLP at aged-matched mice (Fig. 5 C). Histopathological analyses revealed significant invasive carcinoma and CRPC tumors in AP and DLP in *TRAMP/PB-Cre4* mice at the age of 7 mo; however, normal prostate gland in AP or dysplasia/hyperplasia in DLP was found in age-matched *TRAMP/Impa1*$^{FL/FL}$*/PB-Cre4* mice (Fig. 5 D). *TRAMP/Impa1*$^{FL/FL}$*/PB-Cre4* mice also significantly reduced ALDH^{high} PCSCs in the prostate compared with *TRAMP/PB-Cre4* mice (Fig. 5, E and F). The survival analysis revealed that *TRAMP/PB-Cre4* mice significantly reduced mouse survival rate and all mice died before 34 wk of age (Fig. 5 G). Notably, *TRAMP/Impa1*$^{FL/FL}$*/PB-Cre4* mice dramatically prolonged survival rate and extended lifespan over 34 wk of age compared with *TRAMP/PB-Cre4* mice (Fig. 5 G). Collectively, genetic loss of *Impa1* in the prostate abrogates PCSC population in vivo, prostate tumorigenicity, and prolongs the survival rate in the *TRAMP* mouse model.

The prognostic values and clinical significance of IMPA1/inositol axis in advanced human prostate cancer

To understand the clinical significance and prognostic value of IMPA1/inositol axis in human prostate cancer, we determined the IMPA1/inositol expression in prostate cancer specimens. By analyzing TCGA datasets, we found that IMPA1 was overexpressed in diverse cancer types including prostate cancer (Data S1). Consistently, IMPA1 expression was also significantly upregulated in prostate cancer patients compared with normal counterparts by analyzing prostate cancer cohorts from a number of published literature (Data S1).

By analyzing cBioPortal databases obtained from 16 prostate cancer studies with 4,104 samples and 3,886 prostate cancer patients, *IMPA1* gene amplification was found significantly in 16 prostate cancer studies (Fig. S4 A). The database from Gene Expression Profiling Interactive Analysis (GEPIA) revealed that *IMPA1* gene expression is significantly upregulated in most tumor samples (N = 492) compared with normal tissues (N = 152) (Fig. S4 B). Importantly, Kaplan–Meier survival analysis from 1,278 prostate patients according to cBioPortal databases obtained from 16 prostate cancer studies revealed that IMPA1 amplification was associated with poor survival outcomes (Fig. S4 C). Additionally, we also used PrognoScan to analyze the overall survival rate of patients with high or low IMPA1 expression. PrognoScan database revealed that high expression of IMPA1 is significantly correlated with poor overall survival in prostate cancer compared with low expression of IMPA1 (Fig. S4 D). Collectively, these data underscore the clinical importance of IMPA1 overexpression in prostate cancer progression.

To understand the clinical significance and potential biomarker of IMPA1-derived inositol in prostate cancer, we detected inositol levels in serum samples from 20 normal people and 29 prostate cancer patients enrolled in Wake Forest Baptist Cancer Center. Notably, inositol was significantly upregulated in the serum from prostate cancer patients compared with normal counterparts (Fig. 5 H, P < 0.0001), indicating that inositol is a potential biomarker to predict prostate cancer formation. Consistently, IHC staining from adjacent normal (80 cases) and prostate cancer (80 cases) in our in-house prostate cancer samples revealed that high IMPA1 protein expression is detected in human prostate cancer with high Gleason score compared with normal prostate and predicts poor survival outcome (Fig. 5, I–K), establishing the clinical significance of IMPA1/inositol axis in prostate cancer progression.

IMPA1-derived inositol serves as a key cofactor to activate IMPDH2 for the synthesis of guanylate nucleotides

The finding that IMPA1-derived inositol, but not its downstream metabolites, maintains cancer stemness and tumor organoid growth indicates that inositol may have its direct protein targets, which have not been well understood. Inspired by our recent study and other reports that indicated the unique role of certain metabolites such as lactate in regulating cellular functions through their direct protein targeting (Carey et al., 2015; Lu and Thompson, 2012; Zhang et al., 2019), we then sought to identify the direct targets of inositol responsible for inositol-mediated PCSC regulation. To achieve this goal, we synthesized biotin-

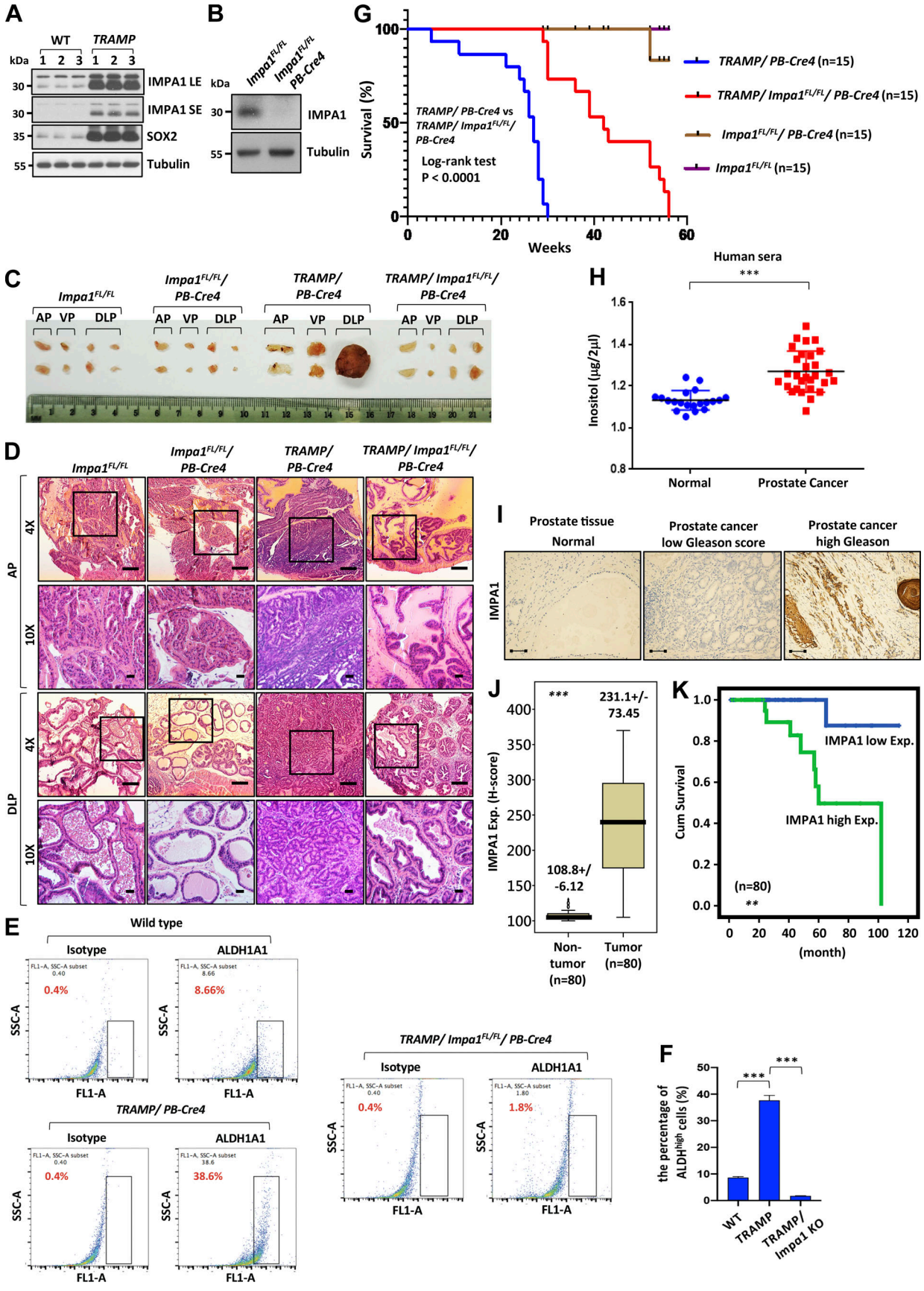

Figure 5. ***Impa1* deficiency abrogates CRPC progression in *TRAMP* mouse model and IMPA1/inositol is upregulated in prostate cancer patients and CRPC patients and correlates with poor survival outcome. (A)** Immunoblotting of prostate tissue from male C57BL/6J WT (*n* = 3) and *TRAMP* (*n* = 3) mice of

8 mo with indicated antibodies. LE, long exposure; SE, short exposure. Immunoblotting data were verified in at least two independent experiments. **(B)** Immunoblotting of prostate tissue from *Impa1*$^{FL/FL}$ and *Impa1*$^{FL/FL}$*/PB-Cre4* with indicated antibodies. *Impa1*$^{FL/FL}$, *Impa1*$^{FL/FL}$*/PB-Cre4*, *TRAMP/PB-Cre4*, and *TRAMP/Impa1*$^{FL/FL}$*/PB-Cre4* mice were generated from four generations of backcrossing to maintain in C57BL/6J background. All mice were intercrossed to generate pups, followed by genotyping to group the age-matched mice for each experimental group. Immunoblotting data were verified in at least two independent experiments. **(C)** Representative images of AP, VP, and DLP lobes of the prostate from *Impa1*$^{FL/FL}$, *Impa1*$^{FL/FL}$*/PB-Cre4, TRAMP/PB-Cre4*, and *TRAMP/Impa1*$^{FL/FL}$*/PB-Cre4* mice at the age of 7 mo. **(D)** H&E staining of AP and DLP lobes of prostate from *Impa1*$^{FL/FL}$, *Impa1*$^{FL/FL}$*/PB-Cre4*, *TRAMP/PB-Cre4*, and *TRAMP/Impa1*$^{FL/FL}$*/PB-Cre4* mice at the age of 7 mo with 4× and 10× magnification (three mice for each group). Scale bar for 4× magnification, 500 µm; scale bar for 10× magnification, 100 µm. **(E)** ALDH1A1 cell population from the prostate tissue of WT, *TRAMP/PB-Cre4* or *TRAMP/Impa1*$^{FL/FL}$*/PB-Cre4* mice was determined by flow cytometry analysis using isotype and ALDH1A1 antibody. **(F)** The percentage of ALDH1A1 (ALDH^{high}) cells from prostate tissue was quantified from E shown as the mean ± SEM of three independent experiments for each group (three mice for each group). *TRAMP*, *TRAMP/PB-Cre4* mice, and *TRAMP/Impa1 KO*, *TRAMP/Impa1*$^{FL/FL}$*/PB-Cre4* mice. ***, P < 0.001 by two-tailed unpaired *t* test. **(G)** Kaplan–Meier survival plots of *Impa1*$^{FL/FL}$, *Impa1*$^{FL/FL}$*/PB-Cre4*, *TRAMP/PB-Cre4*, and *TRAMP/Impa1*$^{FL/FL}$*/PB-Cre4* mice (15 mice for each group). P < 0.0001 by log–rank test. **(H)** The levels of inositol in the sera of normal male people (n = 20) and prostate cancer patients (n = 29) were determined by K-INOSL assay kit. ***, P < 0.001 by two-tailed unpaired *t* test. **(I)** IMPA1 protein expression from adjacent normal and prostate cancer patient with low or high Gleason score in our in-house prostate cancer samples was determined by IHC staining. Scale bar, 20 µm. **(J)** Box plot represents IMPA1 expression in adjacent normal (80 cases) and prostate cancer patients with high Gleason score and advanced stage (80 cases). ***, P < 0.001 by Mann–Whitney U test. **(K)** Disease-specific survival outcome with IMPA1 low or high expression was shown by Kaplan–Meier plots in prostate cancer patients with high Gleason score and advanced stage (80 cases). **, P = 0.0091 by long–rank test. Source data are available for this figure: SourceData F5.

labeled inositol and mixed biotin or biotin-labeled inositol with the whole cell extracts from prostate cancer cells, followed by biotin–streptavidin pull-down for systematic mass spectrometry analysis (Hsu et al., 2022) (Fig. 6 A). Using this systematic approach, we uncovered numerous potential inositol-interacting proteins including IMPDH2 (inosine-5′-monophosphate dehydrogenase 2) (Table S1). We focused on IMPDH2 because it is the rate-limiting enzyme for the synthesis of guanylate nucleotides involved in renal cancer progression (Valvezan et al., 2017). We verified the interaction between inositol and IMPDH2 by incubating biotin-labeled inositol with prostate cancer cell lysates, followed by a biotin pull-down assay (Fig. 6 B). Inositol not only pulled down IMPDH2 from cell extracts but also directly interacted with recombinant IMPDH2 protein through in vitro binding assay (Fig. 6 C). Further in vitro mapping experiments revealed that inositol binds to both the N-terminus and C-terminus regions of IMPDH2 (Fig. 6, D and E).

Active IMPDH2 protein forms a tetramer and extends the contacts between the barrel of adjacent monomers to stabilize the protein complex (Sintchak et al., 1996). IMPDH2 tetramer-related contacts are made between adjacent barrels near the N- and C-terminus. 41–43 amino acids form a β strand parallel with 279–281 amino acids in an adjacent subunit (Sintchak et al., 1996). Based on our in vitro biotin-labeled inositol pull-down assay, we found inositol binds to the N-terminal (1–111 aa) and C-terminal (232–514 aa) of IMPDH2 but not the CBS domain (111–232 aa) in vitro (Fig. 6, D and E). To align the sequence of the N-terminal (1–111 aa) and C-terminal (232–514 aa) of IMPDH2, we did not find the conserved sequence in these two regions. Given that 41–43 and 279–281 aa of IMPDH2 make tetramer-related contacts between adjacent barrels and also are residues in the N- and C-terminus, respectively, this prompted us to make a hypothesis that inositol binds to IMPDH2 to maintain the formation of tetramer/oligomer of IMPDH2.

To test this hypothesis, we examined the tetramer/oligomer of IMPDH2 using a crosslinking assay in 22RV1 cells. Inositol decline by IMPA1 knockdown reduced tetramer/oligomer of IMPDH2, accompanied by the increase of monomer of IMPDH2 (Fig. 6 F). Remarkably, restoration of inositol dramatically rescued the defect of tetramer/oligomer of IMPDH2 upon IMPA1 knockdown (Fig. 6 G). In vitro IMPDH2 oligomerization assay also revealed that inositol significantly promotes dimerization/oligomerization of recombinant IMPDH2 protein, accompanied by a reduced monomer of recombinant IMPDH2 protein in a dose-dependent manner (Fig. 6 H). These results indicate that IMPA1-derived inositol maintains dimerization/oligomerization of IMPDH2.

To identify the IMPDH2 mutants that lose the binding to inositol, we truncated 41–43 aa (IMPDH2$^{\Delta 41-43}$) and 279–281 aa (IMPDH2$^{\Delta 279-281}$) of IMPDH2, followed by biotin-inositol pull-down assay (Fig. 6 I). Both recombinant IMPDH2$^{\Delta 41-43}$ or IMPDH2$^{\Delta 279-281}$ proteins lost their binding to inositol compared with recombinant IMPDH2 full-length proteins (IMPDH2^{FL}) (Fig. 6 J). Hence, 41–43 and 279–281 aa of IMPDH2 both are critical residues for inositol binding.

It has been established that the structure of IMPDH2 forms the complex with MPA, which is an inhibitor of IMPDH, and an IMP reaction intermediate during substrate turnover (Burrell and Kollman, 2022; Sintchak et al., 1996). Both MPA and an IMP intermediate are bound in the active site, Cystein-331, simultaneously (Sintchak et al., 1996). To further demonstrate whether MPA or IMP can compete with inositol binding to IMPDH2, we performed in vitro biotin-labeled inositol pull-down assay again. We found that MPA or IMP did not disrupt inositol binding to IMPDH2, but excessive unlabeled inositol disrupted the binding between biotin-labeled inositol and IMPDH2 (Fig. 6 K).

We also examined the binding between inositol and IMPDH1, which displays a metabolic function similar to IMPDH2. Biotin pull-down assay revealed that IMPDH1 and IMPDH2 both could bind to inositol in 22RV1 cells (Fig. 6 L). IMPDH2 mainly expresses in proliferative cells like cancer cells, while IMPDH1 generally expresses in cells as a housekeeping gene (Jackson et al., 1975; Senda and Natsumeda, 1994). We then examined the expression of IMPDH1 and IMPDH2 in various prostate cancer cell lines. Consistently, IMPDH2, but not IMPDH1, was significantly upregulated in diverse prostate cancer cell lines compared with normal prostate epithelial cells, PNT1A

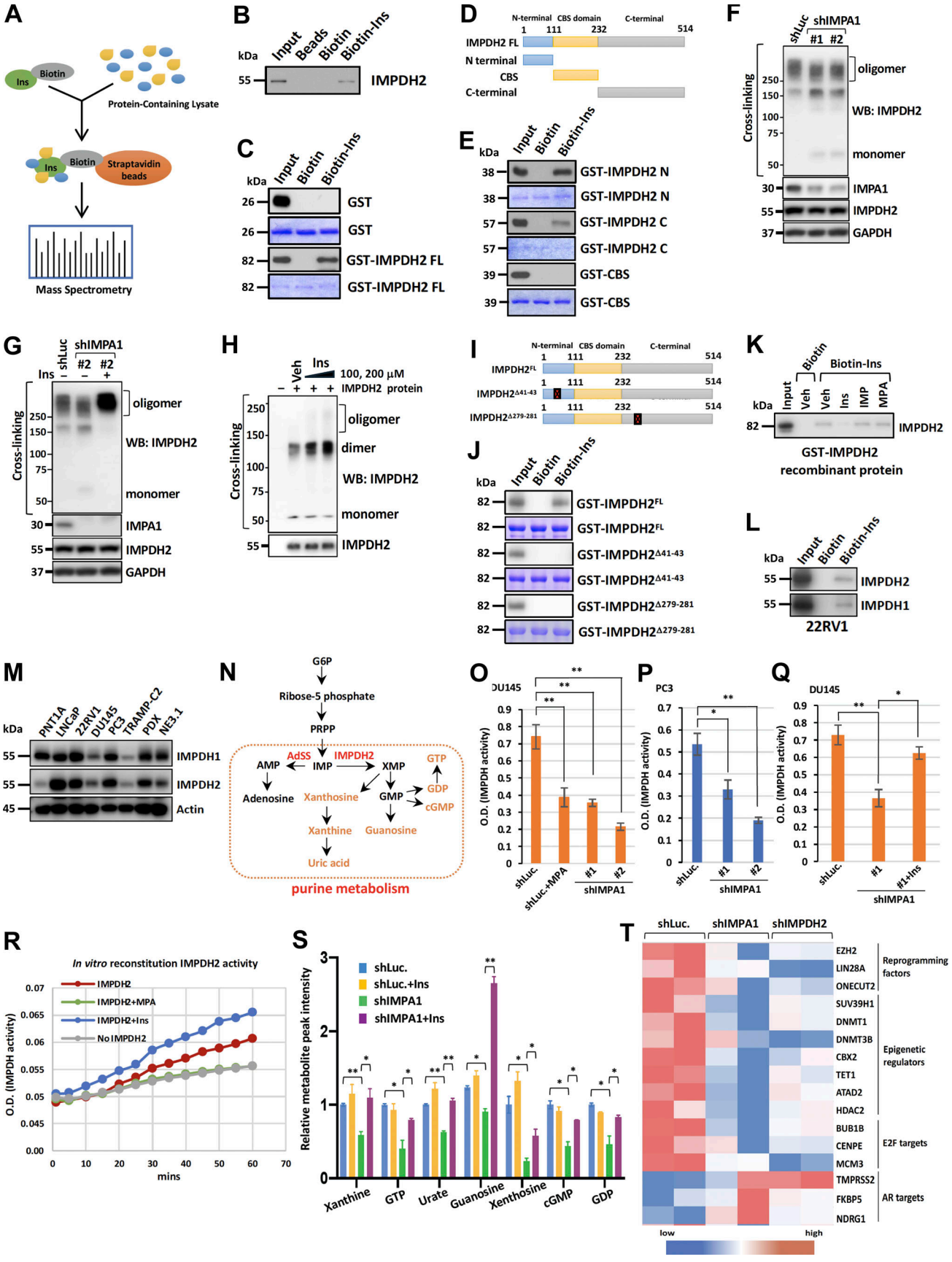

Figure 6. **Inositol maintains IMPDH2 oligomerization, directly binds to IMDPH2, and activates IMPAH2 activity, thereby promoting guanylate purine metabolism. (A)** The cell lysates from PC3 cells were incubated with biotin or biotin-labeled inositol, and inositol-interacting proteins were pulled down by

streptavidin beads and subjected to mass spectrometry. **(B)** The cell lysates from PC3 cells were incubated with 40 μM of biotin or biotin-labeled inositol, pulled down with streptavidin beads and subjected to immunoblotting with IMPDH2 antibody. Immunoblotting data were verified in at least two independent experiments. **(C)** GST and GST-IMPDH2 full length (FL) were expressed in *Escherichia coli* BL21 cells and immobilized on Glutathione-Sepharose. 2 μg of these recombinant proteins were incubated with 40 μM of biotin or biotin-labeled inositol (Biotin-Ins) for 3 h, followed by pulled down with streptavidin beads. The interaction was determined by immunoblotting with indicated antibodies. The purity of the recombinant proteins was resolved by SDS-PAGE, followed by Coomassie blue staining. **(D)** The illustration of the IMPDH2 full length (1–514 aa), the N-terminal (1–111 aa), CBS (111–232 aa), and C-terminal (232–514 aa). **(E)** GST-IMPDH2 N-terminal, GST-IMPDH2 C-terminal, and GST-CBS domain from IMPDH2 were expressed in *Escherichia coli* BL21 cells and immobilized on Glutathione-Sepharose. 2 μg of these recombinant proteins was incubated with 40 μM of biotin or biotin-labeled inositol (Biotin-Ins) for 3 h, followed by pulled down with streptavidin beads. The interaction was determined by immunoblotting with indicated antibodies. The purity of the recombinant proteins was resolved by SDS-PAGE, followed by Coomassie blue staining. Immunoblotting data were verified in at least two independent experiments. **(F)** 22RV1 cell lysates upon shLuc and shIMPA1(#1 and #2) were subjected to crosslinking by bismaleimidohexane (BHM), followed by immunoblotting with IMPDH2 antibody. The input levels of IMPA1, IMPDH2, and GAPDH were represented without crosslinking. Immunoblotting data were verified in at least two independent experiments. **(G)** 22RV1 cell lysates upon shLuc and shIMPA1(#2) with the treatment of vehicle and 100 μM of inositol were subjected to cross-link by bismaleimidohexane (BHM), followed by immunoblotting with IMPDH2 antibody. The input levels of IMPA1, IMPDH2, and GAPDH were represented without cross-link. Immunoblotting data were verified in at least two independent experiments. **(H)** Recombinant IMPDH2 protein incubated with vehicle and 100, 200 μM of inositol were subjected to cross-link by BMH, followed by immunoblotting with IMPDH2 antibody. The input levels of IMPDH2 were represented without cross-link. Immunoblotting data were verified in at least two independent experiments. **(I)** The illustration of the IMPDH2 full length ($IMPDH2^{FL}$), truncated 41–43 aa of IMPDH2 ($IMPDH2^{\Delta41-43}$) and truncated 279–281 aa of IMPDH2 ($IMPDH2^{\Delta279-281}$). **(J)** Recombinant proteins, GST- $IMPDH2^{FL}$, GST-$IMPDH2^{\Delta41-43}$ and GST-$IMPDH2^{\Delta279-281}$, were subjected to biotin and biotin-labeled inositol pull-down assay, followed by immunoblotting with GST antibody. Coomassie blue indicates the equal amount of recombinant proteins in each group. Immunoblotting data were verified in at least two independent experiments. **(K)** Recombinant GST- $IMPDH2^{FL}$ protein were subjected to 40 μM of biotin and 40 μM of biotin-labeled inositol pull-down assay upon adding 1 mM of IMP, 75 nM of MPA and excessive 500 μM of inositol, followed by immunoblotting with IMPDH2 antibody. Immunoblotting data were verified in at least two independent experiments. **(L)** 22RV1 cell lysates were subjected to biotin and biotin-labeled inositol pull-down assay, followed by immunoblotting with indicated antibodies. Immunoblotting data were verified in at least two independent experiments. **(M)** Immunoblotting of various prostate cancer cell lines with indicated antibodies. Immunoblotting data were verified in at least two independent experiments. **(N)** Schematic representation of purine metabolism with a series of enzymes and metabolites. **(O and P)** The activity of IMPDH was measured in DU145 (O) and PC3 (P) stably expressing shLuc or shIMPA1 (#1 and #2) upon 10 μM of MPA treatment by using IMPDH activity assay kit. The detailed procedure is described in Materials and methods. The activity was normalized by protein concentration in each experimental group. The data were shown as the mean ± SEM of three independent experiments for each group. *, $P < 0.05$; **, $P < 0.01$ by two-tailed unpaired *t* test. **(Q)** The activity of IMPDH was measured in DU145 cells stably expressing shLuc or shIMPA1 upon 25 μM of inositol (Ins) treatment by using IMPDH activity assay kit. The data were shown as the mean ± SEM of three independent experiments for each group. *, $P < 0.05$; **, $P < 0.01$ by two-tailed unpaired *t* test. **(R)** In vitro IMPDH2 activity using IMPDH activity assay kit was determined by incubation recombinant IMPDH2 protein with 40 μM of inositol (Ins) or 10 μM of MPA with indicated time. **(S)** Targeted metabolomics of PC3 cells expressing shLuc or shIMPA1 upon 25 μM of inositol (Ins) treatment was performed to measure the levels of purine metabolism including guanosine, xanthosine, cGMP, GDP, xanthine, GTP, Urate. The data were shown as the mean ± SEM of three independent experiments for each group. *, $P < 0.05$; **, $P < 0.01$ by two-tailed unpaired *t* test. **(T)** Heatmap plot from RNA-seq shows the expression levels of reprogramming factors, epigenetic factors, E2F targets, and AR targets in CRPC 22RV1 cells stably expressing shLuc, shIMPA1, or shIMPDH2. Duplicate RNA samples in each group were performed for RNA-seq. Source data are available for this figure: SourceData F6.

(Fig. 6 M). Collectively, these results suggest that inositol binds to 41–43 and 279–281 aa of IMPDH2 to maintain the tetramer/oligomer of IMPDH2.

IMPDH2 is a key rate-limiting enzyme that converts inosine monophosphate (IMP) to xanthosine 5′-monophosphate for subsequently generating purine/guanine nucleotides crucial for DNA and RNA synthesis through an NAD-dependent manner (Fig. 6 N). It is important to note that the regulatory mechanisms by which IMPDH2 activity is regulated remain largely unknown. Given inositol directly binds to IMPDH2, we asked the question of whether inositol could regulate IMPDH2 activity in cells. Of note, the knockdown of IMPA1 in two CRPC lines markedly reduced IMPDH2 activity, similar to the treatment of the specific IMPDH inhibitor, mycophenolic acid (MPA) (Fig. 6, O and P). Restoration of inositol in IMPA1 knockdown cells fully rescued IMPDH2 activity (Fig. 6 Q). In an in vitro reconstitution IMPDH2 activity assay, we demonstrated that inositol could directly enhance IMPDH activity, which was abrogated by MPA (Fig. 6 R).

Since IMPA1/inositol maintains IMPDH2 activity in cells and in vitro, which orchestrates guanine metabolism, the knockdown of IMPA1 led to a marked reduction in the level of a series of guanylate nucleotides including guanosine, xanthosine, xanthine, uric acid, cGMP, GDP and GTP, as determined by metabolomics analysis (Fig. 6 S). Notably, a reduction in the level of these guanylate nucleotides in IMPA1 knockdown cells could be rescued by inositol restoration (Fig. 6 S). These results collectively suggest that IMPA1-derived inositol serves as a direct activator for IMPDH2 leading to maintaining the synthesis of guanylate nucleotides.

IMPDH2 mediates the functional role of IMPA1/inositol in maintaining PCSCs

We then determined whether IMPDH2 acts as a key sensor of inositol to maintain the properties of PCSCs. IMPDH2 activity in spheroid cells from CRPC 22RV1 cells was significantly higher than that in adherent cells (Fig. 7 A). Consistently, guanosine and guanosine 5′-monophosphate (GMP) levels were also upregulated in $ALDH^{high}$ PCSCs compared with $ALDH^{low/-}$ non-PCSCs, correlating with upregulated IMPA1/inositol axis (Fig. 7 B). Strikingly, both the knockdown of IMPDH2 and pharmacological inhibition of IMPDH2 by MPA decreased prostate cancer sphere formation (Fig. 7, C–F and N–P; and Fig. S2, M–O) and $ALDH^{high}$ PCSC populations (Fig. 7, G and H), similar to knockdown of IMPA1 or pharmacological inhibition of IMPA1 by LiCl (Fig. 1, E–M; Fig. S1, M and N; Fig. S1, O–V; and Fig. S2, M–O).

Given that IMPDH2 modulates several downstream metabolites involved in IMP signaling pathway (Fig. 6 N), we raised the question of whether IMPA1/inositol regulates PCSCs through the

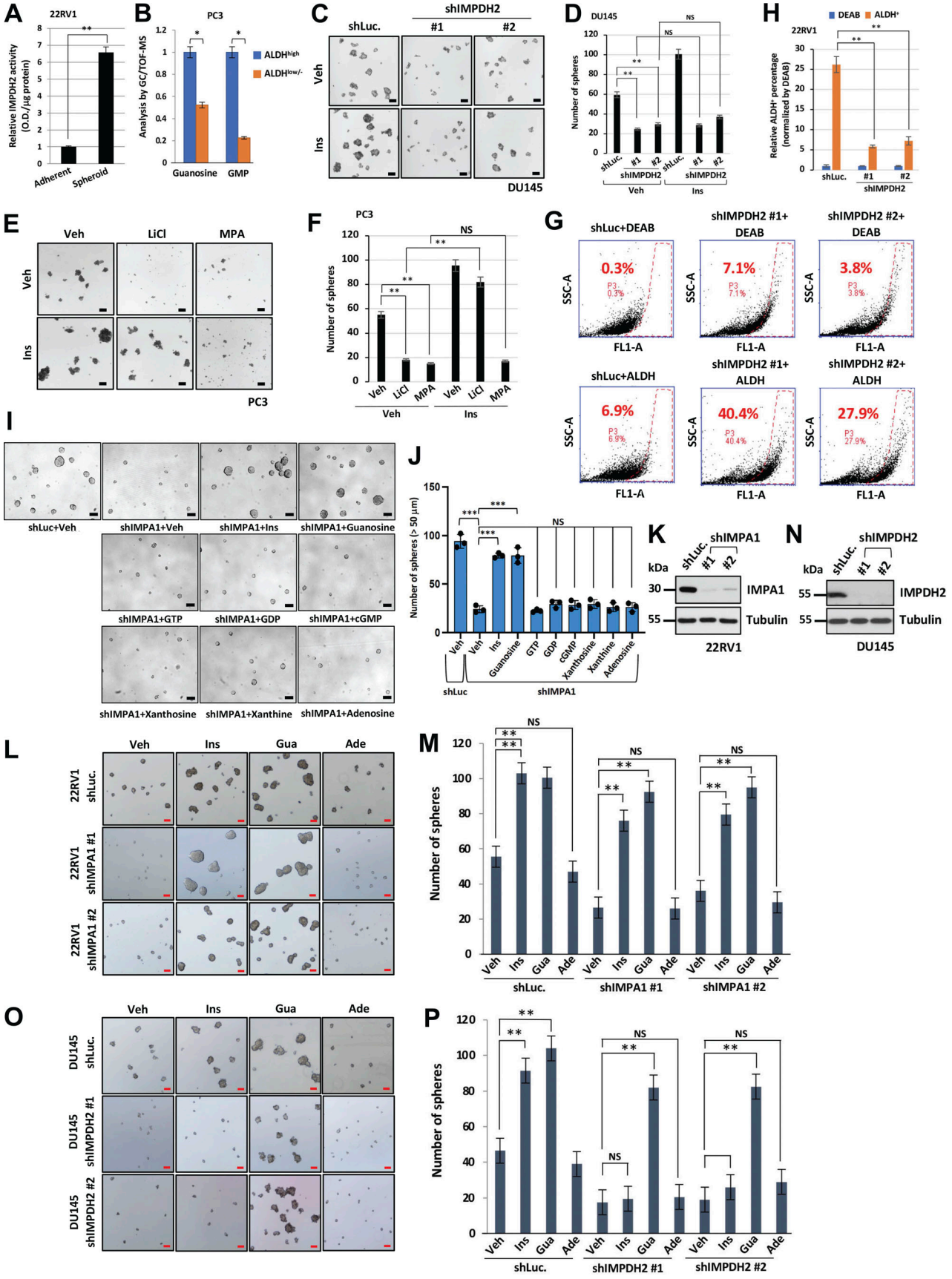

Figure 7. **Inositol promotes PCSCs via directly binding to IMPDH2. (A)** IMPDH activity of adherent and spheroid in 22RV1 cells. The activity was normalized by protein concentration in each experimental group. The data were shown as the mean ± SEM of three independent experiments for each group. **, P < 0.01

by two-tailed unpaired *t* test. **(B)** The levels of guanosine and GMP in ALDH^{high} and ALDH$^{low/-}$ of PC3 cells were determined by metabolomics analysis. *, P < 0.05 by two-tailed uppaired *t* test. **(C)** Spheres from DU145 stably expressing shLuc or shIMPDH2 (#1 and #2) upon the treatment of vehicle (Veh) or 40 µM of inositol (Ins). Scale bar, 100 µm. **(D)** Quantification of the number of spheres from DU145 is shown in C. The data are shown as the mean ± SEM of three independent experiments for each group. **, P < 0.01; NS, non-significant by two-tailed unpaired *t* test. **(E)** Spheres from PC3 cells upon 500 µM of LiCl, 10 µM of MPA, or 25 µM of Ins treatment for 4 days. Scale bar, 100 µm. **(F)** Quantification of sphere number from PC3 by ImageJ shown in E. The data are shown as the mean ± SEM of three independent experiments for each group. **, P < 0.01; NS, non-significant by two-tailed unpaired *t* test. **(G)** 22RV1 cells stably expressing shLuc or shIMPDH2 (#1 and #2) incubated with ALDEFLUOR for 45 min. FACS profiles represent DEAB control and ALDH staining in each group. The gate (P3) was set according to DEAB control. **(H)** Quantification of relative ALDH positive cells normalized by DEAB control according to the gate (P3) is shown as the mean ± SEM of three independent experiments for each group. **, P < 0.01 by two-tailed unpaired *t* test. DEAB, ALDH inhibitor. **(I)** Cancer sphere formation in 22RV1 cells expressing shLuc and shIMPA1 #1 upon vehicle, 40 µM of inositol, 40 µM of guanosine, 100 µM of GTP, 100 µM of GDP, 50 µM of cGMP, 3 µM of xanthosine, 3 µM of xanthine and 40 µM of adenosine. The concentrations of treatment were close to the reported physiological ranges (Traut, 1994). Scale bar, 100 µm. **(J)** Quantification of the number of cancer sphere formations with over 50 µm of diameter from A. The data were shown as the mean ± SEM of three independent experiments for each group. ***, P < 0.001; NS, non-significant by two-tailed unpaired *t* test. **(K and N)** Immunoblotting of 22RV1 (N) stably expressing shLuc or shIMPA1 (#1 and #2) and DU145 (Q) stably expressing shLuc or shIMPDH2 (#1 and #2) with indicated antibodies. Immunoblotting data were verified in at least two independent experiments. **(L and O)** Spheres from 22RV1 (L) or DU145 (O) stably expressing shLuc, IMPA1-two specific shRNA lentivirus (#1 and #2), or IMPDH2-two specific shRNA lentivirus (#1 and #2) upon vehicle (Veh), 40 µM of inositol (Ins), 40 µM of guanosine (Gua) or 40 µM of adenosine (Ade) treatment for 4 days. Scale bar, 100 µm. **(M and P)** Quantification of the number of spheres from L and O for M and P, respectively, was shown. Data are shown as the mean ± SEM of three independent experiments for each group. **, P < 0.01; NS, non-significant by two-tailed unpaired *t* test. Source data are available for this figure: SourceData F7.

downstream metabolites associated with IMP signaling. In general, purine bases enter cells through facilitated diffusion and transport carriers responsible for subsequent intracellular metabolism (Berlin and Oliver, 1975). While IMPA1 loss displayed the defect in cancer sphere formation in 22RV1 cells, restoration of inositol or guanosine, but not other downstream metabolites like GTP, GDP, cGMP, xanthosine, xanthine, and adenosine, could rescue this defect (Fig. 7, I–M). However, restoration of guanosine, which is converted from GMP in IMPDH2-mediated guanylate nucleotide pathway (Fig. 6 N), but not inositol or adenosine, which is converted from AMP in adenylosuccinate synthetase (AdSS)-mediated adenylate nucleotides pathway (Fig. 6 N), rescued the defect in cancer sphere formation upon IMPDH2 knockdown or inhibition (Fig. 7, N–P; and Fig. 7, C–F).

To further demonstrate whether IMPA1/inositol/IMPDH2 axis is specific to maintain the proliferation of PCSCs, we restored inositol and guanosine levels in ALDH^{high} cells isolated from LNCaP and TRAMP-C2 upon IMPA1 knockdown. Restoration of inositol or guanosine could rescue the defect of cell proliferation in ALDH^{high} cells upon IMPA1 knockdown from LNCaP and TRAMP-C2 (Fig. S2, P–U). However, restoration of guanosine, but not inositol, could rescue the defect of cell proliferation in ALDH^{high} cells upon IMPDH2 knockdown from LNCaP and TRAMP-C2 (Fig. S2, P–U), suggesting that IMPA1/inositol acts through IMPDH2 to specifically maintain the cell proliferation of ALDH^{high} PCSCs. However, neither inositol nor guanosine restoration could change cell proliferation in ALDH$^{low/-}$ cells upon IMPA1 or IMPDH2 knockdown from LNCaP and TRAMP-C2 (Fig. S2, P–S, V, and W). Collectively, IMPA1/inositol acts through IMPDH2 to specifically maintain the properties of ALDH^{high} PCSCs.

IMPA1/inositol axis maintains PCSCs with AR$^{low/-}$ features through activating IMPDH2, which maintains CRPC progression

It has been established that the conversion of AR^{+} adenocarcinoma to AR$^{low/-}$ CRPC is one of the key features during CRPC progression, a process that is referred to as lineage plasticity. Recent studies indicated that simultaneous loss of *p53* and *pRB* caused SOX2 and EZH2 upregulation for lineage plasticity leading to CRPC progression (Ku et al., 2017; Mu et al., 2017). Hence, the acquisition of AR$^{low/-}$ PCSCs may represent key cellular features during ABT treatment and CRPC progression. Indeed, ALDH^{high} PCSCs isolated from AR-positive 22RV1 and LNCaP cells also displayed low AR expression, correlated with higher expression of CSC marker Oct4, reprogramming factor SOX2 and IMPA1 protein expression compared with ALDH$^{low/-}$ non-PCSCs (Fig. S1, G–I; and Fig. 8, A and B). IMPA1 loss significantly downregulated reprogramming factor SOX2, which is also important for maintaining AR$^{low/-}$ lineage plasticity, but upregulated AR and NKX3.1 expression in ALDH^{high} PCSCs isolated from AR-positive LNCaP cells and *TRAMP* mice (Fig. 8, A and B; and Fig. 3, D and F).

Since the IMPA1/inositol/IMPDH2 axis maintains PCSCs and IMPA1/inositol critically orchestrates CRPC, we assessed whether IMPA1/inositol is crucial for maintaining PCSCs with AR$^{low/-}$ features through activating IMPDH2 axis. To that end, we conducted systematic RNA-seq to identify the gene expression profile in CRPC 22RV1 cells with control knockdown, IMPA1 knockdown, or IMPDH2 knockdown. RNA-seq revealed that diverse reprogramming factors, epigenetic regulators, and E2F target genes were downregulated in both IMPA1 and IMPDH2 knockdown cells compared with control knockdown cells (Fig. 6 T; data available at figshare: https://figshare.com/s/cc1fbc04cda684abf0a6), suggesting the potential role of IMPA1 and IMPDH2 in epigenetic and transcriptomic regulation. However, we found the upregulation of AR target genes (TMPRSS2, FKBP5, and NDRG1) upon IMPA1 and IMPDH2 knockdown (Fig. 6 T).

In line with RNA-seq datasets, quantitative real-time PCR (qRT-PCR) revealed that reprogramming and TFs such as SOX2, LIN18A, hTET1, EZH2, and MYCN were significantly downregulated in IMPA1 and IMPDH2 knockdown cells (Fig. 8, C and D). Moreover, the mRNA levels of AR and its target genes including TMPRSS2, NDRG1, and FKBP5 were all upregulated in IMPA1 and IMPDH2 knockdown cells (Fig. 8, E and F), indicative of the occurrence of lineage switch from AR$^{low/-}$ to AR^{+} cells upon IMPA1 and IMPDH2 deficiency.

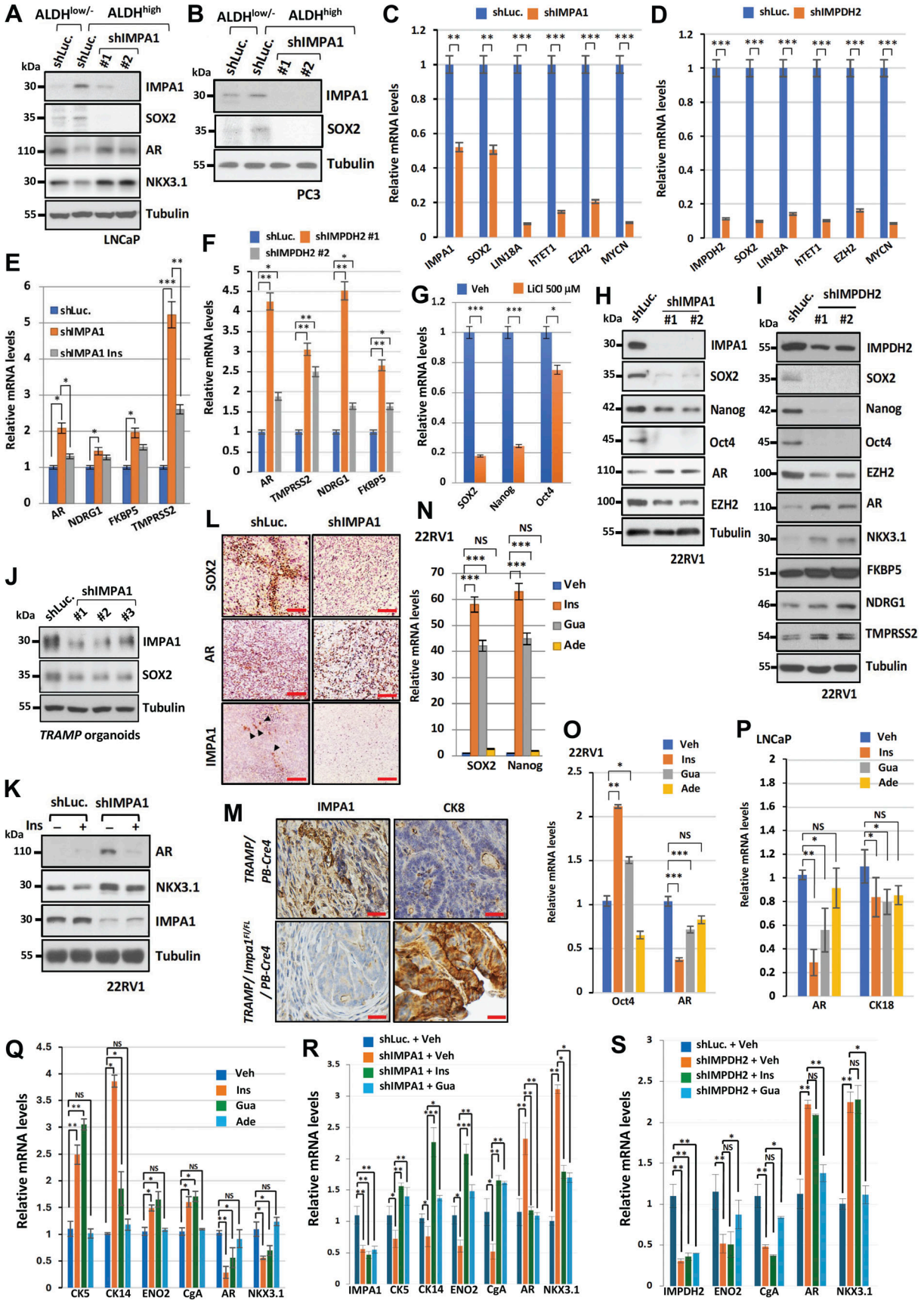

Figure 8. **IMPA1/inositol/IMPDH2 maintains PCSCs with AR$^{low/-}$ features. (A and B)** Immunoblotting of ALDH$^{low/-}$ and ALDH^{high} cells sorted from LNCaP (A) and PC3 (B) cells stably expressing shLuc or shIMPA1 (#1 and #2) with indicated antibodies. Immunoblotting data were verified in at least two independent

experiments. **(C and D)** Relative gene expression of reprogramming factors and epigenetic regulators in 22RV1 cells stably expressing shLuc, shIMPA1, or shIMPDH2 were determined by qRT-PCR analysis. Data are shown as the mean ± SEM of three independent experiments for each group. **, P < 0.01; ***, P < 0.001 by two-tailed unpaired *t* test. **(E)** Relative gene expression of AR and AR target genes in 22RV1 cells stably expressing shLuc or shIMPA1 upon 40 µM of inositol (Ins) treatment for 48 h were determined by qRT-PCR. Data are shown as the mean ± SEM of three independent experiments for each group. *, P < 0.05; **, P < 0.01; ***, P < 0.001 by two-tailed unpaired *t* test. **(F)** Relative gene expression of AR and AR target genes in 22RV1 cells stably expressing shLuc or shIMPDH2 (#1 and #2) were determined by qRT-PCR. Data are shown as the mean ± SEM of three independent experiments for each group. *, P < 0.05; **, P < 0.01 by two-tailed unpaired *t* test. **(G)** Relative gene expression of SOX2, Nanog, Oct4 and SYP in 22RV1 cells upon vehicle or 500 µM of LiCl treatment for 48 h were determined by qRT-PCR. Data are shown as the mean ± SEM of three independent experiments for each group. *, P < 0.05; **, P < 0.01; ***, P < 0.001 by two-tailed unpaired *t* test. **(H)** Immunoblotting of 22RV1 cells stably expressing shLuc or shIMPA1 (#1 and #2) with indicated antibodies. Immunoblotting data were verified in at least two independent experiments. **(I)** Immunoblotting of 22RV1 cells stably expressing shLuc or shIMPDH2 (#1 and #2) with indicated antibodies. Immunoblotting data were verified in at least two independent experiments. **(J)** Immunoblotting of tumor organoid from *TRAMP* mice expressing shLuc or shIMPA1 (#1, #2, and #3) with indicated antibodies. Immunoblotting data were verified in at least two independent experiments. **(K)** Immunoblotting of 22RV1 cells expressing shLuc or shIMPA1 upon 25 µM of inositol (Ins) treatment with indicated antibodies. Immunoblotting data were verified in at least two independent experiments. **(L)** IHC of 22RV1 xenograft tumors stably expressing shLuc or shIMPA1 with indicated antibodies. IHC data were verified in at least two independent experiments. Scale bar, 100 µm. **(M)** IHC of prostate tissue from *TRAMP/PB-Cre4* and *TRAMP/Impa1*$^{FL/FL}$*/PB-Cre4* mice at the age of 7 mo with indicated antibodies. IHC data were verified in at least two independent experiments. Scale bar, 50 µm. **(N and O)** Relative gene expression of SOX2, Nanog, Oct4, and AR genes in 22RV1 cells upon the treatment of 40 µM of inositol (Ins), 40 µM of guanosine (Gua), or 40 µM of adenosine (Ade) for 48 h were determined by qRT-PCR. The data are shown as the mean ± SEM of three independent experiments for each group. *, P < 0.05; **, P < 0.01; ***, P < 0.001; NS, non-significant by two-tailed unpaired *t* test. **(P)** Relative gene expression of luminal markers in LNCaP cells upon the treatment of 40 µM of inositol (Ins), 40 µM of guanosine (Gua), or 40 µM of adenosine (Ade) for 48 h were determined by qRT-PCR. The data were shown as the mean ± SEM of three independent experiments for each group. *, P < 0.05; **, P < 0.01; NS, non-significant by two-tailed unpaired *t* test. **(Q)** Relative gene expression of lineage markers in 22RV1 cells upon the treatment of vehicle (Veh), 40 µM of inositol (Ins), 40 µM of guanosine (Gua), or 40 µM of adenosine (Ade) for 48 h, followed by qRT-PCR. **(R)** Relative gene expression of lineage markers in 22RV1 cells stably expressing shLuc or shIMPA1 upon the treatment of vehicle (Veh), 40 µM of inositol (Ins), or 40 µM of guanosine (Gua) for 48 h, followed by qRT-PCR. **(S)** Relative gene expression of lineage markers in 22RV1 cells stably expressing shLuc or shIMPDH2 upon the treatment of vehicle (Veh), 40 µM of inositol (Ins), or 40 µM of guanosine (Gua) for 48 h, followed by qRT-PCR. All data in Q–S are shown as the mean ± SEM of three independent experiments for each group. *, P < 0.05; **, P < 0.01; ***, P < 0.001, NS, non-significant by two-tailed unpaired *t* test. Source data are available for this figure: SourceData F8.

mRNA levels of CSC markers, Nanog and Oct4, and the reprogramming factor SOX2 were all downregulated upon inactivation of IMPA1 by LiCl treatment (Fig. 8 G). Likewise, the protein expression levels of CSC markers (Oct4 and Nanog) and reprogramming factors (SOX2 and EZH2) were significantly decreased not only in IMPA1 and IMPDH2 knockdown 22RV1 cells but also in prostate tumor organoids from *TRAMP* mice and CRPC xenograft tumors of 22RV1 under IMPA1 knockdown (Fig. 8, H–L). We further confirmed that protein expression of AR and its targets including TMPRSS2, NDRG1, FKBP5, and NKX3.1, which are luminal markers, were upregulated in IMPA1 and IMPDH2 knockdown cancer cells and IMPA1 knockdown xenograft tumors (Fig. 8, H, I, K, and L).

In an in vivo genetic *TRAMP* mouse model, conditional *Impa1* knockout in prostate in *TRAMP* mice (*TRAMP/Impa1*$^{FL/FL}$*/PB-Cre4*) significantly upregulated expression of luminal epithelial cell marker CK8 as the prostate tumor in *TRAMP* mouse model (*TRAMP/PB-Cre4*) displayed low protein expression of luminal epithelial marker CK8 (Fig. 8 M). These results indicate that genetic loss of *Impa1* promotes luminal cell lineage in vivo in *TRAMP* mouse model.

Remarkably, the restoration of inositol in IMPA1 knockdown 22RV1 cells reversed the expression of AR and its targets (Fig. 8, E and K). Additionally, administration of either inositol or guanosine, but not adenosine, induced the expression of CSC markers (Nanog and Oct4) and reprogramming factor SOX2 (Fig. 8, N and O). Collectively, these results indicate the acquisition of AR^{+} luminal cell lineage, but the loss of PCSC marker expression upon loss of inositol or guanosine.

We then defined the role of IMPA1/inositol/IMPDH2 axis in maintaining AR$^{low/-}$ lineages. Administration of either inositol or guanosine, but not adenosine, induced the expression of basal cell markers (CK5 and CK14) and neuroendocrine markers (ENO2 and CgA) but decreased luminal cell markers (AR, NKX3.1, and CK18) (Fig. 8, O–Q). Of note, IMPA1 knockdown or IMPDH2 knockdown decreased the expression of basal cell markers (CK5 and CK14) and neuroendocrine markers (ENO2 and CgA) but upregulated the expression of luminal markers (AR and NKX3.1) in CRPC 22RV1 cells (Fig. 8, R and S). Restoration of either inositol or guanosine in IMPA1 knockdown cells reversed the downregulation of basal cell markers (CK5 and CK14) and neuroendocrine markers (ENO2 and CgA) and the upregulation of luminal cell markers (AR and NKX3.1) (Fig. 8 R). However, restoration of guanosine, but not inositol, in IMPDH2 knockdown cells reversed the downregulation of neuroendocrine markers (ENO2 and CgA) and the upregulation of luminal cell markers (AR and NKX3.1) (Fig. 8 S). Collectively, these results suggest that IMPA1/inositol axis is a master metabolic pathway critical for maintaining AR$^{low/-}$ cell lineage partly via activating IMPDH2/guanosine pathway.

Of note, we examined IMPA1 and IMPDH2 expression in our in-house metastatic prostate cancer with high AR expression (20 cases) in comparison with metastatic prostate cancer with low or negative AR expression (20 cases). Consistently, IMPA1 and IMPDH2 expression are significantly upregulated in AR$^{low/-}$ metastatic prostate cancer compared with AR^{+} metastatic prostate cancer (Fig. S4, E–G). Therefore, the IMPA1/inositol/IMPDH2 axis displays the clinical significance associated with low/negative AR expression that emerges in the metastatic process.

To further investigate the clinical correlation between AR and IMPA1 in CRPC patients, we collected clinical specimens from our in-house CRPC patient samples with high AR expression (AR^{+} CRPC) and low/negative AR expression (AR$^{low/-}$ CRPC) and examined the IMPA1 expression. IHC analysis

revealed that IMPA1 is upregulated in $AR^{low/-}$ CRPC patients compared with AR^{+} CRPC patients (Fig. S4, H and I). To measure inositol levels from clinical samples of prostate cancer patients, we retrieved frozen clinical samples for quantification of inositol levels by using LC-MS/MS. We found that inositol is upregulated in the clinical samples with CRPC compared with those without CRPC (Fig. S4 J). Collectively, IMPA1 appears to be upregulated in $AR^{low/-}$ CRPC compared with AR^{+} CRPC.

Next, we determined whether IMPDH2, as a key downstream of IMPA1/inositol axis in maintaining PCSCs, also maintains CRPC progression, similar to IMPA1/inositol. The anchorage-independent cell transformation was also significantly reduced in IMPDH2 knockdown cells (Fig. S4, K–N). CRPC tumor growth in vivo was markedly impaired upon IMPDH2 deficiency (Fig. S4 O). Of note, the restoration of guanosine, but not inositol and adenosine, partially rescued the defect in cell transformation and CRPC tumor formation in vivo upon IMPDH2 knockdown (Fig. S4, M and O). Importantly, IHC staining from adjacent normal (80 cases) and prostate cancer (80 cases) in our in-house prostate cancer samples also revealed that high IMPDH2 protein expression was detected in human prostate cancer compared with normal prostate and predicted poor survival outcome (Fig. S4, P–R), similar to high IMPA1 protein expression and its association with poor prognosis in these clinical samples (Fig. 5, I–K). Collectively, IMPDH2 shows clinical significance in prostate cancer progression and serves as a sensor of IMPA1-derived inositol to maintain tumorigenicity of CRPC.

The role of EZH2 in regulating PCSCs with $AR^{low/-}$ features by IMPA1/inositol/IMPDH2 axis

PCSCs have been postulated to arise from diseased stem cells or differentiated non-stem bulk tumor cells through epigenetic alterations (Davies et al., 2018). Since SOX2, EZH2, and MYCN all are involved in maintaining the feature of stem-like cells (Varlakhanova et al., 2010; Yu et al., 2017; Zhang and Cui, 2014), which were also downregulated upon IMPA1 knockdown or IMPDH2 knockdown (Fig. 8, C and D; and Fig. S5, A and B), we asked the question whether restoration any of these factors rescued the defect of PCSCs and reversed the expression of luminal epithelial cell markers in IMPA1 and IMPDH2 knockdown cells. Notably, restoration of EZH2, but not SOX2 and MYCN, profoundly rescued the defect of cancer sphere formation and reversed the increased expression of AR activity, reflected by the reduced expression of AR target gene, NKX3.1, and AR expression, upon IMPA1 and IMPDH2 knockdown (Fig. S5, A–D). Thus, restoration of EZH2 partly rescues the defect in PCSCs upon IMPA1 and IMPDH2 knockdown.

Targeting IMPA1/inositol/IMPDH2 axis is an effective strategy for combating CRPC and ABT resistance using tumor organoids, PDX model, and CRPC tumor models

To investigate the role of the IMPA1/inositol/IMPDH2 axis in driving CRPC and ABT resistance, we established the LNCaP enzalutamide-resistant (EnzaR) cells by long-term treatment of enzalutamide for 6 mo (Fig. S5 E). IMPA1 expression and inositol level were also significantly elevated in EnzaR cells (Fig. S5, F and G), correlated with upregulated expression of reprogramming factor and CSC markers, SOX2 and Oct4, and reduced luminal cell marker AR expression compared with enzalutamide-sensitive LNCaP (EnzaS) cells (Fig. S5 F), indicating the lineage switch from AR^{+} epithelial lineage to $AR^{low/-}$ lineage during ABT resistance. Notably, knockout of IMPA1 using CRISPR/Cas9 in EnzaR cells impaired the expression of SOX2 and rescued AR expression (Fig. S5 H), suggesting that the crucial role of IMPA1 in maintaining $AR^{low/-}$ lineage in EnzaR CRPC cells.

Remarkably, administration of either inositol or guanosine, but not adenosine, or IMPA1 overexpression accompanied with downregulation of AR caused the enzalutamide resistance in androgen-sensitive LNCaP cells, as determined by colony formation and cell survival assay (Fig. S5, I–P). To demonstrate whether the IMPA1/inositol/IMPDH2 axis confers ABT resistance, we performed a cell survival assay, colony formation assay, and cancer sphere assay upon IMPA1 or IMPDH2 knockdown in CRPC 22RV1 cells. Genetic IMPA1 or IMPDH2 knockdown by two or three distinct lentiviral shRNAs in CRPC 22RV1 cells and CRPC 22RV1 cancer spheres resensitized the inhibition of cell survival, colony formation, and cancer sphere formation upon enzalutamide treatment (Fig. 9, A–K). IMPA1 knockdown in CRPC 22RV1 cells reduced in vivo CRPC tumor growth and resensitized CRPC tumor to enzalutamide treatment (Fig. 9 P). Of note, restoration of IMPA1 expression level in IMPA1 knockout cells, but not its enzymatic dead mutant, IMPA1-D220A, abrogated the sensitivity of CRPC 22RV1 cells and CRPC 22RV1 cancer spheres to enzalutamide upon IMPA1 knockdown (Fig. 9, L–O), indicating that phosphatase activity of IMPA1 for inositol production is essential for conferring enzalutamide resistance.

To assess whether IMPA1 impairment directly impacts CRPC progression in vivo, we also performed surgical castration in NOD/SCID male mice, followed by xenograft assay. Administration of enzalutamide in control knockdown tumors did not inhibit castration-resistant tumor growth (Fig. 9 Q). Remarkably, IMPA1 knockdown alone or in combination with enzalutamide dramatically impaired prostate tumorigenicity in castrated male mice (Fig. 9 Q).

While restoration of inositol or guanosine compromised the sensitivity to enzalutamide in IMPA1 knockdown cells (Fig. 9 R), restoration of guanosine, but not inositol, impaired the sensitivity to enzalutamide upon IMPDH2 knockdown (Fig. 9 S). Collectively, these results suggest that IMPA1/inositol drives ABT resistance through IMPDH2.

Given IMPA1/inositol/IMPDH2 axis critically maintains PCSC properties for CRPC progression and ABT resistance, we rationalized that inhibiting the IMPA1/inositol/IMPDH2 axis may be a potential strategy for targeting CRPC and overcoming ABT resistance. To test this notion, we used pharmacological approaches to verify the role of targeting the IMPA1/inositol/IMPDH2 axis in viability, organoid growth, and tumor growth of CRPC in xenografts and PDX models. Strikingly, pharmacological inhibition of IMPA1 by LiCl or IMPDH2 inactivation by its inhibitor, MPA, or mizoribine (MZB) in two CRPC cell lines (22RV1 and TRAMP-C2) and CRPC PDX in conjunction with enzalutamide markedly reduced colony formation and cell

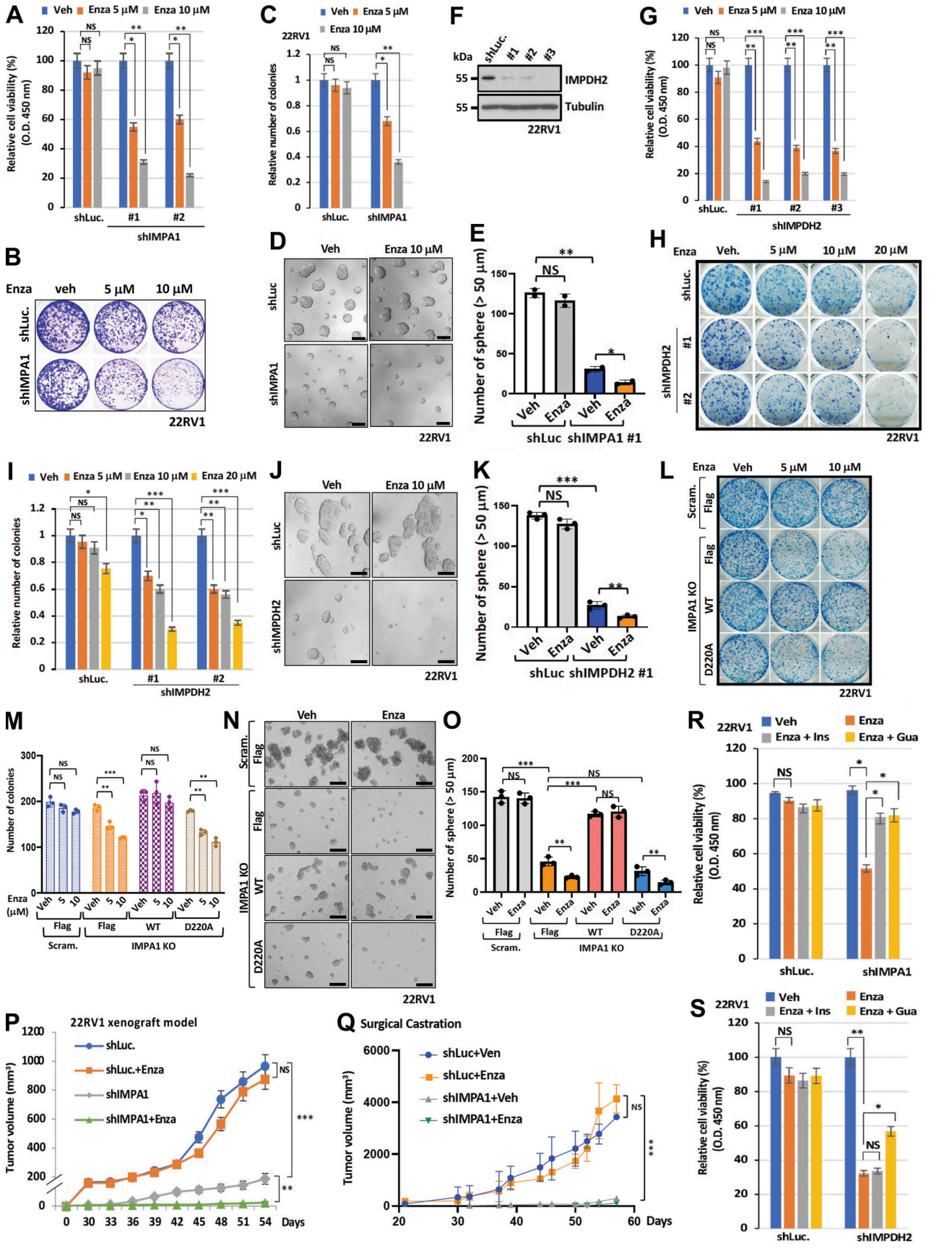

Figure 9. **IMPA1/inositol/IMPDH2 confers enzalutamide resistance. (A and G)** Relative cell viability of 22RV1 cells stably expressing shLuc, shIMPA1 (#1 and #2) (A), or shIMPDH2 (#1, #2 and #3) (G) upon vehicle (Veh), 5, or 10 μM of enzalutamide (Enza) treatment for 48 h were determined by CCK-8. The data

are shown as the mean ± SEM of three independent experiments for each group. *, P < 0.05; **, P < 0.01; ***, P < 0.001; non-significant by two-tailed unpaired *t* test. **(B)** Colony formation assay of 22RV1 cells stably expressing shLuc or shIMPA1 upon vehicle (Veh), 5 or 10 μM of enzalutamide (Enza) treatment every 2 days for 14 days. **(C)** Quantification of colony number from B by ImageJ was shown. The data were shown as the mean ± SEM of three independent experiments for each group. *, P < 0.05; **, P < 0.01; non-significant by two-tailed unpaired *t* test. **(D)** Cancer sphere formation in 22RV1 cells stably expressing shLuc and shIMPA1 #1 upon vehicle (Veh) and 10 μM of enzalutamide (Enza) treatment. Scale bar, 100 μm. **(E and K)** Quantification of the number of cancer sphere formations with over 50 μm of diameter from D and J to E and K. The data are shown as the mean ± SEM of three independent experiments for each group. **, P < 0.01; ***, P < 0.001; NS, non-significant by two-tailed unpaired *t* test. **(F)** Immunoblotting of 22RV1 cells stably expressing IMPDH2 (#1, #2, and #3) with indicated antibodies. **(H)** Colony formation assay of 22RV1 cells stably expressing shLuc or shIMPDH2 (#1 and #2) upon vehicle (Veh), 5, 10, or 20 μM of enzalutamide (Enza) treatment every 2 days for 14 days. **(I)** Quantification of colony number from H by ImageJ was shown. **(J)** Cancer sphere formation in 22RV1 cells stably expressing shLuc and shIMPDH2 #1 upon vehicle (Veh) and 10 μM of enzalutamide (Enza) treatment. Scale bar, 100 μm. **(L)** Colony formation assay of 22RV1 scramble (Scram.) or IMPA1 knockout (KO) cells by CRISPR/Cas9 upon Flag vector, Flag-IMPA1 (WT) and Flag-IMPA1 D220A (D220A) overexpression in response to vehicle (Veh), 5 or 10 μM of enzalutamide (Enza) treatment every 2 days for 14 days. **(M)** Quantification of colony number from L by ImageJ was shown. The data were shown as the mean ± SEM of three independent experiments for each group. **, P < 0.01; ***, P < 0.001; non-significant by two-tailed unpaired *t* test. **(N)** Cancer sphere formation in 22RV1 cells upon Scramble (Scram.) with Flag, IMPA1 knockout (KO) with Flag, Flag-IMPA1^{WT} (WT), and Flag-IMPA1^{D220A} (D220A) in response to the treatment of vehicle (Veh) and 10 μM of enzalutamide (Enza) treatment. Scale bar, 100 μm. **(O)** Quantification of the number of cancer sphere formations with over 50 μm of diameter from N–O. The data are shown as the mean ± SEM of three independent experiments for each group. **, P < 0.01; ***, P < 0.001; NS, non-significant by two-tailed unpaired *t* test. **(P)** Male nude mice subcutaneously injected with 22RV1 cells stably expressing shLuc or shIMPA1 were intraperitoneally injected with vehicle (Veh) or 5 mg/kg of enzalutamide (Enza) every 2 days for 40 days, and tumor volume was measured with indicated days. Five mice were included in each experimental group. **(Q)** Surgically castrated NOD/SCID mice subcutaneously injected with 22RV1 cells upon shLuc and shIMPA1 were intraperitoneally injected with vehicle or 5 mg/kg of enzalutamide (Enza) three times a week for 6 wk and tumor volume was measured with indicated days. Five mice were included in each experimental group. **(R)** Relative cell viability of 22RV1 cells stably expressing shLuc or shIMPA1 upon vehicle (Veh), 5 μM of enzalutamide (Enza), 80 μM of inositol (Ins), or 80 μM of guanosine (Gua) for 72 h treatment was determined by CCK-8. The data are shown as the mean ± SEM of three independent experiments for each group. *, P < 0.05; NS, non-significant by two-tailed unpaired *t* test. **(S)** Relative cell viability of 22RV1 cells stably expressing shLuc or shIMPDH2 upon vehicle (Veh), 5 μM of enzalutamide (Enza), 80 μM of inositol (Ins), or 80 μM of guanosine (Gua) for 72 h treatment was determined by Cell Counting Kit-8 (CCK-8). The data are shown as the mean ± SEM of three independent experiments for each group. *, P < 0.05; **, P < 0.01; NS, non-significant by two-tailed unpaired *t* test. Source data are available for this figure: SourceData F9.

survival of CRPC cells (Fig. 10, A–F) and tumor growth of CRPC 22RV1 and PDX in vivo (Fig. 10, G and H).

To assess whether inhibition of IMPA1 or IMPDH2 alone or in combination with enzalutamide treatment can be effective in targeting CRPC progression, we also performed surgical castration in NOD/SCID male mice, followed by xenograft assay. While enzalutamide failed to show efficacy in reducing castration-resistant xenograft tumor volume, pharmacological inhibition of IMPA1 by LiCl or IMPDH2 inactivation by MZB reduced castration-resistant tumor growth and tumor weight (Fig. 10, I and J). Administration of LiCl or MZB in combination with enzalutamide further attenuated castration-resistant tumor growth and tumor weight (Fig. 10, I and J). However, the treatment of various inhibitors did not reduce the body weight of mice and affect the cell viability of normal prostate epithelium cells, PNT1A (Fig. 10 K and Fig. S5 Q), suggesting the low toxicity of LiCl or MZB alone or in combination with enzalutamide treatment in vivo.

To demonstrate the role of IMPA1/inositol/IMPDH2 in the CRPC *TRAMP* mouse model, we performed surgical castration in *TRAMP* mice at the age of 8 wk. *TRAMP* mice at the age of 9 wk were intraperitoneally administrated with vehicle, enzalutamide, IMPA1 inhibitor (LiCl), IMPDH2 inhibitor (MZB), or in combination with enzalutamide. H&E staining revealed that poorly differentiated carcinoma significantly occurred in castrated *TRAMP* mice (80%) administrated with vehicle or enzalutamide at the age of 6 mo (Fig. 10, L and M); however, administration of LiCl or MZB slightly reduced poorly differentiated tumors at the age-matched castrated *TRAMP* mice (60%) (Fig. 10, L and M). Notably, castrated *TRAMP* mice administrated with enzalutamide in combination with MZB or LiCl significantly reduced poorly differentiated carcinoma but maintained moderately or well-differentiated carcinoma (20–40%) (Fig. 10, L and M). Collectively, pharmacological inhibition of IMPA1 by LiCl or IMPDH2 inactivation by MZB or in combination with enzalutamide ameliorates poorly differentiated carcinoma in castrated *TRAMP* mouse model.

Using two CRPC tumor organoid models from *TRAMP* mice and CRPC PDX tumor, which display ABT resistance (Fig. S5, R and S), we demonstrated that pharmacological inhibition of IMPA1 by LiCl or IMPDH2 inactivation by MZB or MPA inhibited tumor organoid growth, and inhibition of IMPA1 or IMPDH2 in combination with enzalutamide treatment further reduced tumor organoid growth (Fig. 10, N–Q). Collectively, our data provide proof of principle evidence that genetically and pharmacologically targeting the IMPA1/inositol/IMPDH2 axis serves as a promising strategy for targeting CRPC and overcoming ABT resistance.

Discussion

Unraveling novel paradigms allowing for developing therapeutic strategies for CRPC represents an ungently medical need, as there is thus far no effective treatment regime for CRPC. In this study, we identified the IMPA1/inositol axis is amplified in CRPC and its overexpression predicts poor survival outcome as a key mechanism to drive PCSC maintenance and lineage plasticity leading to CRPC progression and ABT resistance partly by activating IMPDH2/guanosine (Fig. S5 T). We validated the essential role of *Impa1* in maintaining PCSCs and CRPC progression using in vivo limiting dilution (Fig. 2, A–E) and genetic *TRAMP* mouse model by generating *TRAMP/Impa1$^{FL/FL}$/PB-Cre4* and *TRAMP* mice (Fig. 5, B–D). Organoids are derived from isolated organ progenitors that can differentiate into an organ-like tissue

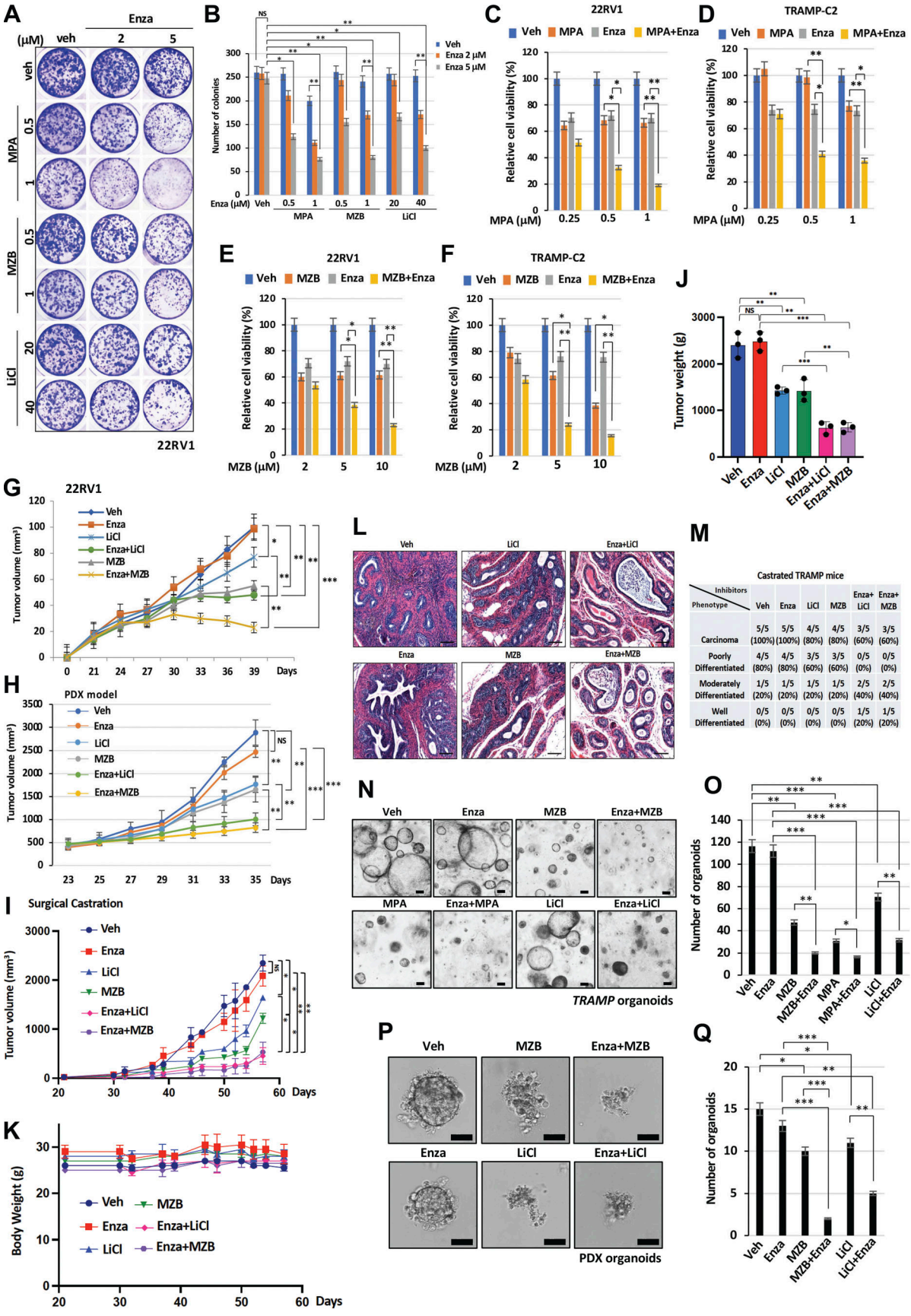

Figure 10. **Pharmacological inhibition of IMPA1 or IMPDH2 in combination with enzalutamide efficiently eradicates CRPC progression. (A)** Colony formation assay of 22RV1 cells upon vehicle (Veh), 2 or 5 μM of enzalutamide (Enza), 0.5 or 1 μM of MPA, 0.5 or 1 μM of MZB, and 20 or 40 μM of LiCl treatment

for 14 days. **(B)** Quantification of the number of colonies from 22RV1 by ImageJ is shown in A. **(C)** MTT assay of 22RV1 cells upon vehicle (Veh), 10 μM of enzalutamide (Enza); 250 nM, 500 nM, or 1 μM of MPA treatment for 24 h. **(D)** MTT assay of TRAMP-C2 cells upon vehicle (Veh), 10 μM of enzalutamide (Enza); 250 nM, 500 nM, or 1 μM of MPA treatment for 24 h. **(E)** MTT assay of 22RV1 cells upon vehicle (Veh), 10 μM of enzalutamide (Enza); 2, 5, or 10 μM of MZB treatment for 24 h. **(F)** MTT assay of TRAMP-C2 cells upon vehicle (Veh), 10 μM of enzalutamide (Enza); 2, 5, or 10 μM of MZB treatment for 24 h. All statistical data are shown as the mean ± SEM of three independent experiments for each group. *, P < 0.05; **, P < 0.01; ***, P < 0.001; NS, non-significant by two-tailed unpaired *t* test. **(G)** Male nude mice subcutaneously injected with 22RV1 cells were intraperitoneally injected with vehicle (Veh), 5 mg/kg of enzalutamide (Enza) daily for 21 days, 200 mg/kg of MZB daily for 7 days; no treatment for 4 days; 100 mg/kg of MZB daily for 10 days or 200 mg/kg of LiCl daily for 21 days, and tumor volume was measured with indicated days. Five mice were included in each experimental group. **(H)** Male NSG mice subcutaneously injected with PDX prostate tumor were intraperitoneally injected with vehicle (Veh), 5 mg/kg of enzalutamide (Enza) daily for 21 days, 200 mg/kg of MZB daily for 7 days; no treatment for 4 days; 100 mg/kg of MZB daily for 10 days or 200 mg/kg of LiCl daily for 21 days, and tumor volume was measured with indicated days. Five mice were included in each experimental group. **(I)** Surgically castrated NOD/SCID mice subcutaneously injected with 22RV1 cells were intraperitoneally injected with vehicle or 5 mg/kg of enzalutamide (Enza), 200 mg/kg of LiCl, 100 mg/kg of MZB, 5 mg/kg of enzalutamide (Enza) in combination with 200 mg/kg of LiCl and 5 mg/kg of enzalutamide (Enza) in combination with 100 mg/kg of MZB three times a week for 6 wk and tumor volume was measured with indicated days. Five mice were included in each experimental group. **(J)** Tumor weight from I was measured on day 57. At least three xenograft tumors in each group were quantified. **, P < 0.01; ***, P < 0.001 by two-tailed unpaired *t* test. **(K)** Body weight from I was measured as indicated days. Five mice were included in each experimental group. **(L)** H&E staining of prostate tissues from surgically castrated TRAMP mice at the age of 6 mo administrated with 5 mg/kg of enzalutamide (Enza), 100 mg/kg of MZB, 200 mg/kg of LiCl, 5 mg/kg of Enza combination with 100 mg/kg of MZB and 5 mg/kg of Enza combination with 200 mg/kg of LiCl three times a week for 18 wk. Five mice were included in each experimental group. Scale bar, 100 μm. **(M)** Histological analysis for the phenotype of carcinoma in surgical castrated TRAMP mice upon the administration of indicated inhibitors. Each group includes 5 mice. **(N)** Tumor organoids from *TRAMP* mice upon Veh, 5 μM of Enza, 1 μM of MPA, 1 μM of MZB, or 500 μM of LiCl treatment for 4 days. Scale bar, 100 μm. **(O)** Quantification of organoid number from N by Image J was shown as the mean ± SEM of three independent experiments for each group. *, P < 0.05; **, P < 0.01; ***, P < 0.001 by two-tailed unpaired *t* test. **(P)** Tumor organoids from PDX tumors with Veh, 5 μM of Enza, 1 μM of MZB, or 500 μM of LiCl treatment for 4 days. Scale bar, 50 μm. **(Q)** Quantification of organoid number from P by ImageJ was shown as the mean ± SEM of three independent experiments for each group. *, P < 0.05; **, P < 0.01; ***, P < 0.001 by two-tailed unpaired *t* test.

consisting of multiple cell types that self-organize to form structures similar to the organ in vivo (Kim et al., 2020). This technology has been built for the foundation of stem cell research (Kim et al., 2020; Tang et al., 2022). Using CRPC tumor organoid models from male *TRAMP* mice and the PDX tumor, genetically and pharmacologically targeting the IMPA1/inositol/IMPDH2 axis markedly impairs the maintenance of $AR^{low/-}$ PCSCs, thus repressing CRPC and overcoming ABT resistance. Our study not only identifies the role of IMPA1/inositol/IMPDH2 axis in driving PCSCs and lineage plasticity for CRPC progression but also suggests that targeting this newly defined metabolic axis is an effective strategy for targeting CRPC and ABT resistance in combination with second-generation AR inhibitors.

IMPDH2 is a rate-limiting enzyme generating purine/guanine nucleotides for DNA synthesis. However, the regulatory mechanisms by which its enzymatic activity is regulated and its role in PCSCs and CRPC progression have been elusive. We show that IMPDH2 serves as a key metabolic enzyme maintaining PCSCs and CRPC progression partly through guanylate purine production. Of note, we demonstrate unprecedentedly that inositol acts as a key metabolite directly binding to and activating IMPDH2 activity by maintaining dimerization/oligomerization of IMPDH2, independently of its canonical role in participating in PI and phosphoinositides production. Thus, IMPDH2 is a critical sensor of inositol, whose activity is induced by inositol through its direct binding to inositol. Our study places the IMPA1/inositol axis as a pivotal upstream mechanism for IMPDH2 activation leading to purine/guanylate production, thereby maintaining PCSCs with $AR^{low/-}$ features for CRPC progression and ABT resistance. It is important to note that the IMPA1/inositol/IMPDH2 axis may also serve as a suppressive signal to limit the expression of AR and its targets for luminal cell lineage leading to maintaining $AR^{low/-}$ lineage. As such, targeting the IMPA1/inositol/IMPDH2 axis eradicates PCSCs for CRPC and switches $AR^{low/-}$ lineage cells to luminal AR^{+} cells, hence providing the molecular basis of how targeting this axis overcomes ABT resistance in CRPC models (Fig. S5 T).

SOX2, EZH2, and MYCN have been shown to facilitate $AR^{low/-}$ lineage plasticity and CRPC progression through epigenetic and transcriptional reprogramming (Dardenne et al., 2016; Ferone et al., 2016; Ku et al., 2017; Mu et al., 2017; Murai et al., 2015; Sarkar and Hochedlinger, 2013). Although pharmacologically targeting SOX2 and EZH2 appears to be an ideal strategy for eradicating PCSCs and thus CRPC, there is either no agent currently available for targeting SOX2 and MYCN or the lack of a well-tolerable EZH2 inhibitor. The newly developed inhibitor for targeting SOX2 is still in the preclinical stage and its potential clinical application is also unknown (Hüser et al., 2018). EZH2 inhibitors have exhibited high toxicity due to the diverse roles of the PRC2 complex consisting of EZH2 in cellular processes including normal cell development, differentiation, and reproduction (Yamagishi and Uchimaru, 2017). MYCN also has been deemed as "undruggable" so that the methods indirectly targeting MYCN have been investigated (Wolpaw et al., 2021). Given that pharmacological targeting transcriptional factors (TFs) reveal the difficulty of the effectiveness and safety of CRPC, targeting the IMPA1/inositol/IMPDH2 axis, which functions as a cancer metabolic vulnerability identified in this study, represents a promising strategy for CRPC and ABT resistance.

Prostate-specific antigen (PSA) is a widely used biomarker for prostate cancer diagnosis and monitoring ABT responses (Pérez-Ibave et al., 2018). However, it cannot be used for prostate cancer diagnosis and monitoring treatment response in those CRPC tumors exemplified by $AR^{low/-}$ prostate cancer cells, which typically exhibit low or non-rising PSA (Davies et al., 2018). In light of lacking potential serum biomarkers for CRPC thus far, the identification of a novel biomarker for specifically

monitoring CRPC and treatment response is therefore imperative. Our findings that IMPA1 is enriched in advanced prostate cancer and that inositol level is elevated in the serum of prostate cancer patients suggest that inositol may serve as a potential serum biomarker for CRPC diagnosis and for monitoring the treatment response for CRPC.

In summary, we identified a novel metabolic axis namely the IMPA1/inositol/IMPDH2 axis as a key mechanism for maintaining $AR^{low/-}$ PCSC properties leading to CRPC progression and ABT resistance. Our findings highlight the novel crosstalk between inositol and purine metabolism in that IMPDH2 serves as an inositol sensor that elicits guanylate purine metabolism to maintain PCSCs and lineage plasticity for CRPC progression and ABT resistance. Our study provides proof of principle evidence that targeting the IMPA1/inositol/IMPDH2 axis through either IMPA1 or IMPDH2 inhibition represents a promising strategy for targeting CRPC and overcoming ABT resistance.

Materials and methods

Mice

TRAMP mice on C57BL/6J background were previously described (Chen et al., 2005; Lin et al., 2010; Ruan et al., 2017). Male *TRAMP* mouse (C57BL/6J) purchased from the Jackson Laboratory was crossed with WT mice to generate cohorts of male *TRAMP* mice for tumor organoids study. Female *Impa1*$^{flox/flox}$ mice were crossed with male *PB-Cre4* transgenic mice to generate cohorts of male *Impa1*$^{flox/flox}$*/PB-Cre4* mice. Female *TRAMP* mice were crossed with male *Impa1*$^{flox/flox}$*/PB-Cre4* mice to generate cohorts of male *TRAMP/Impa1*$^{flox/flox}$*/PB-Cre4* mice for histopathological and survival study. NOD-*scid* IL2Rg^{null} (NSG) mouse (No: 005557) purchased from the Jackson Laboratory was used for PDX study. All animal procedures were approved by the Institutional Animal Care and Use Committee in Wake Forest University School of Medicine and Duke University School of Medicine.

Cell culture

DU145, PC3, 22RV1, and LNCaP cells were cultured in RPMI 1640 supplied with 10% FBS. TRAMP-C2 cells were cultured in DMEM supplied with 5% FBS, 5% Nu-serum IV, 5 µg/ml insulin, and 10 nM dihydrotestosterone (DHT). EnzaR LNCaP cells were cultured in RPMI 1640 supplied with 10% FBS and 100 µM of enzalutamide. Prostate cancer PDX cells isolated from PDX tumors (Model ID: J000077451; The Jackson Laboratory) were cultured in DMEM supplied with 10% FBS.

3D prostate organoid culture

TRAMP mice at 6 mo of age or CRPC (advanced prostate adenocarcinoma/metastasis of prostate adenocarcinoma) PDX model (Model ID: J000077451), which were purchased from the Jackson Laboratory, were dissected for prostate tissue including AP, VP, and DLP, and prostate tumor were isolated and minced into small pieces about 1 mm^3, followed by digesting in 5 mg/ml collagenase type II (17101-015; Life Technologies) with 10 µM Y-27632 dihydrochloride (M1817; Abmole Bioscience) at 37°C for 1 h and then pipetting up and down with fired-polished glass pipettes. After washing with adDMEM/F12 (12634-034; Life Technologies) containing 10 mM HEPES (35050-068; Life Technologies) and 2 mM GlutaMAX (15630-056; Life Technologies), the tissue pellet was digested in TrypLE Express (12605-010; Life Technologies) 10 µM Y-27632 dihydrochloride at 37°C for 15 min, followed by washing, resuspending cells in the Matrigel, and plating on the dishes. The culture medium components were prepared for mouse prostate tumor organoids including 1× B27, 1.25 mM of N-acetylcystein, 50 ng/ml of EGF, 100 ng/ml of Noggin, R-spondin 1 (10% conditional medium from 293T-HA-RspoI-Fc cell line), 200 nM of A83-01, 1 nM of DHT, and 10 µM of Y-27632 dihydrochloride, and for human prostate cancer, PDX organoids including 1× B27, 1.25 mM of N-acetylcystein, 50 ng/ml of EGF, 100 ng/ml of Noggin, R-spondin 1 (10% conditional medium from 293T-HA-RspoI-Fc cell line), 200 nM of A83-01, 10 ng/ml of FGF10, 5 ng/ml of FGF2, 1 µM of Prostaglandin E2, 10 mM of Nicotinamide, 10 µM of SB202190, 1 nM of DHT, and 10 µM of Y-27632 dihydrochloride. From 7 days after initial plating, tumor organoids were treated with 5 µM of enzalutamide, 1 µM of MZB, 1 µM of MPA, or 500 µM of LiCl for 4–6 days. To quantify the number of organoids, at least five images of phase contrast were randomly captured, and each experimental group was conducted with three mice in the statistic, followed by using ImageJ software being processed and subjected to particle analysis for each organoid.

Generation of conditional *Impa1*$^{flox/flox}$ mice

C57BL/6 mouse model with loxP sites at exon 3 of mouse *Impa1* locus was generated by Cyagen Biosciences using CRISPR/Cas9-mediated genome engineering. The gRNA oligos to mouse *Impa1* gene were designed by the CRISPR website (http://crispor.gi.ucsc.edu) Two targeting sequences at *Impa1* locus were gRNA1: 5′-ATGGGCATGGCGCTTCTAGCTGG-3′ and gRNA: 5′-GGTGGG ATAGCCTACTCGTGAGG-3′. The donor vector containing loxP sites and Cas9 mRNA were co-injected into fertilized mouse eggs to generate targeted conditional knockout offspring. The mice with the target region of mouse *Impa1* were identified by PCR followed by sequence analysis.

Knockout cell generation using CRISPR

Knockout cells were generated using a double Cas9 nickase strategy as described previously (Ran et al., 2013b). Two pairs of gRNA targeting exon 3 and 4 respectively were designed for the IMPA1 gene using the online design tool at http://www.benchling.com/crispr. Each gRNA duplex was cloned into the PX462 vector encoding SpCas9n-2A-puro (#48141; Addgene). The lentivirus of two pairs of gRNAs was produced and used to infect cells, which were selected by puromycin (2 µg/ml), and the single colony was picked. Individual clones with IMPA1 knockout were verified by immunoblotting.

Non targeting scramble gRNA sequence:

guide A: 5′-CGAGGCTTAACGCCAGATTC-3′; guide B: 5′-GAA CTCGTTAGGCCGTGAAG-3′.

IMPA1 gRNA sequence:

guide A: 5′-AATAGGGTCAATGATCCATG-3′; guide B: 5′-CCT TTTGTAGCTGTTTCAAT-3′.

Reagents and antibodies

The antibodies were used as follows: IMPA1 (sc-374234; Santa Cruz), Nanog (sc-134218; Santa Cruz), SOX2 (sc-365823; Santa Cruz; #3579; Cell Signaling), Flag (F1804; Sigma-Aldrich), CDIPT (sc-514255; Santa Cruz), Actin (A5441; Sigma-Aldrich), GAPDH (G8795; Sigma-Aldrich), Tubulin (T8203; Sigma-Aldrich), PI4K2α (sc-390026; Santa Cruz), PLCβ1 (sc-5291; Santa Cruz), INPP1 (sc-393584; Santa Cruz), IMPDH2 (ab131158; Abcam), Oct4 (AB3209; Millipore), AR (sc-7305; Santa Cruz; sc-816; Santa Cruz), CK8 (sc-8020; Santa Cruz), EZH2 (07-689; Millipore), NKX3.1 (sc-393190; Santa Cruz), FKBP5 (sc-271547; Santa Cruz), NDRG1 (sc-398291; Santa Cruz), TMPRSS2 (sc-515727; Santa Cruz), and ALDH1A1 (sc-374076; Santa Cruz). The following secondary antibodies were used: HRP-coupled antibodies to mouse (sc-2055; Santa Cruz) and rabbit (31480; Thermo Fisher), Alexa Fluor 488 anti-mouse IgG (A-21202; Thermo Fisher), and Alexa Fluor 555 anti-rabbit IgG (A-27039; Thermo Fisher). The reagents were used as follows: LiCl (5910) was obtained from Millipore; Myo-inositol (I7508), L-α-phosphatidylinositol (P6636), guanosine (G6752), adenosine (A9251), and MPA (M5255) from Sigma-Aldrich; BIO (S7198), SB216763 (S1075), MZB (S1384), and enzalutamide (S1250) from https://Selleckchem.com; phosphatidylinositol 4-phosphate (P-4016), phosphatidylinositol 4,5-phosphate (P-4516), phosphatidylinositol 3,4,5-triphosphate (P-3924), and inositol 1,4-bisphosphate (Q-0014) from Echelon; D-myo-inositol-1-phosphate (No. 10007777) from Cayman; and myo-inositol 1,4,5-trisphosphate hexapotassium salt (1482) from Tocris.

The synthesis of biotin-labeled inositol

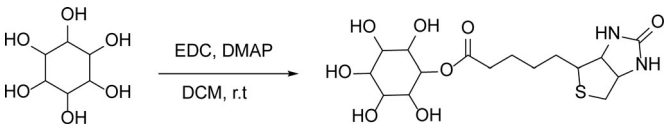

Inositol (180 mg, 1.0 mmol), 1-ethyl-3-(3-dimethylaminopropyl) carbodiimide hydrochloride (EDC) (384 mg, 2.0 mmol), and 4-dimethylaminopyridine (DMAP) (11 mg, 0.01 mmol) in dry dichloromethane (DCM) (10 ml) were mixed and stirred in the solution at room temperature, followed by adding dropwise biotin (244 mg, 1.0 mmol) in 10 ml DCM for 5 min and stirring at room temperature overnight. 20% ethyl acetate/hexanes was used for removing solvent and precipitating the product. 210 mg of wax solid was obtained and the yield was 52%. $C_{16}H_{27}N_2O_8S$ $[M+H]^+$, 407, was calculated by LC/MS.

Tumor sphere culture, immunoblotting, biotin pull-down assay, immunofluorescence, and IHC

For in vitro tumor sphere culture, 3,000 cells were counted and seeded in the low attachment 6-well plate (CORNING) with the spheroid culture medium (20 ng/ml of EGF, 20 ng/ml of FGF, 1× B27, 5 μg/ml of insulin, and 0.5 μg/ml of hydrocortisone in HyClone DMEM/F12 1:1 medium). To quantify the cancer sphere, at least five images of phase contrast were randomly captured, and each experimental group was conducted three times in the statistic, followed by using ImageJ software being processed and subjected to particle analysis for each sphere.

For immunoblotting, cells were lysed in radioimmunoprecipitation assay buffer supplemented with a proteinase inhibitor cocktail and subjected to immunoblotting by indicated antibodies. Immunoblotting assays were repeated at least three times for each dataset.

For biotin pull-down assay, the full-length recombinant proteins of GST-IMPDH2, GST-IMPDH2 N-terminal (1–111 aa), C-terminal (232–514 aa), and CBS (111–232 aa) domain were expressed in *Escherichia coli* BL21 and purified. The purity of the recombinant proteins was resolved by SDS-PAGE, followed by Coomassie blue staining. Magnetic Dynabeads MyOne Streptavidin T1 (Thermo Fisher Scientific) was preincubated with free biotin or biotin-labeled inositol for 30 min at room temperature and then incubated with cell lysates or recombinant proteins rotated for 2 h at 4°C. The beads were washed with PBS three to four times and analyzed by immunoblotting.

For IHC, xenograft tumors or prostate tumors from *TRAMP* mice were fixed with 10% formalin overnight, followed by paraffin-embedded sections. After deparaffization and rehydration slides by xylene and ethanol, antigen retrieval was conducted in citric acid buffer (10 mM, pH 7.0) at 121°C for 15 min, followed by blocking and incubating with Cytokeratin 8 (sc-8020; Santa Cruz) or IMPA1 antibody (sc-374234; Santa Cruz) overnight at 4°C. After incubating with primary antibodies and washing three times, R.T.U. VECTASTAIN ABC-HRP kit was used for the staining procedure. The tissue was incubated with prediluted biotinylated secondary antibody, followed by incubating with VECTASTAIN ABC reagent, peroxidase substrate solution and H&E staining.

Lentiviral infection and sequences of shRNAs

To generate lentivirus-producing cell lines, calcium phosphate was used to transfect with the plasmids of luciferase (control), IMPA1, IMPDH2, CDIPT, INPP1, PI4K2α and PLC β1 shRNA, Flag, Flag-IMPA1, virus Gag-Pol packing vector (pPAX), and virus envelope glycoprotein expression vector (pMD.2G) in 293T cells. Supernatants were collected 48 h after transfection, filtered (0.45 μm), purified by centrifugation, and stored at −80°C. Infections were carried out overnight in the presence of 8 μg/ml Polybrene (Sigma-Aldrich). After viral infection, cells were selected with puromycin (2 μg/ml). The individual mission shRNAs kept in frozen bacterial glycerol were purchased from Sigma-Aldrich. The following shRNAs sequences were used:

IMPA1 #1 for human TRCN0000310192: 5′-CAACGAGACGACGAAGATTAA-3′;

IMPA1 #2 for human TRCN0000296135: 5′-CATCAACTGAAATAGTCAATT-3′;

IMPA1 for mouse #1 TRCN0000081409: 5′-CGGAGAATAATTGCCGCAAAT-3′;

IMPA1 for mouse #2 TRCN0000081410: 5′-GCTGGAGAGATGATTCGTGAA-3′;

IMPA1 for mouse #3 TRCN0000306604: 5′-ATGTTCCAGAAGCCATATTTG-3′;

CDIPT for human TRCN0000035987: 5′-GAGTCACAAGATGATCGACTT-3′;

INPP1 for human TRCN0000051600: 5′-GCTTAGAAAGAA ATCCAGAAA-3′;

PI4K2α for human TRCN0000195093: 5′-CAATGACAACTG GCTGATTAA-3′;

PLCβ1 for human TRCN0000226441: 5′-CAGCGAGATCCT CGGCTTAAT-3′;

IMPDH2 #1 for human TRCN0000026512: 5′-CACCTACAA TGACTTTCTCAT-3′;

T; IMPDH2 #2 for human TRCN0000293612: 5′-CACCTACAA TGACTTTCTCAT-3′;

IMPDH2 #3 for human TRCN0000293547: 5′-GACTGTTTC TTGGAAGAGATA-3′;

IMPDH2 #1 for mouse TRCN0000041338: 5′-GCTGAAGAA ATACCGAGGTAT-3′;

IMPDH2 #2 for mouse TRCN0000041339: 5′-CATGACTAA GAGGGAAGATTT-3′.

qRT-PCR and sequence of primers

For qRT-PCR, isolation of RNA was determined by Quick-RNA Miniprep Kit (R1055; ZYMO RESEARCH) according to the manufacturer's protocol. The generation of cDNA was used by PrimeScript RT Master Mix (RR036A; TaKaRa), followed by qRT-PCR performed using iTaqTM Universal SYBR Green Supermix (172-5125; BioRad) and Applied Biosystems 7300 Real-Time PCR System. mRNA levels were normalized to GAPDH or 18S ribosomal RNA. The following primer pairs were used:

AR forward: 5′-CTCACCAAGCTCCTGGACTC-3′
AR reverse: 5′-CAGGCAGAAGACATCTGAAAG-3′
TMPRSS2 forward: 5′-CTGCCAAGGTGCTTCTCATT-3′
TMPRSS2 reverse: 5′-CTGTCACCCTGGCAAGAATC-3′
FKBP5 forward: 5′-AGGCTGCAAGACTGCAGATC-3′
FKBP5 reverse: 5′-CTTGCCCATTGCTTTATTGG-3′
NDRG1 forward: 5′-ATCACCCAGTTTGCCGTCT-3′
NDRG1 reverse: 5′-GACTCCAGGAAGCATTTCAGCC-3′
SOX2 forward: 5′-GGGAAATGGGAGGGGTGCAAAAGAGG-3′
SOX2 reverse: 5′-TTGCGTGAGTGTGGATGGGATTGGTG-3′
Oct4 forward: 5′-GACAGGGGGAGGGGAGGAGCTAGG-3′
Oct4 reverse: 5′-CTTCCCTCCAACCAGTTGCCCCAAAC-3′
Nanog forward: 5′-CAGTCTGGACACTGGCTGAA-3′
Nanog reverse: 5′-CTCGCTGATTAGGCTCCAAC-3′
EZH2 forward: 5′-AGGACGGCTCCTCTAAACCAT-3′
EZH2 reverse: 5′-CTTGGTGTTGCACTGTGCTT-3′
MYCN forward: 5′-CACAAGGCCCTCAGTACCTC-3′
MYCN reverse: 5′-ACCACGTCGATTTCTTCCTC-3′
CK18 forward: 5′-ATCTTGGTGATGCCTTGGAC-3′
CK18 reverse: 5′-CCTGCTTCTGCTGGCTTAAT-3′
CK5 forward: 5′-ATCGCCACTTACCGCAAGCTGCTGGAGGG-3′
CK5 reverse: 5′-AAACACTGCTTGTGACAACAGAG-3′
CK14 forward: 5′-TTTGGCTGGAGGAGGTCACA-3′
CK14 reverse: 5′-ATCGCCACCTACCGCCGCCTG-3′
CgA forward: 5′-CTGCGCCGGGCAAGT-3′
CgA reverse: 5′-CATCACCTCGGTATCCCCTTT-3′
ENO2 forward: 5′-TGATGACCTGACGGTGACCA-3′
ENO2 reverse: 5′-CAAACAGTTGCAGGCCTTCTC-3′
hTET1 forward: 5′-GCCTTTAAAACTTTGGGCTTC-3′
hTET1 reverse: 5′-TCTGTTGTTGTGCCTCTGGA-3′
LIN28A forward: 5′-GGCCACGGGCTCAGCCGACGACCAT-3′
LIN28A reverse: 5′-AGCCGAACCCCATGCGCACGTTGAACC-3′
IMPDH2 forward: 5′-GCTCCTGTGCCTGATGGAAT-3′
IMPDH2 reverse: 5′-CGGGCTCCTCCCCAAAATAA-3′
IMPA1 forward: 5′-GCAAGACAAGCTGGAGAGGT-3′
IMPA1 reverse: 5′-TGATCCATGTGGGGTTGTCG-3′
GAPDH forward: 5′-CCCACTCCTCCACCTTTGAC-3′
GAPDH reverse: 5′-TCTCTCTTCCTCTTGTGCTCTTG-3′
18S rRNA forward: 5′-GTAACCCGTTGAACCCCATT-3′
18S rRNA reverse: 5′-CCATCCAATCGGTAGTAGCG-3′
NKX3.1 forward: 5′-CCGCTTCCAAAGACCTAGAGGA-3′
NKX3.1 reverse: 5′-ACCGTCGTCCTCGGTCCTTGG-3′.

Cell survival, colony formation, soft agar, in vivo xenograft assay, and PDX model

Cancer cells were counted and ∼3,000 cells per well were seeded in a 96-well cell culture plate. After incubation at 37°C in a humidified atmosphere with 5% CO_2 for 24 h, cells were treated with enzalutamide, MZB, MPA, or LiCl (the treatment of concentration and time for each reagent are described in the figure legends), followed by adding 0.5 mg/ml 3′-(4,5-dimethylthiazol-2-yl)-2,5-diphenyl tetrazolium bromide (MTT) for 4 h. Formazan was dissolved by DMSO and measured OD at 570 nm. For Cell Counting Kit-8 (CCK-8), cancer cells were treated with enzalutamide, MZB, MPA, or LiCl, followed by adding 10 µl of CCK-8 reagent to each well for 4 h and measuring OD at 450 nm. For colony formation assay, 3,000 cells were seeded in a 24-well cell culture plate in the presence of enzalutamide, MZB, MPA, or LiCl. The culture medium upon each drug treatment was changed every 2 days for 14 days. Cells were washed with PBS and stained with 2% Methyl Blue in 50% ethanol. For soft agar assay, 1.5 ml of culture medium containing 0.6% Difco agar (BD Biosciences) was used as the base layer of a 6-well dish. The base layer was overlaid with 1.5 ml of a second layer of 0.3% agar containing a suspension of 10,000 cells. After 21 days in culture, cells were stained (1 h, room temperature) with 0.05% crystal violet (Sigma-Aldrich). To quantify the number of colonies, the staining colonies were scanned by scanner, and each experimental group conducted triplicate in the statistic, followed by using ImageJ software being processed and subjected to particle analysis for each colony. Quantification of the number of colonies is shown as the mean ± SEM of three independent experiments for each group.

For the in vivo xenograft assay, 10^6 cancer cells stably expressing shLuc, shIMPA1 #1, shIMPA1 #2, or shIMPDH2 #1 were subcutaneously injected into athymic male nude mice (four to five mice for each group), followed by intraperitoneal injection with 30 mg/kg of inositol or 30 mg/kg of guanosine every 2 days. The tumor size was measured every 2–3 days with a caliper once palpable tumors showed, and tumor volume was determined with the standard formula $LW^2/2$, where L is the longest diameter and W is the shortest diameter. For enzalutamide treatment, 10^6 of 22RV1 parental cells or those expressing shLuc or shIMPA1 were subcutaneously injected into athymic male nude mice (four to five mice for each group). While developed tumors reached a volume of around 150 mm^3, mice were intraperitoneally injected with vehicle (5% DMSO+1% CMC

Na+1% Tween-80) or 5 mg/kg of enzalutamide every 2 days for 40 days, and tumors size was measured every 3 days with a caliper. For enzalutamide, MZB or LiCl treatment, 10^6 of 22RV1 parental cells were subcutaneously injected into athymic male nude mice (four to five mice for each group). While developed tumors reached a volume of around 20 mm^3, mice were intraperitoneally injected with vehicle, 5 mg/kg of enzalutamide daily for 18 days, 200 mg/kg of MZB daily for 7 days; no treatment for 4 days; 100 mg/kg of MZB daily for 7 days, or 200 mg/kg daily of LiCl for 18 days and tumors size was measured every 3 days with a caliper.

For PDX model, PDX prostate tumor (Model ID: J000077451; The Jackson Laboratory) was finely minced with surgical scissors and a scalpel blade in a sterile petri dish on an ice pack. The tumor tissue was evenly divided and engrafted into NOD-*scid* IL2Rg^{null} (NSG) mice (n = 5 for each experimental group). Mice were anesthetized with isoflurane, fur was removed using clippers, and skin was cleansed with 70% ethanol prior to engraftment. When the tumors reached a volume of around 20 mm^3, mice were intraperitoneally administrated with enzalutamide, MZB, or LiCl, similar to the treatment of 22RV1 xenograft model, and tumors size was measured every 3 days with a caliper.

For castrated NOD/SCID mouse model, surgical castrated NOD/SCID mice (n = 5 for each experimental group) subcutaneously injected with 22RV1 cells were intraperitoneally injected with vehicle or 5 mg/kg of enzalutamide (Enza), 200 mg/kg of LiCl, 100 mg/kg of MZB, 5 mg/kg of enzalutamide (Enza) in combination with 200 mg/kg of LiCl and 5 mg/kg of enzalutamide (Enza) in combination with 100 mg/kg of MZB three times a week for 6 wk, and tumor volume was measured with indicated days. When the tumors were palpable, mice were intraperitoneally administrated with enzalutamide, MZB, or LiCl, similar to the treatment of 22RV1 xenograft model, and the tumor size was measured every 3 days with a caliper.

For the castrated *TRAMP* mouse model, surgical castration in *TRAMP* mice (n = 5 for each experimental group) was performed at the age of 8 wk. *TRAMP* mice at the age of 9 wk were intraperitoneally administrated with vehicle, 5 mg/kg of enzalutamide (Enza), 100 mg/kg of MZB, 200 mg/kg of LiCl, 5 mg/kg of Enza in combination with 100 mg/kg of MZB, and 5 mg/kg of Enza in combination with 200 mg/kg of LiCl three times a week for 18 wk. Prostate tissues were harvested, followed by H&E staining at the age of 6 mo.

Patients, human materials, and IHC

The human samples from prostate cancer patients used in this study were approved by the Institutional Review Board (IRB) of Wake Forest Cancer Center (IRB00037560) and Chi Mei Medical Center (IRB10707004). All research was performed according to relevant guidelines and protocol approved by the IRB of Chi Mei Medical Center and Wake Forest Cancer Center. At Chi Mei Medical Center, the samples were retrieved from the biobank in a deidentified manner. Following local rules, informed consent was obtained from all prostate cancer patients before being enrolled into the biobank. The serum samples from prostate cancer patients used in this study were approved by Wake Forest IRB (IRB00037560). Informed consent was obtained from all prostate cancer patients involved in this study. IHC was conducted under the standard procedure using 1:100 dilution with primary IMPA1 and 1:200 dilution with IMPDH2 antibodies. The secondary antibody was incubated for 30 min and then developed for 5 min with 3-diaminobenzidine. IHC samples were scored manually by Dr. Chien-Feng Li under the multi-headed microscope as previously described (Chan et al., 2012).

Inositol level, IMPDH2 activity measurement, ALDEFLUOR assay, and FACS

The inositol levels and the activity of inosine-5′-monophosphate dehydrogenase (IMPDH) in cells were determined by the K-INOSL Assay Kit (820517; Megazyme) and IMPDH enzymatic activity assay kit (K495; BioVision), respectively, according to the manufacturer's protocol. For in vitro IMPDH activity assay, 40 μM of inositol or 10 μM of MPA were incubated with recombinant IMPDH2 enzyme at room temperature for 30 min, followed by adding substrate and detection buffer, which were provided from the assay kit, and the OD at 450 nm was measured at 37°C for 1 h in kinetic mode. For the ALDH positive cells analysis, the ALDH activity of the cells was measured by ALDEFLUOR assay Kit according to manufacturer's protocol. Briefly, 200,000 cells were counted and stained by ALDEFLUOR reagent with and without N,N-diethylaminobenzaldehyde (DEAB) treatment at 37°C for 45 min, followed by washing with ALDEFLUOR assay buffer and flow cytometry analysis (BD Accuri C6 Flow Cytometer). For FACS, cells were labeled with ALDEFLUOR Kit and sorted using MoFlo Astrios Cell Sorter (BECKMAN COULTER) in two ways including the highest 10% ALDH positive cells (ALDH^{high}) and the lowest 10% ALDH negative cells (ALDH$^{low/-}$), followed by cell culture and immunoblotting.

RNA-seq and microarray

The total RNA was extracted using Quick-RNA Miniprep Kit (Zymo Research) from ALDH$^{low/-}$ and ALDH^{high} cells isolated from LNCaP and PC3 cells or 22RV1 cells stably expressing shLuc, shIMPA1 #1, and shIMPDH2 #2. RNA-seq reads were trimmed to remove possible adapter sequences and nucleotides with poor quality using Trimmomatic v.0.36.

The trimmed reads were mapped to the *Homo sapiens* GRCh38 with ERCC genes reference genome available on ENSEMBL using the STAR aligner v.2.5.2b. The STAR aligner is a splice aligner that detects splice junctions and incorporates them to help align the entire read sequences. BAM files were generated as a result of this step.

Unique gene hit counts were calculated by using featureCounts from the Subread package v.1.5.2. The hit counts were summarized and reported using the gene ID feature. Only unique reads that fell within exon regions were counted. After the extraction of gene hit counts, the gene hit counts table was used for downstream differential expression analysis.

Using DESeq2, a comparison of gene expression between the customer-defined groups of samples was performed. The Wald test was used to generate P values and $\log_2$ fold changes. Genes with an adjusted P value <0.05 and absolute $\log_2$ fold change >1 were called differentially expressed genes for each comparison.

The raw data for RNA-seq have been deposited in publicly available GEO databases (GSE270564 and GSE270565).

For microarray analysis, $ALDH^{low/-}$ and $ALDH^{high}$ cells from PC3 cells were sorted by FACS, followed by genomic DNA extraction. The Affymetrix array system provides exon-level expression profiling of the whole genome on a single array. The arrays contain probes for over 1 million exon clusters within regions of the genome known or predicted to be transcribed. Gene differential profiles are generated by adjusted P value and absolute $\log_2$ fold change after gene symbol annotation.

Metabolomics analysis

$ALDH^{low/-}$ and $ALDH^{high}$ cells isolated from LNCaP and PC3 were washed twice in ice-cold PBS and lysed in 1 ml of ice-cold 80% methanol with the plates placed on dry ice to quench metabolism. After 5 min, cells were scraped and transferred into 1.5-ml tubes and incubated at 80°C for 30 min. Lysates were centrifuged at 13,000 rpm for 10 min and supernatants were transferred to new vials and dried at 30°C in a Speed-Vac for 3 h.

The targeted LC-MS/MS method was modeled and developed as previously described (Carroll et al., 2015; Hsu et al., 2021). Briefly, all LC-MS/MS experiments were performed on an Agilent 1290 UPLC-6490 QQQ-MS system. Each sample was injected twice, 10 ml for analysis using negative ionization mode and 4 ml for analysis using positive ionization mode. Both chromatographic separations were performed in hydrophilic interaction chromatography mode on a Waters XBridge BEH Amide column (150 × 2.1 mm, 2.5 µm particle size; Waters Corporation). The flow rate was 0.3 ml/min, autosampler temperature was kept at 4°C, and the column compartment was set at 40°C. The mobile phase was composed of Solvents A (10 mM ammonium acetate, 10 mM ammonium hydroxide in 95% H_2O/5% ACN) and B (10 mM ammonium acetate, 10 mM ammonium hydroxide in 95% ACN/5% H_2O).

After the initial 1 min isocratic elution of 90% B, the percentage of Solvent B decreased to 40% at t = 11 min. The composition of Solvent B was maintained at 40% for 4 min (t = 15 min), and then the percentage of B gradually went back to 90% to prepare for the next injection. The mass spectrometer is equipped with an electrospray ionization source. Targeted data acquisition was performed in a multiple reaction–monitoring (MRM) mode. The whole LC-MS system was controlled by Agilent Masshunter. Workstation software. The extracted MRM peaks were integrated using Agilent MassHunter Quantitative Data Analysis.

Statistical analysis

Statistical significance was identified by two-tailed unpaired Student's t test using Prism software for cancer sphere assay, colony formation assay, and qRT-PCR according to three independent experiments for each group. Statistical analysis for Kaplan–Meier plots was performed using a two-sided log-rank test. In addition, a one-sided log-rank test was used to determine whether the *TRAMP/Impa1*$^{FL/FL}$*/PB-Cre4* mice had better survival outcomes than *TRAMP/PB-Cre4* mice. Statistical analysis for H-score and inositol levels from clinical samples were performed using the Mann–Whitney U test. P values of <0.05 were considered statistically significant; *, P < 0.05; **, P < 0.01; ***, P < 0.001; NS, non-significant.

Online supplemental material

Fig. S1 shows RNA-seq analysis from sorted $ALDH^{high}$ and $ALDH^{low/-}$ LNCaP cells, immunoblotting of sorted $ALDH^{high}$ and $ALDH^{low/-}$ 22RV1 cells, and adherent/spheroid prostate cancer cells; and ALDEFLUOR assay from control knockdown and IMPA1 knockdown cells. Fig. S2 shows colony formation assay from sorted $ALDH^{high}$ and $ALDH^{low/-}$ LNCaP and TRAMP-C2 cells upon IMPA1 knockdown and IMPDH2 knockdown. Fig. S3 shows cancer sphere assay and tumor organoids from *TRMAP* mouse model upon knockdown of the key enzymes involved in PI and phosphoinositides cycles. Fig. S4 shows the analysis of cBioPortal database, GEPIA database, and PrognoScan database and describes AR, IMPA1, and IMPDH2 expression by IHC staining in various prostate cancer patients. Fig. S5 shows the characteristics of EnzaR cell lines and colony formation assay in response to the treatment of the different metabolites and inhibitors. Table S1 shows identified inositol-binding proteins by mass spectrometry. Data S1 shows the analysis of the copy number of IMPA1 in prostate cancer patients.

Data availability

All data reported in this paper are available upon request to the corresponding author. The RNA-seq data from LNCaP $ALDH^{high}$ cell and LNCaP $ALDH^{low/-}$ cells and 22RV1 cells were deposited in NCBI Gene Expression Omnibus database accession numbers: GSE270564 and GSE270565. Metabolomics data and microarray data were deposited at the following permanent URLs: metabolomics: https://figshare.com/s/01c3a4c13ecdff7be728; microarray: https://figshare.com/s/3ff185e2781d54b039cf; RNA-seq: https://figshare.com/s/5081739c2f2cba50553d; https://figshare.com/s/cc1fbc04cda684abf0a6.

Acknowledgments

We are grateful to the members of H.-K. Lin's lab for critical inputs and suggestions. We thank the technical support and discussion of ALDH negative/positive cell sorting from Dr. John F. Whitesides (Flow Cytometry Shared Resource, Wake Forest University School of Medicine). We acknowledge the support of the Wake Forest Baptist Comprehensive Cancer Center Cell & Cellular Imaging & Flow Cytometry Shared Resources & Tumor Tissue and Pathology Shared Resource Core, supported by the National Cancer Institute's Cancer Center Support Grant (P30CA012197). We also acknowledge the support of Flow Cytometry Shared Resource from Duke Cancer Institute and Duke Human Vaccine Institute, Light Microscopy Core Facility, and histology laboratory of the BioRepository & Precision Pathology Center at Duke University School of Medicine.

This research was supported in part by Postdoctoral Research Abroad Program from the Ministry of Science and Technology in Taiwan to C.-C. Hsu (105-2917-I-564-067) and start-ups from Wake Forest School of Medicine, Endowed funds for Anderson Discovery Professor for Cancer Research and Fred and Janet Sanfilippo Distinguished Professor, Start-ups from the Duke

University School of Medicine, National Institutes of Health (NIH) grants R01CA256158, R01CA248037, and R01CA270617 to H.-K. Lin, and NIH grant R01CA277682 to H.-Y. Li and H.-K. Lin.

Author contributions: C.-C. Hsu: Conceptualization, Data curation, Formal analysis, Funding acquisition, Investigation, Methodology, Project administration, Resources, Software, Supervision, Validation, Visualization, Writing - original draft, Writing - review & editing, G. Wang: Data curation, Resources, C.-F. Li: Investigation, Methodology, Resources, Validation, X. Zhang: Investigation, Z. Cai: Investigation, T. Chen: Methodology, Resources, B.-S. Pan: Conceptualization, R.K. Manne: Writing - review & editing, G. Deep: Resources, Writing - review & editing, H. Gu: Data curation, Methodology, Y. Wang: Data curation, Funding acquisition, Resources, D. Peng: Investigation, Vasudevarao Penugurti: Methodology, Writing - review & editing, X. Zhou: Supervision, Z. Xu: Formal analysis, Z. Chen: Data curation, Methodology, M. Chen: Writing - review & editing, A.J. Armstrong: Writing - original draft, Writing - review & editing, J. Huang: Conceptualization, Resources, Writing - review & editing, H.-Y. Li: Supervision, Writing - review & editing, H.-K. Lin: Conceptualization, Funding acquisition, Project administration, Supervision, Writing - original draft, Writing - review & editing.

Disclosures: A.J. Armstrong reported personal fees from Pfizer/Astellas, personal fees from AstraZeneca, personal fees from Bayer, personal fees from Novartis, grants from BMS, and personal fees from Merck during the conduct of the study. J. Huang reported personal fees from Kingmed Diagnostics, personal fees from Artera, and personal fees from York Biotechnology outside the submitted work. H.-K. Lin reported personal fees from Stablix, Inc. outside the submitted work. No other disclosures were reported.

Submitted: 8 October 2023
Revised: 9 July 2024
Accepted: 19 August 2024

References

Aggarwal, R., J. Huang, J.J. Alumkal, L. Zhang, F.Y. Feng, G.V. Thomas, A.S. Weinstein, V. Friedl, C. Zhang, O.N. Witte, et al. 2018. Clinical and genomic characterization of treatment-emergent small-cell neuroendocrine prostate cancer: A multi-institutional prospective study. *J. Clin. Oncol.* 36:2492–2503. https://doi.org/10.1200/JCO.2017.77.6880

Beltran, H., D.S. Rickman, K. Park, S.S. Chae, A. Sboner, T.Y. MacDonald, Y. Wang, K.L. Sheikh, S. Terry, S.T. Tagawa, et al. 2011. Molecular characterization of neuroendocrine prostate cancer and identification of new drug targets. *Cancer Discov.* 1:487–495. https://doi.org/10.1158/2159-8290.CD-11-0130

Berlin, R.D., and J.M. Oliver. 1975. Membrane transport of purine and pyrimidine bases and nucleosides in animal cells. *Int. Rev. Cytol.* 42: 287–336. https://doi.org/10.1016/S0074-7696(08)60983-3

Burrell, A.L., and J.M. Kollman. 2022. IMPDH dysregulation in disease: A mini review. *Biochem. Soc. Trans.* 50:71–82. https://doi.org/10.1042/BST20210446

Carey, B.W., L.W. Finley, J.R. Cross, C.D. Allis, and C.B. Thompson. 2015. Intracellular α-ketoglutarate maintains the pluripotency of embryonic stem cells. *Nature*. 518:413–416. https://doi.org/10.1038/nature13981

Carroll, P.A., D. Diolaiti, L. McFerrin, H. Gu, D. Djukovic, J. Du, P.F. Cheng, S. Anderson, M. Ulrich, J.B. Hurley, et al. 2015. Deregulated Myc requires MondoA/Mlx for metabolic reprogramming and tumorigenesis. *Cancer Cell*. 27:271–285. https://doi.org/10.1016/j.ccell.2014.11.024

Chan, C.H., C.F. Li, W.L. Yang, Y. Gao, S.W. Lee, Z. Feng, H.Y. Huang, K.K. Tsai, L.G. Flores, Y. Shao, et al. 2012. The Skp2-SCF E3 ligase regulates Akt ubiquitination, glycolysis, herceptin sensitivity, and tumorigenesis. *Cell*. 149:1098–1111. https://doi.org/10.1016/j.cell.2012.02.065

Chen, Z., L.C. Trotman, D. Shaffer, H.K. Lin, Z.A. Dotan, M. Niki, J.A. Koutcher, H.I. Scher, T. Ludwig, W. Gerald, et al. 2005. Crucial role of p53-dependent cellular senescence in suppression of Pten-deficient tumorigenesis. *Nature*. 436:725–730. https://doi.org/10.1038/nature03918

Chiaverotti, T., S.S. Couto, A. Donjacour, J.H. Mao, H. Nagase, R.D. Cardiff, G.R. Cunha, and A. Balmain. 2008. Dissociation of epithelial and neuroendocrine carcinoma lineages in the transgenic adenocarcinoma of mouse prostate model of prostate cancer. *Am. J. Pathol.* 172:236–246. https://doi.org/10.2353/ajpath.2008.070602

Clark, D.W., and K. Palle. 2016. Aldehyde dehydrogenases in cancer stem cells: Potential as therapeutic targets. *Ann. Transl. Med.* 4:518. https://doi.org/10.21037/atm.2016.11.82

Cryns, K., A. Shamir, N. Van Acker, I. Levi, G. Daneels, I. Goris, J.A. Bouwknecht, L. Andries, S. Kass, G. Agam, et al. 2008. IMPA1 is essential for embryonic development and lithium-like pilocarpine sensitivity. *Neuropsychopharmacology*. 33:674–684. https://doi.org/10.1038/sj.npp.1301431

Dardenne, E., H. Beltran, M. Benelli, K. Gayvert, A. Berger, L. Puca, J. Cyrta, A. Sboner, Z. Noorzad, T. MacDonald, et al. 2016. N-myc induces an EZH2-mediated transcriptional program driving neuroendocrine prostate cancer. *Cancer Cell*. 30:563–577. https://doi.org/10.1016/j.ccell.2016.09.005

Davies, A.H., H. Beltran, and A. Zoubeidi. 2018. Cellular plasticity and the neuroendocrine phenotype in prostate cancer. *Nat. Rev. Urol.* 15: 271–286. https://doi.org/10.1038/nrurol.2018.22

Di Paolo, G., and P. De Camilli. 2006. Phosphoinositides in cell regulation and membrane dynamics. *Nature*. 443:651–657. https://doi.org/10.1038/nature05185

Elia, I., M. Rossi, S. Stegen, D. Broekaert, G. Doglioni, M. van Gorsel, R. Boon, C. Escalona-Noguero, S. Torrekens, C. Verfaillie, et al. 2019. Breast cancer cells rely on environmental pyruvate to shape the metastatic niche. *Nature*. 568:117–121. https://doi.org/10.1038/s41586-019-0977-x

Faubert, B., K.Y. Li, L. Cai, C.T. Hensley, J. Kim, L.G. Zacharias, C. Yang, Q.N. Do, S. Doucette, D. Burguete, et al. 2017. Lactate metabolism in human lung tumors. *Cell*. 171:358–371.e9. https://doi.org/10.1016/j.cell.2017.09.019

Faubert, B., A. Solmonson, and R.J. DeBerardinis. 2020. Metabolic reprogramming and cancer progression. *Science*. 368:eaaw5473. https://doi.org/10.1126/science.aaw5473

Ferone, G., J.Y. Song, K.D. Sutherland, R. Bhaskaran, K. Monkhorst, J.P. Lambooij, N. Proost, G. Gargiulo, and A. Berns. 2016. SOX2 is the determining oncogenic switch in promoting lung squamous cell carcinoma from different cells of origin. *Cancer Cell*. 30:519–532. https://doi.org/10.1016/j.ccell.2016.09.001

Gelman, I.H. 2016. How the TRAMP model revolutionized the study of prostate cancer progression. *Cancer Res.* 76:6137–6139. https://doi.org/10.1158/0008-5472.CAN-16-2636

Germann, M., A. Wetterwald, N. Guzmán-Ramirez, G. van der Pluijm, Z. Culig, M.G. Cecchini, E.D. Williams, and G.N. Thalmann. 2012. Stem-like cells with luminal progenitor phenotype survive castration in human prostate cancer. *Stem Cells*. 30:1076–1086. https://doi.org/10.1002/stem.1087

Hsu, C.C., Z.G. Xu, J. Lei, Z.Z. Chen, H.Y. Li, and H.K. Lin. 2022. Identification of myo-inositol-binding proteins by using the biotin pull-down strategy in cultured cells. *STAR Protoc.* 3:101385. https://doi.org/10.1016/j.xpro.2022.101385

Hsu, C.-C., X. Zhang, G. Wang, W. Zhang, Z. Cai, B.-S. Pan, H. Gu, C. Xu, G. Jin, X. Xu, et al. 2021. Inositol serves as a natural inhibitor of mitochondrial fission by directly targeting AMPK. *Mol. Cell*. 81:3803–3819.e7. https://doi.org/10.1016/j.molcel.2021.08.025

Hu, Y., and G.K. Smyth. 2009. ELDA: Extreme limiting dilution analysis for comparing depleted and enriched populations in stem cell and other assays. *J. Immunol. Methods*. 347:70–78. https://doi.org/10.1016/j.jim.2009.06.008

Hui, S., J.M. Ghergurovich, R.J. Morscher, C. Jang, X. Teng, W. Lu, L.A. Esparza, T. Reya, J. Le Zhan, Yanxiang Guo, et al. 2017. Glucose feeds the TCA cycle via circulating lactate. *Nature*. 551:115–118. https://doi.org/10.1038/nature24057

Hüser, L., D. Novak, V. Umansky, P. Altevogt, and J. Utikal. 2018. Targeting SOX2 in anticancer therapy. *Expert Opin. Ther. Targets*. 22:983–991. https://doi.org/10.1080/14728222.2018.1538359

Jackson, R.C., G. Weber, and H.P. Morris. 1975. IMP dehydrogenase, an enzyme linked with proliferation and malignancy. *Nature*. 256:331–333. https://doi.org/10.1038/256331a0

Jahchan, N.S., J.S. Lim, B. Bola, K. Morris, G. Seitz, K.Q. Tran, L. Xu, F. Trapani, C.J. Morrow, S. Cristea, et al. 2016. Identification and targeting of long-term tumor-propagating cells in small cell lung cancer. *Cell Rep.* 16: 644–656. https://doi.org/10.1016/j.celrep.2016.06.021

Kim, J., B.K. Koo, and J.A. Knoblich. 2020. Human organoids: Model systems for human biology and medicine. *Nat. Rev. Mol. Cell Biol.* 21:571–584. https://doi.org/10.1038/s41580-020-0259-3

Kregel, S., K.J. Kiriluk, A.M. Rosen, Y. Cai, E.E. Reyes, K.B. Otto, W. Tom, G.P. Paner, R.Z. Szmulewitz, and D.J. Vander Griend. 2013. Sox2 is an androgen receptor-repressed gene that promotes castration-resistant prostate cancer. *PLoS One*. 8:e53701. https://doi.org/10.1371/journal.pone.0053701

Ku, S.Y., S. Rosario, Y. Wang, P. Mu, M. Seshadri, Z.W. Goodrich, M.M. Goodrich, D.P. Labbé, E.C. Gomez, J. Wang, et al. 2017. Rb1 and Trp53 cooperate to suppress prostate cancer lineage plasticity, metastasis, and antiandrogen resistance. *Science*. 355:78–83. https://doi.org/10.1126/science.aah4199

Lee, S.O., Z. Ma, C.R. Yeh, J. Luo, T.H. Lin, K.P. Lai, S. Yamashita, L. Liang, J. Tian, L. Li, et al. 2013. New therapy targeting differential androgen receptor signaling in prostate cancer stem/progenitor vs. non-stem/progenitor cells. *J. Mol. Cell Biol.* 5:14–26. https://doi.org/10.1093/jmcb/mjs042

Lin, H.K., Z. Chen, G. Wang, C. Nardella, S.W. Lee, C.H. Chan, W.L. Yang, J. Wang, A. Egia, K.I. Nakayama, et al. 2010. Skp2 targeting suppresses tumorigenesis by Arf-p53-independent cellular senescence. *Nature*. 464:374–379. https://doi.org/10.1038/nature08815

Lu, C., and C.B. Thompson. 2012. Metabolic regulation of epigenetics. *Cell Metab.* 16:9–17. https://doi.org/10.1016/j.cmet.2012.06.001

Mashimo, T., K. Pichumani, V. Vemireddy, K.J. Hatanpaa, D.K. Singh, S. Sirasanagandla, S. Nannepaga, S.G. Piccirillo, Z. Kovacs, C. Foong, et al. 2014. Acetate is a bioenergetic substrate for human glioblastoma and brain metastases. *Cell*. 159:1603–1614. https://doi.org/10.1016/j.cell.2014.11.025

Mayers, J.R., M.E. Torrence, L.V. Danai, T. Papagiannakopoulos, S.M. Davidson, M.R. Bauer, A.N. Lau, B.W. Ji, P.D. Dixit, A.M. Hosios, et al. 2016. Tissue of origin dictates branched-chain amino acid metabolism in mutant Kras-driven cancers. *Science*. 353:1161–1165. https://doi.org/10.1126/science.aaf5171

Mu, P., Z. Zhang, M. Benelli, W.R. Karthaus, E. Hoover, C.C. Chen, J. Wongvipat, S.Y. Ku, D. Gao, Z. Cao, et al. 2017. SOX2 promotes lineage plasticity and antiandrogen resistance in TP53- and RB1-deficient prostate cancer. *Science*. 355:84–88. https://doi.org/10.1126/science.aah4307

Murai, F., D. Koinuma, A. Shinozaki-Ushiku, M. Fukayama, K. Miyaozono, and S. Ehata. 2015. EZH2 promotes progression of small cell lung cancer by suppressing the TGF-β-Smad-ASCL1 pathway. *Cell Discov.* 1:15026. https://doi.org/10.1038/celldisc.2015.26

Nyquist, M.D., A. Corella, I. Coleman, N. De Sarkar, A. Kaipainen, G. Ha, R. Gulati, L. Ang, P. Chatterjee, J. Lucas, et al. 2020. Combined TP53 and RB1 loss promotes prostate cancer resistance to a spectrum of therapeutics and confers vulnerability to replication stress. *Cell Rep.* 31: 107669. https://doi.org/10.1016/j.celrep.2020.107669

Pérez-Ibave, D.C., C.H. Burciaga-Flores, and M.A. Elizondo-Riojas. 2018. Prostate-specific antigen (PSA) as a possible biomarker in non-prostatic cancer: A review. *Cancer Epidemiol.* 54:48–55. https://doi.org/10.1016/j.canep.2018.03.009

Qin, J., X. Liu, B. Laffin, X. Chen, G. Choy, C.R. Jeter, T. Calhoun-Davis, H. Li, G.S. Palapattu, S. Pang, et al. 2012. The PSA(-/lo) prostate cancer cell population harbors self-renewing long-term tumor-propagating cells that resist castration. *Cell Stem Cell*. 10:556–569. https://doi.org/10.1016/j.stem.2012.03.009

Quaglia, F., S.R. Krishn, Y. Wang, D.W. Goodrich, P. McCue, A.V. Kossenkov, A.C. Mandigo, K.E. Knudsen, P.H. Weinreb, E. Corey, et al. 2021. Differential expression of αVβ3 and αVβ6 integrins in prostate cancer progression. *PLoS One*. 16:e0244985. https://doi.org/10.1371/journal.pone.0244985

Ran, F.A., P.D. Hsu, C.Y. Lin, J.S. Gootenberg, S. Konermann, A.E. Trevino, D.A. Scott, A. Inoue, S. Matoba, Y. Zhang, and F. Zhang. 2013a. Double nicking by RNA-guided CRISPR Cas9 for enhanced genome editing specificity. *Cell*. 154:1380–1389. https://doi.org/10.1016/j.cell.2013.08.021

Ran, F.A., P.D. Hsu, J. Wright, V. Agarwala, D.A. Scott, and F. Zhang. 2013b. Genome engineering using the CRISPR-Cas9 system. *Nat. Protoc.* 8: 2281–2308. https://doi.org/10.1038/nprot.2013.143

Reya, T., S.J. Morrison, M.F. Clarke, and I.L. Weissman. 2001. Stem cells, cancer, and cancer stem cells. *Nature*. 414:105–111. https://doi.org/10.1038/35102167

Ruan, D., J. He, C.F. Li, H.J. Lee, J. Liu, H.K. Lin, and C.H. Chan. 2017. Skp2 deficiency restricts the progression and stem cell features of castration-resistant prostate cancer by destabilizing Twist. *Oncogene*. 36: 4299–4310. https://doi.org/10.1038/onc.2017.64

Sarkar, A., and K. Hochedlinger. 2013. The sox family of transcription factors: Versatile regulators of stem and progenitor cell fate. *Cell Stem Cell*. 12: 15–30. https://doi.org/10.1016/j.stem.2012.12.007

Seiler, D., J. Zheng, G. Liu, S. Wang, J. Yamashiro, R.E. Reiter, J. Huang, and G. Zeng. 2013. Enrichment of putative prostate cancer stem cells after androgen deprivation: Upregulation of pluripotency transactivators concurs with resistance to androgen deprivation in LNCaP cell lines. *Prostate*. 73:1378–1390. https://doi.org/10.1002/pros.22685

Senda, M., and Y. Natsumeda. 1994. Tissue-differential expression of two distinct genes for human IMP dehydrogenase (E.C.1.1.1.205). *Life Sci.* 54: 1917–1926. https://doi.org/10.1016/0024-3205(94)90150-3

Sintchak, M.D., M.A. Fleming, O. Futer, S.A. Raybuck, S.P. Chambers, P.R. Caron, M.A. Murcko, and K.P. Wilson. 1996. Structure and mechanism of inosine monophosphate dehydrogenase in complex with the immunosuppressant mycophenolic acid. *Cell*. 85:921–930. https://doi.org/10.1016/S0092-8674(00)81275-1

Tang, X.Y., S. Wu, D. Wang, C. Chu, Y. Hong, M. Tao, H. Hu, M. Xu, X. Guo, and Y. Liu. 2022. Human organoids in basic research and clinical applications. *Signal Transduct. Target. Ther.* 7:168. https://doi.org/10.1038/s41392-022-01024-9

Traut, T.W. 1994. Physiological concentrations of purines and pyrimidines. *Mol. Cell. Biochem.* 140:1–22. https://doi.org/10.1007/BF00928361

Valvezan, A.J., M. Turner, A. Belaid, H.C. Lam, S.K. Miller, M.C. McNamara, C. Baglini, B.E. Housden, N. Perrimon, D.J. Kwiatkowski, et al. 2017. mTORC1 couples nucleotide synthesis to nucleotide demand resulting in a targetable metabolic vulnerability. *Cancer Cell*. 32:624–638.e5. https://doi.org/10.1016/j.ccell.2017.09.013

van den Hoogen, C., G. van der Horst, H. Cheung, J.T. Buijs, J.M. Lippitt, N. Guzmán-Ramírez, F.C. Hamdy, C.L. Eaton, G.N. Thalmann, M.G. Cecchini, et al. 2010. High aldehyde dehydrogenase activity identifies tumor-initiating and metastasis-initiating cells in human prostate cancer. *Cancer Res.* 70:5163–5173. https://doi.org/10.1158/0008-5472.CAN-09-3806

Varlakhanova, N.V., R.F. Cotterman, W.N. deVries, J. Morgan, L.R. Donahue, S. Murray, B.B. Knowles, and P.S. Knoepfler. 2010. Myc maintains embryonic stem cell pluripotency and self-renewal. *Differentiation*. 80: 9–19. https://doi.org/10.1016/j.diff.2010.05.001

Wolpaw, A.J., R. Bayliss, G. Büchel, C.V. Dang, M. Eilers, W.C. Gustafson, G.H. Hansen, N. Jura, S. Knapp, M.A. Lemmon, et al. 2021. Drugging the "undruggable" MYCN oncogenic transcription factor: Overcoming previous obstacles to impact childhood cancers. *Cancer Res.* 81: 1627–1632. https://doi.org/10.1158/0008-5472.CAN-20-3108

Yamagishi, M., and K. Uchimaru. 2017. Targeting EZH2 in cancer therapy. *Curr. Opin. Oncol.* 29:375–381. https://doi.org/10.1097/CCO.0000000000000390

Yu, Y., P. Deng, B. Yu, J.M. Szymanski, T. Aghaloo, C. Hong, and C.Y. Wang. 2017. Inhibition of EZH2 promotes human embryonic stem cell differentiation into mesoderm by reducing H3K27me3. *Stem Cell Rep.* 9: 752–761. https://doi.org/10.1016/j.stemcr.2017.07.016

Zhang, S., and W. Cui. 2014. Sox2, a key factor in the regulation of pluripotency and neural differentiation. *World J. Stem Cells*. 6:305–311. https://doi.org/10.4252/wjsc.v6.i3.305

Zhang, W., G. Wang, Z.G. Xu, H. Tu, F. Hu, J. Dai, Y. Chang, Y. Chen, Y. Lu, H. Zeng, et al. 2019. Lactate is a natural suppressor of RLR signaling by targeting MAVS. *Cell*. 178:176–189.e15. https://doi.org/10.1016/j.cell.2019.05.003

Zhou, Z., A. Flesken-Nikitin, D.C. Corney, W. Wang, D.W. Goodrich, P. Roy-Burman, and A.Y. Nikitin. 2006. Synergy of p53 and Rb deficiency in a conditional mouse model for metastatic prostate cancer. *Cancer Res.* 66: 7889–7898. https://doi.org/10.1158/0008-5472.CAN-06-0486

Zhou, Z., A. Flesken-Nikitin, and A.Y. Nikitin. 2007. Prostate cancer associated with p53 and Rb deficiency arises from the stem/progenitor cell-enriched proximal region of prostatic ducts. *Cancer Res.* 67:5683–5690. https://doi.org/10.1158/0008-5472.CAN-07-0768

Supplemental material

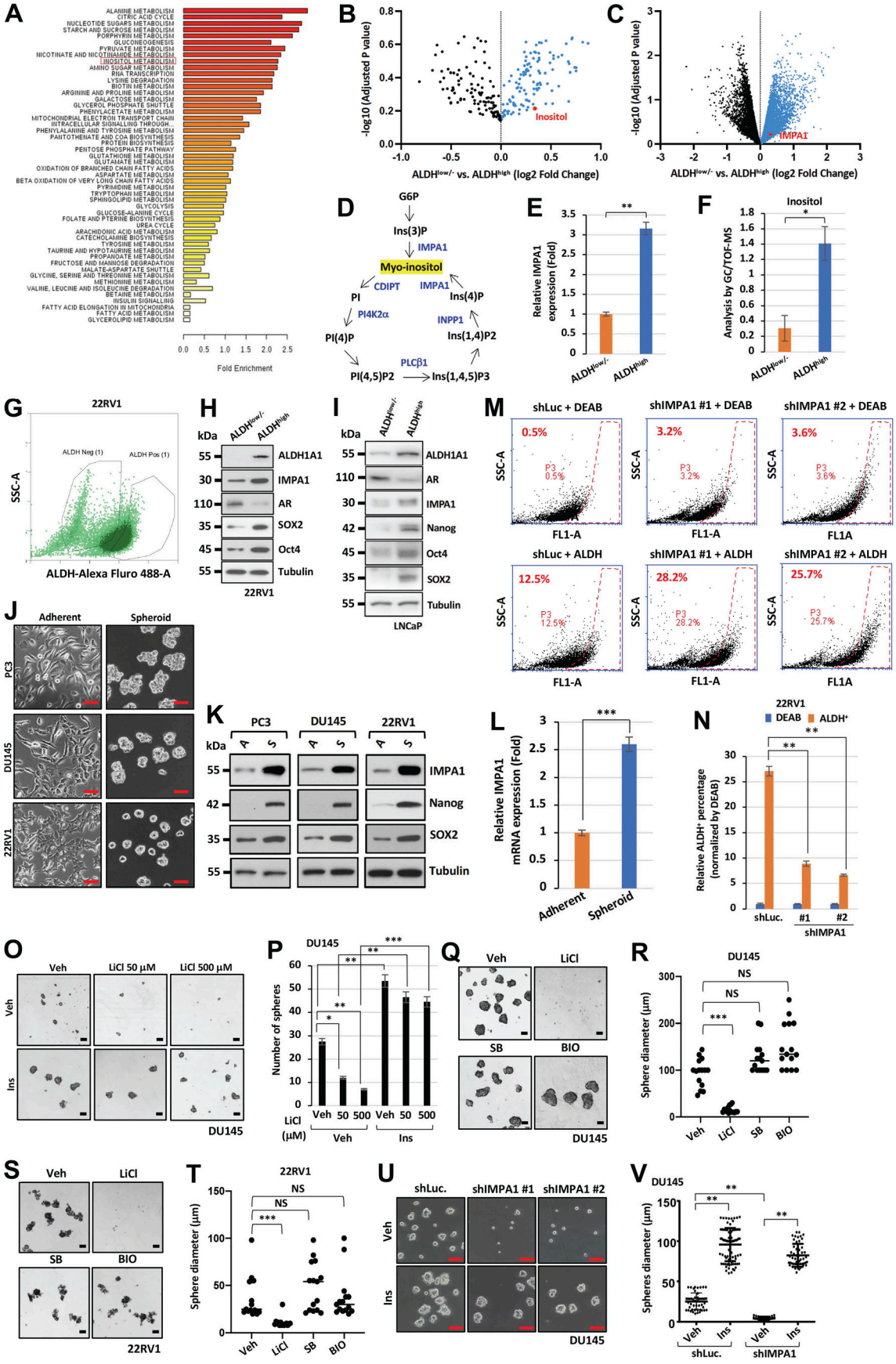
A
ALANINE METABOLISM
CITRIC ACID CYCLE
NUCLEOTIDE SUGARS METABOLISM
STARCH AND SUCROSE METABOLISM
PORPHYRIN METABOLISM
GLUCONEOGENESIS
PYRUVATE METABOLISM
NICOTINATE AND NICOTINAMIDE METABOLISM
INOSITOL METABOLISM
AMINO SUGAR METABOLISM
RNA TRANSCRIPTION
LYSINE DEGRADATION
BIOTIN METABOLISM
ARGININE AND PROLINE METABOLISM
GALACTOSE METABOLISM
GLYCEROL PHOSPHATE SHUTTLE
PHENYLACETATE METABOLISM
MITOCHONDRIAL ELECTRON TRANSPORT CHAIN
INTRACELLULAR SIGNALLING THROUGH...
PHENYLALANINE AND TYROSINE METABOLISM
PANTOTHENATE AND COA BIOSYNTHESIS
PROTEIN BIOSYNTHESIS
PENTOSE PHOSPHATE PATHWAY
GLUTATHIONE METABOLISM
GLUTAMATE METABOLISM
OXIDATION OF BRANCHED CHAIN FATTY ACIDS
ASPARTATE METABOLISM
BETA OXIDATION OF VERY LONG CHAIN FATTY ACIDS
PYRIMIDINE METABOLISM
TRYPTOPHAN METABOLISM
SPHINGOLIPID METABOLISM
GLYCOLYSIS
GLUCOSE-ALANINE CYCLE
FOLATE AND PTERINE BIOSYNTHESIS
UREA CYCLE
ARACHIDONIC ACID METABOLISM
CATECHOLAMINE BIOSYNTHESIS
TYROSINE METABOLISM
TAURINE AND HYPOTAURINE METABOLISM
PROPANOATE METABOLISM
FRUCTOSE AND MANNOSE DEGRADATION
MALATE-ASPARTATE SHUTTLE
GLYCINE, SERINE AND THREONINE METABOLISM
METHIONINE METABOLISM
VALINE, LEUCINE AND ISOLEUCINE DEGRADATION
BETAINE METABOLISM
INSULIN SIGNALLING
FATTY ACID ELONGATION IN MITOCHONDRIA
FATTY ACID METABOLISM
GLYCEROLIPID METABOLISM
0.0 0.5 1.0 1.5 2.0 2.5
Fold Enrichment
B
-log10 (Adjusted P value)
Inositol
ALDHlow/- vs. ALDHhigh (log2 Fold Change)
C
-log10 (Adjusted P value)
IMPA1
ALDHlow/- vs. ALDHhigh (log2 Fold Change)
D
G6P
Ins(3)P
IMPA1
Myo-inositol
CDIPT
IMPA1
PI
Ins(4)P
PI4K2α
INPP1
PI(4)P
Ins(1,4)P2
PLCβ1
PI(4,5)P2
Ins(1,4,5)P3
E
Relative IMPA1 expression (Fold)
ALDHlow/-
ALDHhigh
F
Inositol
Analysis by GC/TOF-MS
ALDHlow/-
ALDHhigh
G
22RV1
ALDH Neg (1)
ALDH Pos (1)
SSC-A
ALDH-Alexa Fluro 488-A
H
kDa
ALDHlow/-
ALDHhigh
55 ALDH1A1
30 IMPA1
110 AR
35 SOX2
45 Oct4
55 Tubulin
22RV1
I
kDa
ALDHlow/-
ALDHhigh
55 ALDH1A1
110 AR
30 IMPA1
42 Nanog
45 Oct4
35 SOX2
55 Tubulin
LNCaP
M
shLuc + DEAB
0.5%
shIMPA1 #1 + DEAB
3.2%
shIMPA1 #2 + DEAB
3.6%
shLuc + ALDH
12.5%
shIMPA1 #1 + ALDH
28.2%
shIMPA1 #2 + ALDH
25.7%
SSC-A
FL1-A
J
Adherent
Spheroid
PC3
DU145
22RV1
K
PC3
DU145
22RV1
kDa
A
S
55 IMPA1
42 Nanog
35 SOX2
55 Tubulin
L
Relative IMPA1 mRNA expression (Fold)
Adherent
Spheroid
N
22RV1
DEAB
ALDH+
Relative ALDH+ percentage (normalized by DEAB)
shLuc.
#1
#2
shIMPA1
O
Veh
LiCl 50 μM
LiCl 500 μM
Veh
Ins
DU145
P
DU145
Number of spheres
LiCl (μM)
Veh 50 500 Veh 50 500
Veh
Ins
Q
Veh
LiCl
SB
BIO
DU145
R
DU145
NS
Sphere diameter (μm)
Veh
LiCl
SB
BIO
S
Veh
LiCl
SB
BIO
22RV1
T
22RV1
NS
Sphere diameter (μm)
Veh
LiCl
SB
BIO
U
shLuc.
shIMPA1 #1
shIMPA1 #2
Veh
Ins
DU145
V
DU145
Spheres diameter (μm)
Veh
Ins
Veh
Ins
shLuc.
shIMPA1

Figure S1. **Inositol decline by IMPA1 loss impairs cancer sphere formation and ALDH^{high} PCSCs. (A)** Gene ontology enrichment analysis reveals the upregulated metabolism pathways in ALDH-positive (ALDH^{high}) PC3 cells compared with ALDH-negative (ALDH$^{low/-}$) PC3 cells. **(B and C)** Volcano plot shows upregulation of genes and metabolites in ALDH^{high} compared with ALDH$^{low/-}$ of LNCaP cells. LNCaP cells were isolated using FACS based on ALDH expression. **(D)** The graph represents the pathway of the PI cycle. **(E)** The graph represents the expression levels of IMPA1 from DNA microarray in ALDH^{high} and ALDH$^{low/-}$ PC3 cells. **(F)** The levels of inositol from metabolomics in ALDH^{high} and ALDH$^{low/-}$ of PC3 cells. **(G)** Dot plot of sorted ALDH^{high} and ALDH$^{low/-}$ 22RV1 cells population. **(H)** Immunoblotting of ALDH$^{low/-}$ and ALDH^{+} 22RV1 cells from cell sorting using ALDEFLUOR kit with indicated antibodies. Immunoblotting data were verified in at least two independent experiments. **(I)** Immunoblotting of ALDH^{high} and ALDH$^{low/-}$ LNCaP cells from cell sorting using ALDEFLUOR kit with indicated antibodies. Immunoblotting data were verified in at least two independent experiments. **(J)** The phase contrast shows the images of adherent and spheroid PC3, DU145, and 22RV1 cells. Scale bar, 100 µm. **(K)** Immunoblotting of adherent and spheroid PC3, DU145, and 22RV1 cells. Immunoblotting data were verified in at least two independent experiments. **(L)** The graph represents relative mRNA expression levels of IMPA1 in adherent and spheroid PC3 cells. **(M)** 22RV1 cells stably expressing shLuc, shIMPA1 (#1 and #2) incubated with ALDEFLUOR for 45 min. FACS profiles represent DEAB control and ALDH staining in each group. The gate (P3) was set according to DEAB control. **(N)** Quantification of relative ALDH positive cells normalized by DEAB control according to the gate (P3) from J is shown as the mean ± SEM of three independent experiments for each group. **, P < 0.01 by two-tailed unpaired *t* test. DEAB, ALDH inhibitor. **(O)** Spheres from DU145 upon vehicle (Veh), 25 µM of inositol (Ins), or 50 and 500 µM of LiCl treatment for 4 days. Scale bar, 100 µm. **(P)** Quantification of number of spheres from DU145 (O) was shown as the mean ± SEM of three independent experiments for each group. *, P < 0.05; **, P < 0.01; ***, P < 0.001 by two-tailed unpaired *t* test. **(Q and S)** Sphere forming cells from DU145 (N) and 22RV1 (P) upon vehicle (Veh), inositol (Ins), 500 µM of LiCl, 10 µM of SB216763 or BIO treatment. Scale bar, 100 µm. **(R and T)** Quantification of the size of spheres for R and T from DU145 (Q) and 22RV1 (S) upon the vehicle or 10 µM of inositol (Ins) treatment was shown as the mean ± SEM of three independent experiments for each group. ***, P < 0.001; NS, non-significant by two-tailed unpaired *t* test. **(U)** Spheres from DU145 stably expressing shLuc or IMPA1-two specific shRNA lentivirus (#1 and #2) upon vehicle (Veh) or 25 µM of inositol treatment (Ins). Scale bar, 100 µm. **(V)** Quantification of the size of spheres shown in R. At least five images of phase contrast were randomly captured, followed by using ImageJ software analysis. **, P < 0.01 by two-tailed unpaired *t* test. Source data are available for this figure: SourceData FS1.

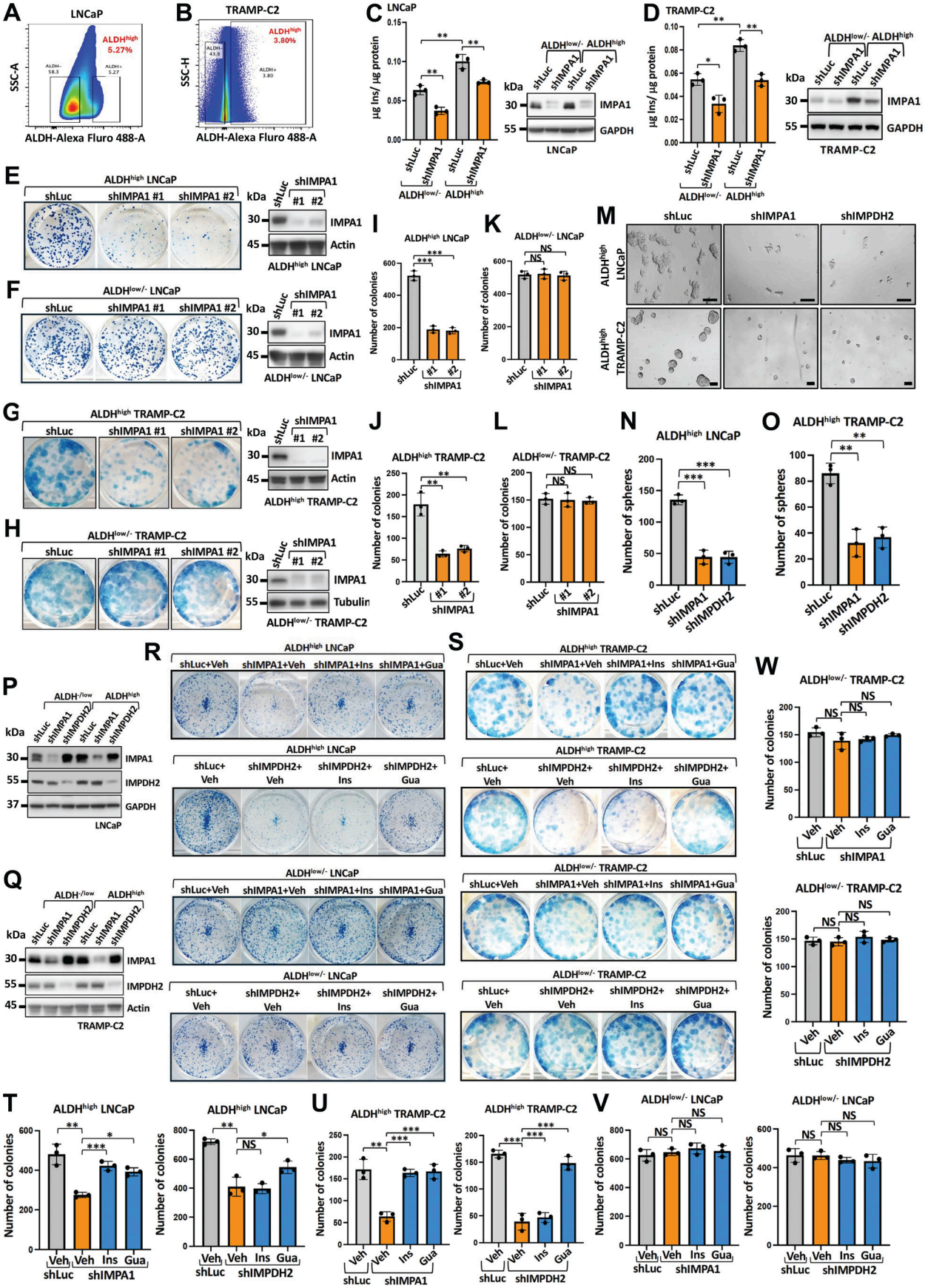
A
LNCaP
ALDHhigh 5.27%
SSC-A
ALDH-Alexa Fluro 488-A
B
TRAMP-C2
ALDHhigh 3.80%
SSC-H
ALDH-Alexa Fluro 488-A
C
LNCaP
µg Ins/ µg protein
shLuc
shIMPA1
ALDHlow/- ALDHhigh
kDa
IMPA1
GAPDH
LNCaP
D
TRAMP-C2
µg Ins/ µg protein
ALDHlow/- ALDHhigh
TRAMP-C2
E
ALDHhigh LNCaP
shLuc
shIMPA1 #1
shIMPA1 #2
IMPA1
Actin
F
ALDHlow/- LNCaP
G
ALDHhigh TRAMP-C2
H
ALDHlow/- TRAMP-C2
Tubulin
I
ALDHhigh LNCaP
Number of colonies
K
ALDHlow/- LNCaP
NS
M
shLuc
shIMPA1
shIMPDH2
ALDHhigh LNCaP
ALDHhigh TRAMP-C2
J
ALDHhigh TRAMP-C2
L
ALDHlow/- TRAMP-C2
N
ALDHhigh LNCaP
Number of spheres
O
ALDHhigh TRAMP-C2
P
ALDH-/low
ALDHhigh
IMPDH2
GAPDH
LNCaP
Q
Actin
TRAMP-C2
R
ALDHhigh LNCaP
shLuc+Veh
shIMPA1+Veh
shIMPA1+Ins
shIMPA1+Gua
shIMPDH2+ Veh
shIMPDH2+ Ins
shIMPDH2+ Gua
S
ALDHhigh TRAMP-C2
ALDHlow/- LNCaP
ALDHlow/- TRAMP-C2
W
ALDHlow/- TRAMP-C2
Veh
Ins
Gua
T
ALDHhigh LNCaP
U
ALDHhigh TRAMP-C2
V
ALDHlow/- LNCaP

Figure S2. **IMPA1/inositol/IMPDH2 pathway maintains the proliferation of ALDH^{high} cells, but not ALDH$^{low/-}$ cells. (A and B)** Dot plot of sorted ALDH^{high} and ALDH$^{low/-}$ LNCaP (A) and TRAMP-C2 (B) cells population. **(C and D)** Inositol levels were determined by K-INOSL assay kit according to the manufacturer's instructions. The inositol levels were normalized by protein concentration in each experimental group. Three independent experiments were performed. *, P < 0.05; **, P < 0.01 by two-tailed unpaired *t* test. Immunoblotting of ALDH^{high} and ALDH$^{low/-}$ LNCaP cells and ALDH^{high} and ALDH$^{low/-}$ TRAMP-C2 cells with indicated antibodies. **(E–H)** Colony formation of ALDH^{high} (E and G) and ALDH$^{low/-}$ (F and H) LNCaP cells and TRAMPC-C2 cells upon shLuc and shIMPA1 (#1 and #2). Immunoblotting of ALDH^{high} (E and G) and ALDH$^{low/-}$ (F and H) LNCaP cells and TRAMP-C2 cells stably expressing shLuc and shIMPA1 (#1 and #2). **(I–L)** Quantification of number of colonies of ALDH^{high} (I and J) and ALDH$^{low/-}$ (K and L) LNCaP cells (I and K) and TRAMPC-C2 cells (J and L). The data are shown as the mean ± SEM of three independent experiments for each group. **, P < 0.01; ***, P < 0.001; NS, non-significant by two-tailed unpaired *t* test. **(M)** Cancer sphere formation in ALDH^{high} LNCaP and ALDH^{high} TRAMP-C2 cells upon shLuc, shIMPA1 #1 and shIMPDH2 #1. Scale bar, 100 µm. **(N and O)** Quantification of cancer sphere formation of ALDH^{high} LNCaP cells (N) and ALDH^{high} TRAMP-C2 cells (O) from M. The data are shown as the mean ± SEM of three independent experiments for each group. **, P < 0.01; ***, P < 0.001 by two-tailed unpaired *t* test. **(P and Q)** Immunoblotting of ALDH^{high} and ALDH$^{low/-}$ LNCaP (P) and TRAMP-C2 (Q) cells stably expressing shLuc, shIMPA1 #1, or shIMPDH2 #1 with indicated antibodies. Immunoblotting data were verified in at least two independent experiments. **(R and S)** Colony formation of ALDH^{high} or ALDH$^{low/-}$ LNCaP (R) and TRAMP-C2 (S) cells stably expressing shLuc, shIMPA1 #1, or shIMPDH2 #1 upon vehicle, 80 µM of inositol (Ins), and 80 µM of guanosine (Gua) treatment. **(T–W)** Quantification of number of colonies of ALDH^{high} (T and U) or ALDH$^{low/-}$ (V and W) LNCaP (T and V) and TRAMP-C2 (U and W) cells upon shLuc, shIMPA1 #1, shIMPDH2 #1 with vehicle, 80 µM of inositol (Ins), and 80 µM of guanosine (Gua) treatment from R and S. The data were shown as the mean ± SEM of three independent experiments for each group. *, P < 0.05; **, P < 0.01; ***, P < 0.001 by two-tailed unpaired *t* test. Source data are available for this figure: SourceData FS2.

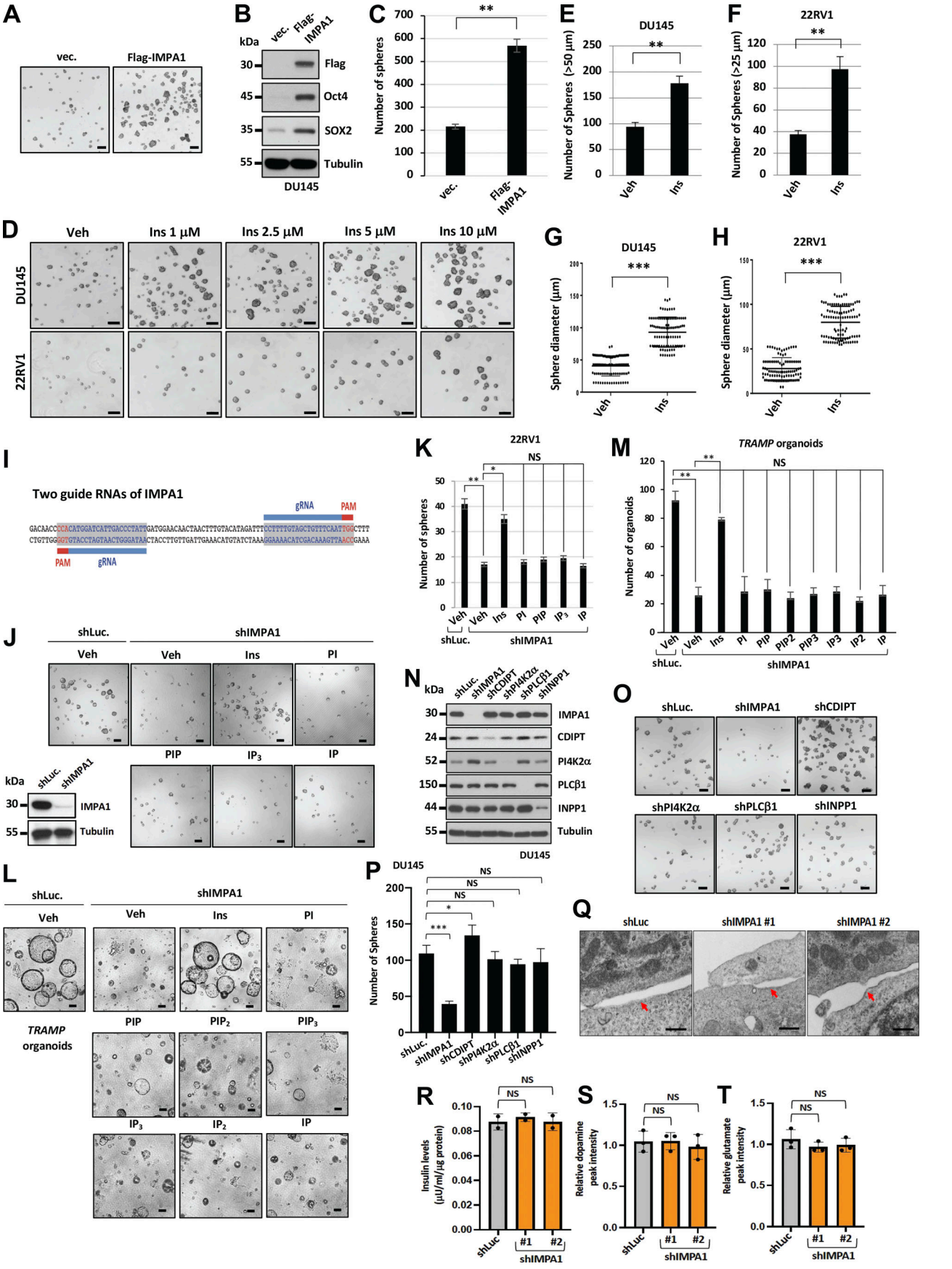
A
vec.
Flag-IMPA1
B
kDa
vec.
Flag-IMPA1
30
Flag
45
Oct4
35
SOX2
55
Tubulin
DU145
C
Number of spheres
**
vec.
Flag-IMPA1
E
DU145
Number of Spheres (>50 µm)
**
Veh
Ins
F
22RV1
Number of Spheres (>25 µm)
**
Veh
Ins
D
Veh
Ins 1 µM
Ins 2.5 µM
Ins 5 µM
Ins 10 µM
DU145
22RV1
G
DU145
Sphere diameter (µm)
***
Veh
Ins
H
22RV1
Sphere diameter (µm)
***
Veh
Ins
I
Two guide RNAs of IMPA1
gRNA
PAM
GACAACCCCACATGGATCATTGACCCTATTGATGGAACAACTAACTTTGTACATAGATTTCCTTTTGTAGCTGTTTCAATTGGCTTT
CTGTTGGGGTGTACCTAGTAACTGGGATAACTACCTTGTTGATTGAAACATGTATCTAAAGGAAAACATCGACAAAGTTAACCGAAA
PAM
gRNA
J
shLuc.
shIMPA1
Veh
Veh
Ins
PI
PIP
IP3
IP
kDa
shLuc.
shIMPA1
30
IMPA1
55
Tubulin
K
22RV1
NS
Number of spheres
**
*
Veh
Veh
Ins
PI
PIP
IP3
IP
shLuc.
shIMPA1
M
TRAMP organoids
NS
**
**
Number of organoids
Veh
Veh
Ins
PI
PIP
PIP2
PIP3
IP3
IP2
IP
shLuc.
shIMPA1
N
kDa
shLuc.
shIMPA1
shCDIPT
shPI4K2α
shPLCβ1
shINPP1
30
IMPA1
24
CDIPT
52
PI4K2α
150
PLCβ1
44
INPP1
55
Tubulin
DU145
O
shLuc.
shIMPA1
shCDIPT
shPI4K2α
shPLCβ1
shINPP1
L
shLuc.
shIMPA1
Veh
Veh
Ins
PI
TRAMP organoids
PIP
PIP2
PIP3
IP3
IP2
IP
P
DU145
NS
NS
NS
*
***
Number of Spheres
shLuc.
shIMPA1
shCDIPT
shPI4K2α
shPLCβ1
shINPP1
Q
shLuc
shIMPA1 #1
shIMPA1 #2
R
NS
NS
Insulin levels (µU/ml/µg protein)
shLuc
#1
#2
shIMPA1
S
NS
NS
Relative dopamine peak intensity
shLuc
#1
#2
shIMPA1
T
NS
NS
Relative glutamate peak intensity
shLuc
#1
#2
shIMPA1

Figure S3. **Inositol directly maintains cancer stemness in prostate cancer spheres and tumor organoids independently of its downstream PI cycle.** **(A)** Spheres from DU145 stably expressing Flag vector or Flag-IMPA1 lentivirus. Scale bar, 100 µm. **(B)** The cell lysates of spheres from DU145 stably expressing Flag vector or Flag-IMPA1 lentivirus were subjected to immunoblotting with indicated antibodies. **(C)** Quantification of number of spheres from DU145 (A) was shown as the mean ± SEM of three independent experiments for each group. **, P < 0.001 by two-tailed unpaired *t* test. **(D)** Representative images of spheres from DU145 and 22RV1 upon 1, 2.5, 5, and 10 µM of inositol treatment for 4 days. Scale bar, 150 µm. **(E–H)** Quantification of the size and number of spheres from DU145 (E and G) and 22RV1 (F and H) upon the vehicle or 10 µM of inositol (Ins) treatment is shown as the mean ± SEM of three independent experiments for each group. **, P < 0.01 by two-tailed unpaired *t* test. **(I)** Illustration of cDNA sequence of IMPA1 targeted by the gRNA pairs. **(J)** Photographs of spheres from 22RV1 cells stably expressing shLuc or shIMPA1 upon the treatment of vehicle (Veh), 25 µM of inositol (Ins), 4 µM of PI, phosphatidylinositol 4-phosphate (PIP), phosphatidylinositol 4,5-bisphosphate (PIP_2), phosphatidylinositol 3,4,5-trisphosphate (PIP_3), 25 µM of inositol 1,3,4-trisphosphate (IP_3), inositol 1,4-bisphosphate (IP_2), or inositol 4-phosphate (IP). Immunoblotting of 22RV1 cells stably expressing shLuc or shIMPA1 with indicated antibodies. Scale bar, 100 µm. **(K)** Quantification of the number of spheres from 22RV1 (J) was shown as the mean ± SEM of three independent experiments for each group. *, P < 0.05; **, P < 0.01; NS, non-significant by two-tailed unpaired *t* test. **(L)** Tumor organoids from TRAMP expressing shLuc or shIMPA1 upon the treatment of vehicle (Veh) or 25 µM of inositol (Ins), 4 µM of PI, phosphatidylinositol 4-phosphate (PIP), phosphatidylinositol 4,5-bisphosphate (PIP_2), phosphatidylinositol 3,4,5-trisphosphate (PIP_3), 25 µM of inositol 1,3,4-trisphosphate (IP_3), inositol 1,4-bisphosphate (IP_2) or inositol 4-phosphate (IP) were shown. Scale bar, 100 µm. **(M)** Quantification of the number of tumor organoids from TRAMP was shown as the mean ± SEM of three independent experiments for each group. **, P < 0.01; NS, non-significant by two-tailed unpaired *t* test. **(N)** Immunoblotting of DU145 cells stably expressing shLuc, shIMPA1, shCDIPT, shPI4K2α, shPLCβ1, or shINPP1 with indicated antibodies. **(O)** Photographs of spheres from DU145 cells stably expressing shLuc, shIMPA1, shCDIPT, shPI4K2α, shPLCβ1, or shINPP1. Scale bar, 100 µm. **(P)** Quantification of the number of spheres from DU145 (O) was shown as the mean ± SEM of three independent experiments for each group. *, P < 0.05; ***, P < 0.001; NS, non-significant by two-tailed unpaired *t* test. **(Q)** The images of the EM represent the cell membrane from DU145 cells stably expressing shLuc and shIMPA1 (#1 and #2). The red arrow indicates cell membrane. **(R)** Insulin levels were determined by human insulin ELISA kit (Elabscience) in $ALDH^{high}$ LNCaP cells upon shLuc and shIMPA1 (#1 and #2). NS, non-significant. **(S and T)** The levels of dopamine (S) and glutamine (T) were determined by LC-MC/MS in 22RV1 cells upon shLuc and shIMPA1 (#1 and #2). NS, non-significant. Triplicate samples in each group were performed for LC-MS/MS. Source data are available for this figure: SourceData FS3.

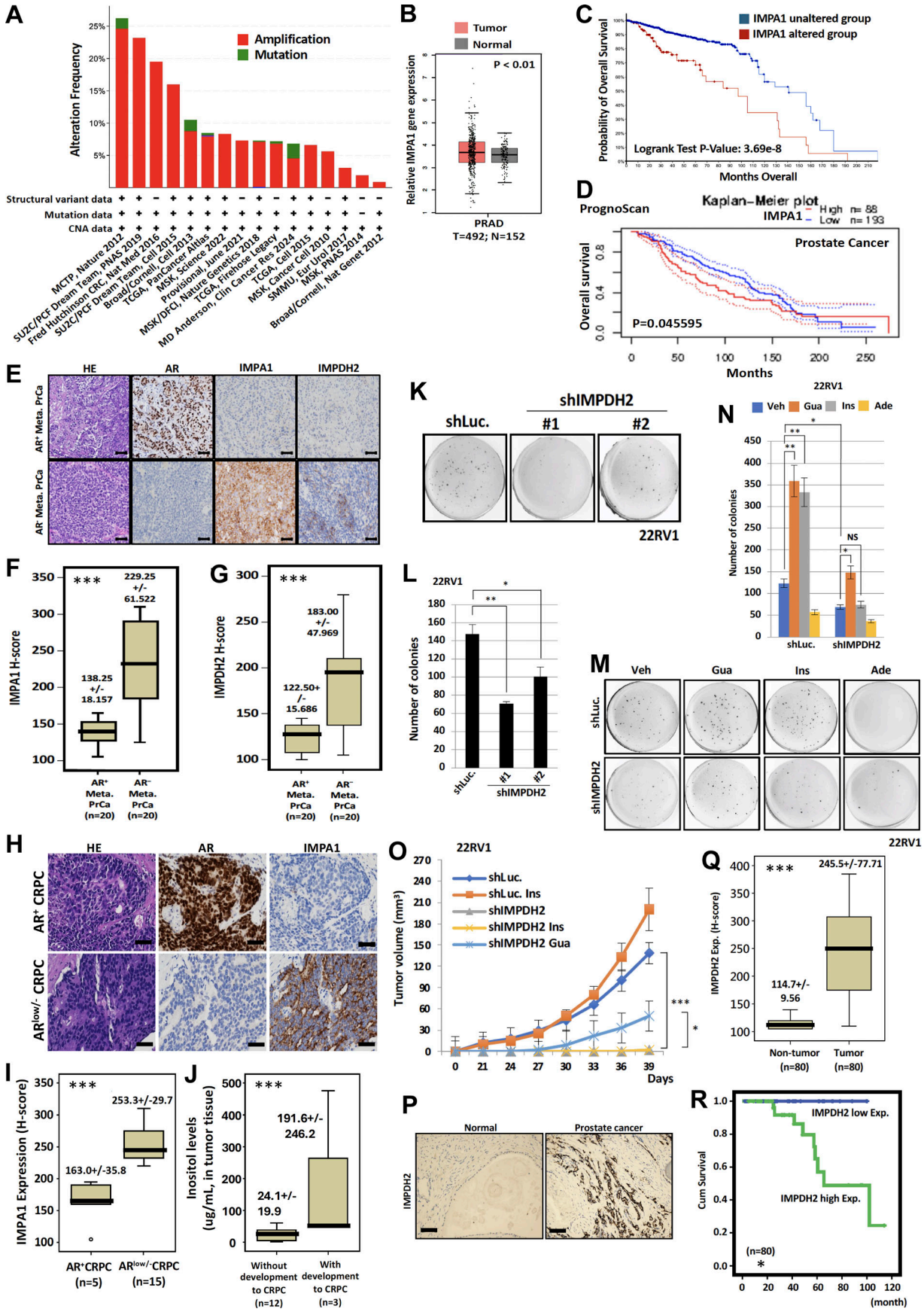
A
Amplification
Mutation
Alteration Frequency
Structural variant data
Mutation data
CNA data
MCTP, Nature 2012
SU2C/PCF Dream Team, PNAS 2019
Fred Hutchinson CRC, Nat Med 2016
SU2C/PCF Dream Team, Cell 2015
Broad/Cornell, Cell 2013
TCGA, PanCancer Atlas
MSK, Science 2022
Provisional, June 2021
MSK/DFCI, Nature Genetics 2018
MD Anderson, Clin Cancer Legacy
TCGA, Firehose Legacy
TCGA, Cell 2015
MSK, Cancer Cell 2010
SMMU, Eur Urol 2017
MSK, PNAS 2014
Broad/Cornell, Nat Genet 2012
B
Tumor
Normal
P < 0.01
Relative IMPA1 gene expression
PRAD
T=492; N=152
C
IMPA1 unaltered group
IMPA1 altered group
Probability of Overall Survival
Logrank Test P-Value: 3.69e-8
Months Overall
D
PrognoScan
Kaplan–Meier plot
IMPA1
High n= 88
Low n= 193
Prostate Cancer
Overall survival
P=0.045595
Months
E
HE
AR
IMPA1
IMPDH2
AR+ Meta. PrCa
AR- Meta. PrCa
F
IMPA1 H-score
***
229.25 +/- 61.522
138.25 +/- 18.157
AR+ Meta. PrCa (n=20)
AR- Meta. PrCa (n=20)
G
IMPDH2 H-score
***
183.00 +/- 47.969
122.50+ /- 15.686
AR+ Meta. PrCa (n=20)
AR- Meta. PrCa (n=20)
H
HE
AR
IMPA1
AR+ CRPC
AR low/- CRPC
I
IMPA1 Expression (H-score)
***
253.3+/-29.7
163.0+/-35.8
AR+CRPC (n=5)
AR low/- CRPC (n=15)
J
Inositol levels (ug/mL, in tumor tissue)
***
191.6+/- 246.2
24.1+/- 19.9
Without development to CRPC (n=12)
With development to CRPC (n=3)
K
shIMPDH2
shLuc.
#1
#2
22RV1
L
22RV1
Number of colonies
shLuc.
#1
#2
shIMPDH2
M
Veh
Gua
Ins
Ade
shLuc.
shIMPDH2
N
22RV1
Veh
Gua
Ins
Ade
Number of colonies
NS
shLuc.
shIMPDH2
O
22RV1
shLuc.
shLuc. Ins
shIMPDH2
shIMPDH2 Ins
shIMPDH2 Gua
Tumor volume (mm³)
***
*
Days
P
Normal
Prostate cancer
IMPDH2
Q
22RV1
IMPDH2 Exp. (H-score)
***
245.5+/-77.71
114.7+/- 9.56
Non-tumor (n=80)
Tumor (n=80)
R
IMPDH2 low Exp.
IMPDH2 high Exp.
Cum Survival
(n=80)
*
(month)

Figure S4. **IMPA1 and IMPDH2 are upregulated in prostate cancer patients correlated with poor survival outcome. (A)** The frequency of alteration of *IMPA1* gene in human prostate cancers. The representative data obtained from cBioPortal (https://www.cbioportal.org) representing a combined study of 4,104 samples, querying 3,886 prostate cancer patients in 16 studies are shown by a bar graph. **(B)** The bar graph represents the relative expression of IMPA1 in normal tissues (152) and prostate cancers (492) from the GEPIA database. P < 0.01. **(C)** The overall survival of prostate cancer patients with IMPA1 altered group (121 cases) and IMPA1 unaltered group (1,157 cases). The representative data also obtained from cBioPortal (https://www.cbioportal.org) representing a combined study of 4,104 samples, querying 3,886 prostate patients in 16 studies as shown by overall survival Kaplan–Meier plot. The median months overall survival of the IMPA1 altered group and IMPA1 unaltered group are 97 and 141 mo, respectively. Long–rank test P value = 3.69e–8. **(D)** The overall survival Kaplan–Meier plot of prostate cancer patients with IMPA1 high and low expression from the database of PrognoScan. Long–rank test P value = 0.045595. **(E)** Prostate tissue from AR^+ metastatic prostate cancer and $AR^{low/-}$ metastatic prostate cancer patients in our in-house prostate cancer samples were determined by IHC staining with indicated antibodies. Scale bar, 100 µm. **(F and G)** Box plot represents IMPA1 (F) and IMPDH2 (G) expression in AR^+ metastatic prostate cancer (20 cases) and AR^- metastatic prostate cancer (20 cases). ***, P < 0.001 by Mann–Whitney U test. **(H)** Prostate tissue from AR^+ CRPC and $AR^{low/-}$ CRPC in our in-house prostate cancer samples were determined by IHC staining with indicated antibodies. Scale bar, 200 µm. **(I)** Box plot represents IMPA1 expression levels by H-score in AR^+ CRPC (*n* = 5) and $AR^{low/-}$ CRPC (*n* = 15) prostate cancer patients. ***, P < 0.001 (AR^+ CRPC versus $AR^{low/-}$ CRPC) by Mann–Whitney U test. **(J)** Inositol levels were determined by LC-MS/MS in the prostate tissues of the patients without or with the development to CRPC. ***, P < 0.001 (patients without CRPC versus patient with CRPC) by Mann–Whitney U test. **(K)** Soft agar assay shown in 22RV1 cells stably expressing shLuc or shIMPDH2 (#1 and #2). **(L)** Quantification of the number of colonies from 22RV1 by ImageJ shown in K. The data were shown as the mean ± SEM of three independent experiments for each group. *, P < 0.05; **, P < 0.01 by two-tailed unpaired *t* test. **(M)** Soft agar assay shown in 22RV1 cells stably expressing shLuc or shIMPDH2 upon the treatment of 40 µM of guanosine (Gua), 40 µM of inositol (Ins) or 40 µM of adenosine (Ade) for 20 days. **(N)** Quantification of the number of colonies from 22RV1 by ImageJ shown in M. The data were shown as the mean ± SEM of three independent experiments for each group. *, P < 0.05; **, P < 0.01 by two-tailed unpaired *t* test. **(O)** Male nude mice subcutaneously injected with 22RV1 cells stably expressing shLuc or shIMPDH2 were intraperitoneally injected with 30 mg/kg of inositol (Ins) or 30 mg/kg of guanosine (Gua) every 2 days until 39 days, and tumor volume was measured with indicated days. Four mice were included in each experimental group. **(P)** IMPDH2 protein expression from adjacent normal and prostate cancer patients with high Gleason scores, and advanced stage in our in-house prostate cancer samples was determined by IHC staining. Scale bar, 20 µm. **(Q)** Box plot represents IMPDH2 expression in adjacent normal (80 cases) and prostate cancer patients with high Gleason score and advanced stage (80 cases). ***, P < 0.001 by Mann–Whitney U test. **(R)** Disease-specific survival outcome with IMPDH2 low or high expression was shown by Kaplan–Meier plots in prostate cancer patients with high Gleason score and advanced stage (80 cases). *, P = 0.0171 by long–rank test.

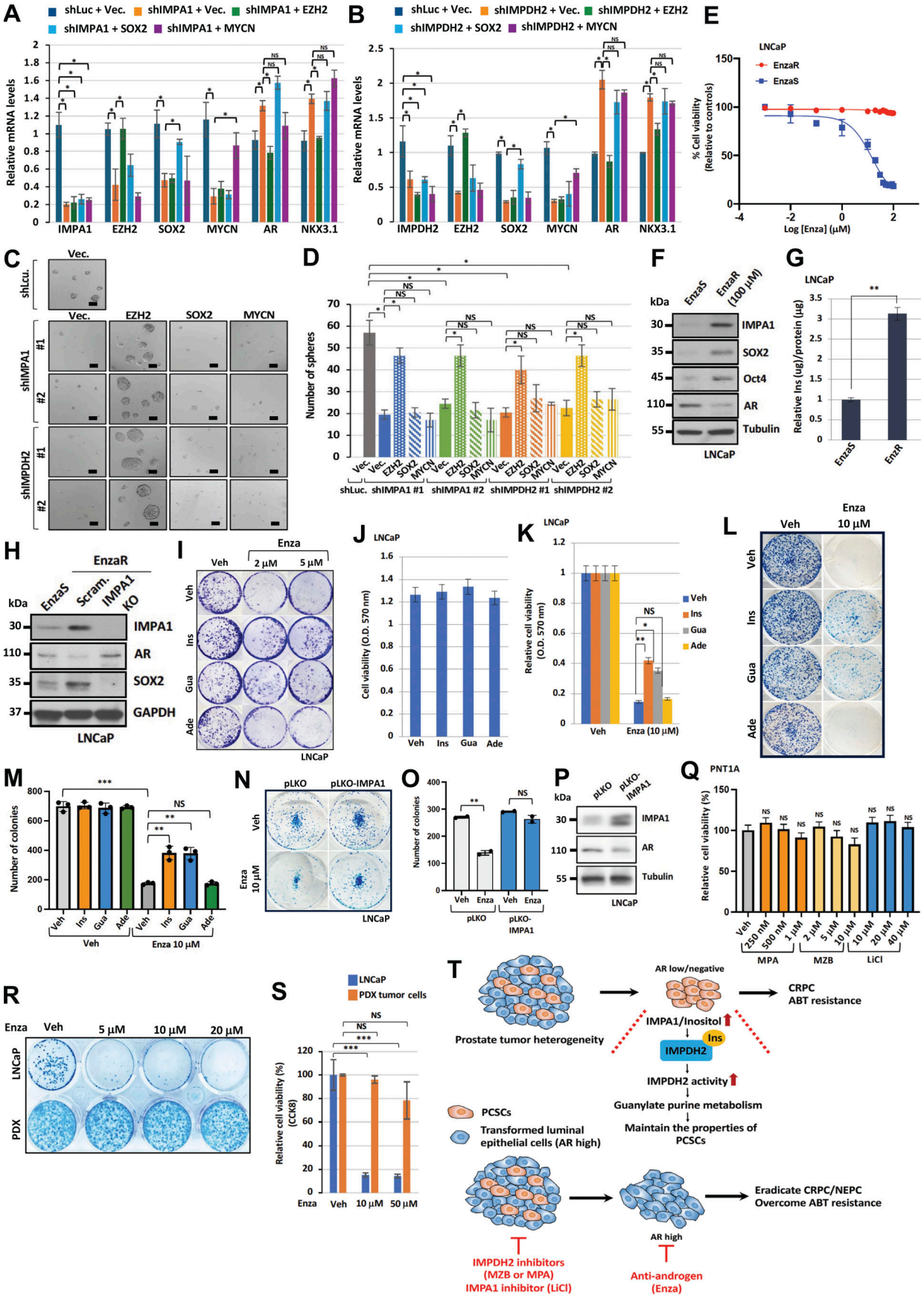
A
shLuc + Vec.
shIMPA1 + Vec.
shIMPA1 + EZH2
shIMPA1 + SOX2
shIMPA1 + MYCN
Relative mRNA levels
IMPA1
EZH2
SOX2
MYCN
AR
NKX3.1
B
shLuc + Vec.
shIMPDH2 + Vec.
shIMPDH2 + EZH2
shIMPDH2 + SOX2
shIMPDH2 + MYCN
Relative mRNA levels
IMPDH2
EZH2
SOX2
MYCN
AR
NKX3.1
E
LNCaP
EnzaR
EnzaS
% Cell viability (Relative to controls)
Log [Enza] (μM)
C
Vec.
shLcu.
shIMPA1 #1
shIMPA1 #2
shIMPDH2 #1
shIMPDH2 #2
EZH2
SOX2
MYCN
D
Number of spheres
shLuc.
shIMPA1 #1
shIMPA1 #2
shIMPDH2 #1
shIMPDH2 #2
F
kDa
EnzaS
EnzaR (100 μM)
IMPA1
SOX2
Oct4
AR
Tubulin
LNCaP
G
LNCaP
Relative Ins (ug)/protein (μg)
EnzaS
EnzaR
H
EnzaR
kDa
EnzaS
Scram.
IMPA1 KO
IMPA1
AR
SOX2
GAPDH
LNCaP
I
Enza
Veh
2 μM
5 μM
Ins
Gua
Ade
LNCaP
J
LNCaP
Cell viability (O.D. 570 nm)
Veh
Ins
Gua
Ade
K
LNCaP
Relative cell viability (O.D. 570 nm)
Veh
Ins
Gua
Ade
Enza (10 μM)
L
Enza
Veh
10 μM
Ins
Gua
Ade
M
Number of colonies
Veh
Ins
Gua
Ade
Enza 10 μM
N
pLKO
pLKO-IMPA1
Veh
Enza 10 μM
LNCaP
O
Number of colonies
Veh
Enza
pLKO
pLKO-IMPA1
P
kDa
pLKO
pLKO-IMPA1
IMPA1
AR
Tubulin
LNCaP
Q
PNT1A
Relative cell viability (%)
Veh
250 nM
500 nM
1 μM
2 μM
5 μM
10 μM
10 μM
20 μM
40 μM
MPA
MZB
LiCl
R
Enza
Veh
5 μM
10 μM
20 μM
LNCaP
PDX
S
LNCaP
PDX tumor cells
Relative cell viability (%) (CCK8)
Enza
Veh
10 μM
50 μM
T
Prostate tumor heterogeneity
AR low/negative
CRPC
ABT resistance
IMPA1/Inositol
Ins
IMPDH2
IMPDH2 activity
Guanylate purine metabolism
Maintain the properties of PCSCs
PCSCs
Transformed luminal epithelial cells (AR high)
AR high
Eradicate CRPC/NEPC
Overcome ABT resistance
IMPDH2 inhibitors (MZB or MPA)
IMPA1 inhibitor (LiCl)
Anti-androgen (Enza)

Figure S5. **IMPA1/inositol/IMPDH2 axis maintains EZH2 expression and PCSCs with AR$^{low/-}$ features and endows enzalutamide resistance.** **(A)** Relative gene expression of IMPA1, EZH2, SOX2, and MYCN in 22RV1 cells stably expressing shLuc or shIMPA1 upon overexpression of Vec. (vector), EZH2, SOX2, and MYCN, followed by qRT-PCR. Data were shown as the mean ± SEM of three independent experiments for each group. *, P < 0.05; NS, non-significant by two-tailed unpaired *t* test. **(B)** Relative gene expression of IMPDH2, EZH2, SOX2, and MYCN in 22RV1 cells stably expressing shLuc or shIMPDH2 upon overexpression of Vec. (vector), EZH2, SOX2, and MYCN followed by qRT-PCR. The data are shown as the mean ± SEM of three independent experiments for each group. *, P < 0.05; NS, non-significant by two-tailed unpaired *t* test. **(C)** Spheres from 22RV1 stably expressing shLuc or shIMPA1 (#1 and #2) upon overexpression of Vec. (vector), EZH2, SOX2, and MYCN are shown. Scale bar, 100 µm. **(D)** Quantification of the number of spheres from C is shown as the mean ± SEM of three independent experiments for each group for 22RV1. *, P < 0.05; NS, non-significant by two-tailed unpaired *t* test. **(E)** Cell viability was determined by CCK-8 assay upon indicated doses of enzalutamide treatment for 48 h in LNCaP EnzaS and EnzaR cells. **(F)** Immunoblotting of LNCaP EnzaS and EnzaR cell lines with indicated antibodies. **(G)** The levels of inositol in LNCaP EnzaS and EnzaR cell lines was determined by K-INOSL assay kit. The inositol levels were normalized by protein concentration in each experimental group. Three independent experiments were performed for the statistic of a two-tailed unpaired *t* test. **, P < 0.01. **(H)** Immunoblotting of LNCaP EnzaS and EnzaR cell lines expressing scramble (Scram.) and CRISPR/Cas9 IMPA1 knockout (IMPA1 KO) with indicated antibodies. Immunoblotting data were verified in at least two independent experiments. **(I)** Colony formation assay of LNCaP cells upon vehicle (Veh), 2 or 5 µM of enzalutamide (Enza), 40 µM of inositol (Ins), 40 µM of guanosine (Gua), or 40 µM of adenosine (Ade) treatment every 2 days for 14 days. **(J)** MTT assay of LNCaP cells upon vehicle (Veh), 40 µM of inositol (Ins), 40 µM of guanosine (Gua), or 40 µM of adenosine (Ade) treatment for 72 h. The data are shown as the mean ± SEM of three independent experiments for each group. NS, non-significant by two-tailed unpaired *t* test. **(K)** MTT assay of LNCaP cells upon vehicle (Veh), 10 µM of enzalutamide (Enza), 40 µM of inositol (Ins), 40 µM of guanosine (Gua), or 40 µM of adenosine (Ade) treatment for 72 h. The data were shown as the mean ± SEM of three independent experiments for each group. *, P < 0.05; **, P < 0.01; NS, non-significant by two-tailed unpaired *t* test. **(L)** Colony formation of LNCaP cells upon vehicle (Veh), 10 µM of enzalutamide (Enza), 40 µM of inositol (Ins), 40 µM of guanosine (Gua), or 40 µM of adenosine (Ade) treatment every 2 days for 14 days. **(M)** Quantification of the number of colonies from L–M by using ImageJ software. The data are shown as the mean ± SEM of three independent experiments for each group. **, P < 0.01; ***, P < 0.001; NS, non-significant by two-tailed unpaired *t* test. **(N)** Colony formation assay of LNCaP cells by seeding 4,000 cells upon pLKO vector or pLKO-IMPA1 stably expression in response to vehicle (Veh) and 10 µM of enzalutamide (Enza) treatment every 2 days for 14 days. **(O)** Quantification of number of colonies from N was shown. The data were shown as the mean ± SEM of three independent experiments for each group. **, P < 0.01; NS, non-significant by two-tailed unpaired *t* test. **(P)** Immunoblotting of LNCaP stably expressing pLKO or pLKO-IMPA1 with indicated antibodies. Immunoblotting data were verified in at least two independent experiments. **(Q)** PNT1A cells were treated with the concentration of MPA, MZB, and LiCl as indicated for 72 h, followed by CCK-8 assay. The data are shown as the mean ± SEM of three independent experiments for each group. NS, non-significant by two-tailed unpaired *t* test. **(R)** Colony formation assay of PDX tumor cells isolated from PDX tumors or LNCaP cells by seeding 2,000 cells upon vehicle (Veh), 5, 10, and 20 µM of enzalutamide (Enza) treatment for 14 days. **(S)** Relative cell viability of EnzaS LNCaP cells and PDX cells upon vehicle (Veh), 10 or 50 µM of enzalutamide (Enza) treatment for 48 h were determined by CCK-8. The data were shown as the mean ± SEM of three independent experiments for each group. ***, P < 0.001; NS, non-significant by two-tailed unpaired *t* test. **(T)** Working model for the role of IMPA1/inositol/IMPDH2 axis with PCSC properties to promote CRPC progression and ABT resistance. In the prostate hierarchical model, IMPA1/inositol/IMPDH2 axis maintains PCSC properties with AR$^{low/-}$ features leading to CRPC progression and ABT resistance. Mechanistically, inositol directly binds to and activates IMPDH2 activity to promote guanylate purine metabolism. Notably, IMPA1/inositol/IMPDH2/guanosine axis serves as an upstream signal critical for maintaining PCSCs with AR$^{low/-}$ features leading to CRPC and ABT resistance. Hence, pharmacological inhibition of IMPA1 or IMPDH2 eradicates PCSCs with AR$^{low/-}$ features while it enhances AR^{+} luminal cell identity, leading to resensitizing ABT treatment. Thus, the combination of the IMPA1 inhibitor (LiCl) or IMPDH2 inhibitors (MZB or MPA) with ABT, enzalutamide (Enza), is a promising therapeutic strategy for targeting CRPC and overcoming ABT resistance. We therefore identify the critical role of the IMPA1/inositol/IMPDH2/guanosine axis as a master metabolic pathway for driving CRPC and ABT resistance. Source data are available for this figure: SourceData FS5.

Provided online are Table S1 and Data S1. Table S1 shows identification of inositol-binding proteins using biotin-labeled inositol pull-down assay, followed by mass spectrometry analysis. Data S1 shows analysis of the copy number of *IMPA1* gene in prostate cancer.